High-Pressure Synthesis of Thermoelectric Materials

Thesis by
Geoff Staneff

In Partial Fulfillment of the Requirements
for the Degree of
Doctor of Philosophy

California Institute of Technology
Pasadena, California
2005
(Defended November 24, 2004)

Acknowledgements

I would like to acknowledge a number of people who were instrumental in the completion of this dissertation. I am especially grateful to my advisor, Dr. Paul Asimow, for his guidance and for taking on this project three years ago. I thank Thierry Caillat for providing insight into the workings of thermoelectric systems, and for arranging the funding much of this research. Without the expertise of Jed Mosenfelder, especially on the topic of high-pressure synthesis, I would have been lost in the wilderness. I am also grateful to all the members of the Thermoelectrics Group at JPL, and Chi Ma for his assistance in the GPS Analytical Facility.

I would like to thank my friends and family for providing support while I've completed this work. I thank the lads at the San Fernando Valley Rugby Club for introducing a regular dose of blue-collar reality into my ivory tower life. And I must thank the players and associates of the Caltech Rugbyclub. Without these people I would not be here today.

I also thank Pawan Gogna for providing a new direction for our. The last six months have been a rewarding experience that has opened new possibilities for thermoelectrics research. Much enthusiasm has been rekindled due to our recent work in nano-structured silicon-germanium materials.

And finally I thank Lori for whom it must have seemed like I would never finish writing this. Without her friendship, support and understanding I might not have.

Abstract

New thermoelectric materials were synthesized using high-pressure techniques. The synthetic limits of cerium filling in cobalt triantimonide were explored and a model for successful synthesis conditions was generated. The high-pressure technique expanded the practical filling limit from x=0.07 to x=0.5 in the $Ce_xCo_4Sb_{12}$ system. Explorations of cerium filled ruthenium-rhodium triantimonide were also undertaken, using our previous work to guide the synthesis attempt. This material was predicted to have outstanding thermoelectric properties, but our investigations did not confirm this result. The filled skutterudite, $Ce(Ru_{0.67}Rh_{0.33})_4Sb_{12}$, exhibited the low thermal conductivity anticipated, approximately half the total thermal conductivity of a binary $CoSb_3$ skutterudite over a wide range in temperatures. The electrical properties were insufficient to produce a high efficiency thermoelectric, but these results did suggest incorporated rare earth filling atoms do not fully ionize when incorporated into the skutterudite structure. Modification of the carrier type should therefore be investigated by solid solution on the transition metal or pnictide sites and not the filling ion.

The high-pressure synthesis techniques developed for skutterudite synthesis were then employed to sinter nano-scale silicon-germanium compounds. A sintering figure of merit was created to justify the use of high-pressure synthesis, which later proved to be a useful tool for planning subsequent experiments. Sintered silicon, germanium, and silicon-germanium composites were obtained, with the nano-scale grain structure and chemical heterogeneity of the starting powder aggregate intact.

Future work in high-pressure synthesis should be undertaken to quantify the sintering figure of merit presented in this work. The ability to produce a dense multiphase material with a controlled nano-structure should provide a great boon to thermoelectrics research. The high-pressure synthesis technique provides an method to mix two thermoelectric materials without homogenizing them. Both the two-phased solid and the network of nano-scale grains provide powerful tools for minimizing the thermal conductivity of a thermoelectric device component.

Contents

List of Figures

List of Tables

Chapter 1

Theory and Applications of Thermoelectrics

1.1 Overview of Thermoelectrics

Thermoelectric devices have provided useful service since Thomas Seebeck's accidental 1820s discovery, that a junction between any two metals (bi-metallic couple) will generate a potential as a function of the temperature at that junction, was put into practice [1-5]. Seebeck himself believed the effect to be a magnetic field induced by the temperature gradient, and Seebeck's original experiment observed the effect with the assistance of a compass needle in the configuration shown in Figure 1.1. This experimental setup biased Seebeck's thinking towards characterization of a thermomagnetic effect instead of a thermoelectric effect. We now understand that the observed magnetic effect was a by-product of the induced electrical current driven by the potential gradient that developed in response to the applied thermal gradient.

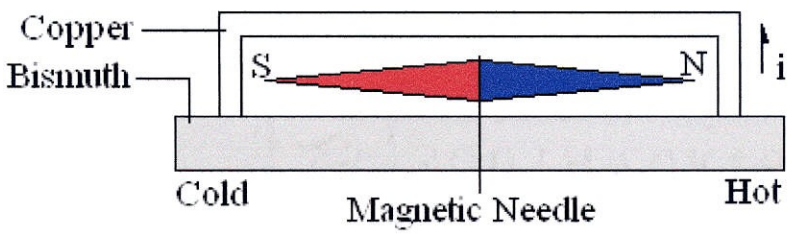

Figure 1.1: Schematic of the experimental apparatus used for the initial experiments demonstrating the Seebeck effect. The entire bismuth bar was approximately one foot from end to end, with an eight inch compass needle. The magnetic compass needle deflected in response to the electric field created by the current flow around the bi-metallic circuit.

Once the effect had been studied and reproduced by others it was cast into this form:

$$V = S(T_h - T_c) \tag{1.1}$$

where V is the potential, S is the constant of proportionality relating the temperature gradient to the potential for the bi-metallic couple in question, and T_h and T_c are the hot and cold temperatures forming the temperature gradient. Once the value of S for a given bi-metallic couple has been calibrated, it becomes possible to use that couple as a device to measure temperatures quickly, easily, and precisely. One such early thermocouple was a Pt-$Pt_{0.9}Rh_{0.1}$ thermocouple, established in 1885 by Henri Le Châtelier, which served as a standard for temperatures up to the melting point of silver until the adoption of the International Practical Temperature Scale in 1968 (IPTS-68) [6, 7]. In 1834 the Peltier effect was discovered, demonstrating that heat, in excess of pure Joule heating, could be added to a system by running a current through a bi-metallic couple [8]. By 1838 Lenz had demonstrated the cooling corollary, demonstrating that a bi-metallic couple was capable of serving as a heat source or sink when the appropriate current was passed through it [9]. The measure of a bi-metallic couple's ability to produce heating/cooling or electricity given the proper configuration was lumped into a Figure of Merit in 1910 by Altenkirch [10, 11] and was cast in its modern form in 1949 by Ioffe [12]:

$$Z = \frac{S^2\sigma}{\lambda} \tag{1.2}$$

where S is the Seebeck coefficient, σ is the conductivity, T the temperature, and λ the thermal conductivity of the material. This thermoelectric figure of merit, Z, represents

the suitability of a thermoelectric material for thermoelectric applications. Z is in units of inverse temperature, so it is common to multiply both sides of the equation by the temperature to arrive at a dimensionless figure of merit, ZT:

$$ZT = \frac{S^2 \sigma T}{\lambda}$$

$$S : \frac{\mu V}{K} \qquad \sigma = \frac{1}{\rho} : \frac{1}{\Omega cm}$$

$$T : K \qquad \lambda : \frac{W}{mK} \tag{1.3}$$

By the 1950s the efficiency of thermoelectric devices approached 5% and the ability to cool a solid with a Peltier junction from room temperature to below 0 °C had been established [13]. Tellurides of antimony and bismuth formed the basis for the heavily doped semiconductors that comprised the devices in these mid-20th century thermoelectric applications.

Applications, outside of the ubiquitous thermocouple, have been limited to solid state cooling or heating, and power generation. Thermoelectric devices convert thermal gradients into useful electric current or convert electric current into a heat source or sink. They can provide useful service in systems where power is in demand and waste heat in ample supply, or where temperature control is critical and power is readily available. Thermoelectric generators have been limited in application due to their relative inefficiency when compared to other power sources. They most often see service when access is difficult, the environment is extreme, and reliability is mandatory. Many

current commercial thermoelectric systems function with 3% efficiency or less [14, 15], demonstrating that the field has been largely stagnant over the past fifty years. One strength of thermoelectric devices is the ability to function without refueling. Radioisotope Thermoelectric Generators (RTGs) used in space applications rely on the radioactive decay of ^{238}Pu to provide a stable temperature of 1000 °C for the hot side and the coldness of space for the heat sink on the cold side. For any space application beyond the orbit of Mars, RTGs become one of the only options, as the power density available to solar panels drops with the solar distance cubed. While RTGs do not have great efficiency, their power density is largely independent of environment. Thermoelectric generators have participated in the NASA Apollo, Pioneer, Viking, Voyager, Galileo, and Cassini spaceflights. A cut-away view of a typical RTG can be seen in Figure 1.2 below. In the case of the Voyager spaceflights, those thermoelectric-powered probes have collected and returned data continuously over the last 27 years without inspection, maintenance, refueling or time off. The three RTGs on the Cassini spacecraft provide 720 Watts and measure 16.5 inches in diameter and 44.5 inches in length; the Cassini RTG is shown in Figure 1.3.

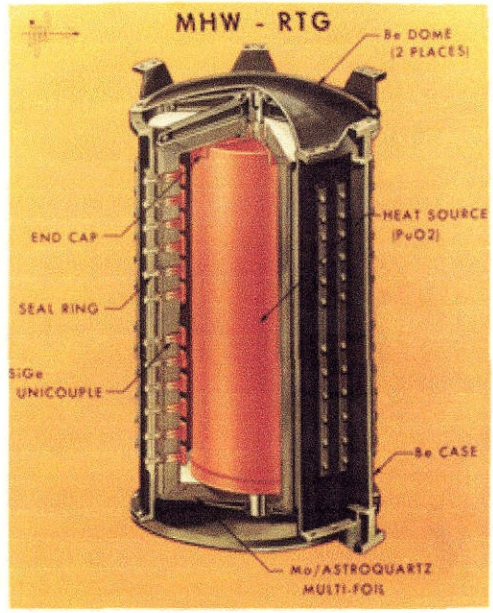

Figure 1.2: Radioisotope Thermoelectric Generator in cut-away view. SiGe unicouples surround the decaying PuO2 heat source. RTGs are modular, with each heating element approximately 1 m in length.

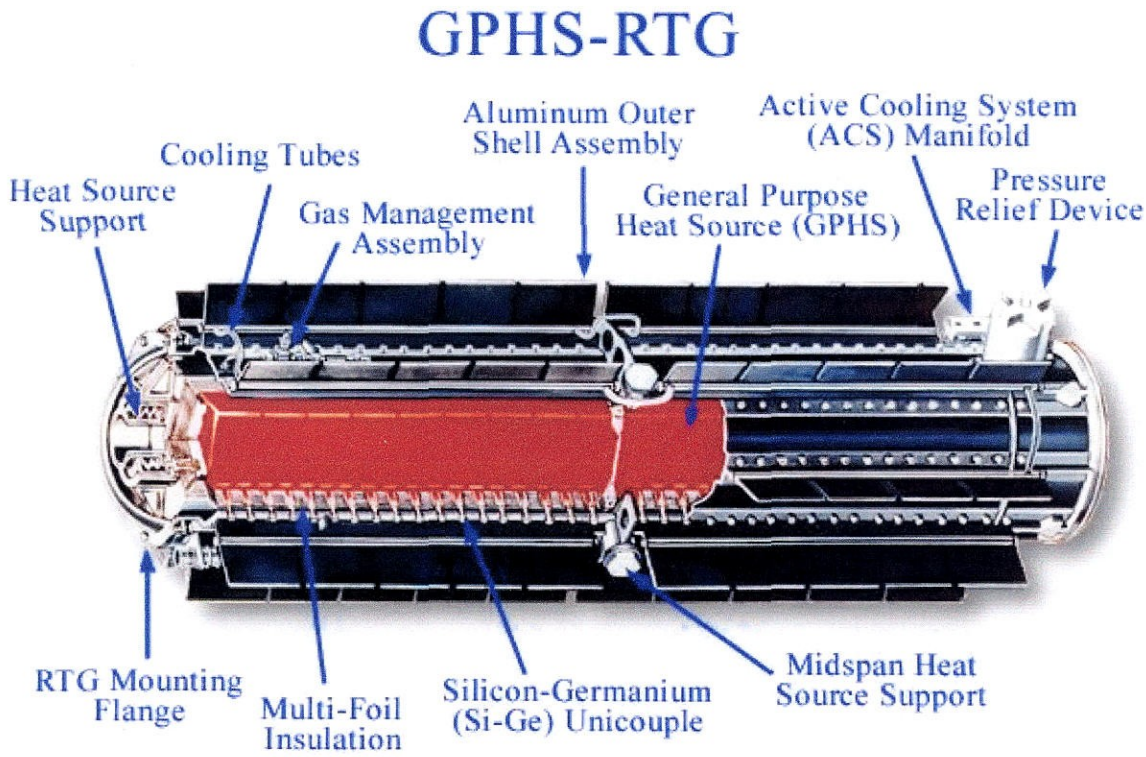

Figure 1.3: One of the three General Power Heat Source (GPHS) Radioisotope Thermoelectric Generators (RTG) onboard the Cassini Saturn mission. The three RTGs provide 720 W with a degradation of 1-2% per year. The Cassini probe, launched in 1997, has now reached Saturn and has begun sending back images of Titan's surface [16].

Contemporary applications of thermoelectric devices include cogeneration of electrical power from waste heat, microchip cooling applications, and recreational devices like coolers and food containers that warm or cool a snack without worrying about wires, access to external power supplies, or heavy cooking equipment. Of course the thermocouple remains the most common application of the thermoelectric effect, providing temperature measurement and providing a vital service to temperature control systems. While improvements in thermoelectric materials will have little impact on thermocouples, it will push thermoelectric generators and heaters into the mainstream. Much interest in the field is presently directed to converting tailpipe exhaust heat into electricity to power onboard systems in automobiles, for instance. Thermoelectrics provide spot heating or cooling on a scale appropriate to microchip applications; improving the thermoelectric efficiency in turn allows these temperature-controlling components to be packed more densely for greater heating or cooling, or into a smaller space for the same heating or cooling; both features hold merit for microchip applications.

With improving thermoelectric materials the efficiency of thermoelectric generators will come to rival that of other power generating options. Thermoelectric generators have outstanding capabilities to provide reliable standalone power or to regulate temperatures on the spot in a compact device. In situations where moving parts or consumable fuels are difficult or costly to work with – e.g., undersea, geographically remote locations, or in space, higher efficiency thermoelectrics could come to dominate power generation

markets. Many processes in our developed world produce vast quantities of waste heat and most of that heat goes unutilized. Higher efficiency thermoelectric power generation could recover much of that lost potential as the payoff begins to compete with the cost of recovering that waste heat.

1.2 The Thermoelectric Effect

1.2.1 Basics and Definitions

All materials, to varying degrees, develop an electrical potential in response to an applied thermal gradient; the strength of this response is represented by the magnitude of the Seebeck coefficient. The Seebeck coefficient is a measure of proportionality between the thermal gradient on a material and the resultant potential gradient generated in response to that thermal gradient. Charge carriers in a material have kinetic energy proportional to their temperature. Those charge carriers on the hot side of the thermal gradient will have higher kinetic energy than those on the cold side. These charge carriers will then move further between collisions and drift towards the cool side – establishing a potential gradient in response to a thermal gradient. This electrical potential can develop either parallel or antiparallel to the thermal gradient, depending on the sign of the majority charge carriers in the material. For increased efficiency thermoelectric generators pair an n-type component (electron conductor) with a p-type component (hole conductor) in the thermoelectric circuit.

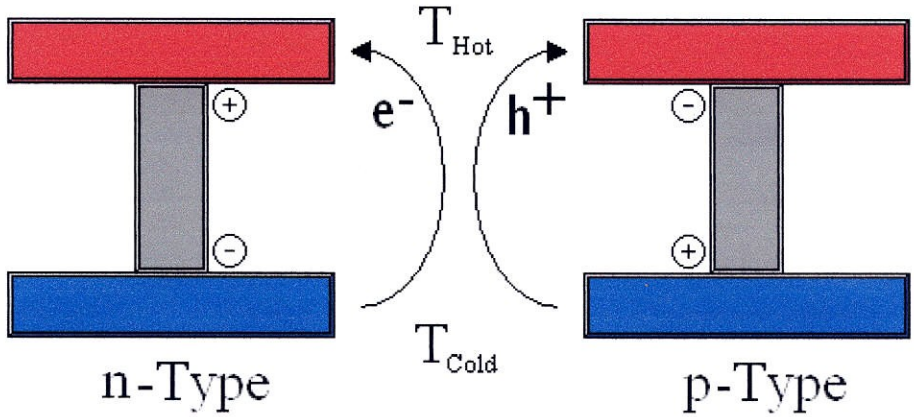

Figure 1.4: Response of n and p type materials to an applied thermal gradient. In this diagram T_{Hot} is greater than T_{Cold}. The p-Type material has a positive Seebeck coefficient (the constant of proportionality between the electric potential gradient and the thermal gradient, $S = \Delta V/\Delta T$) and develops a potential gradient parallel to the thermal gradient. The n-Type material has a negative Seebeck coefficient and develops a potential gradient antiparallel to the thermal gradient.

A thermoelectric unicouple is the basic element of a thermoelectric generator, consisting of an n-Type and a p-Type leg connected in series. The external circuit, through which power is drawn out of the generator, connects the n and p legs, typically on the cold side of the generator.

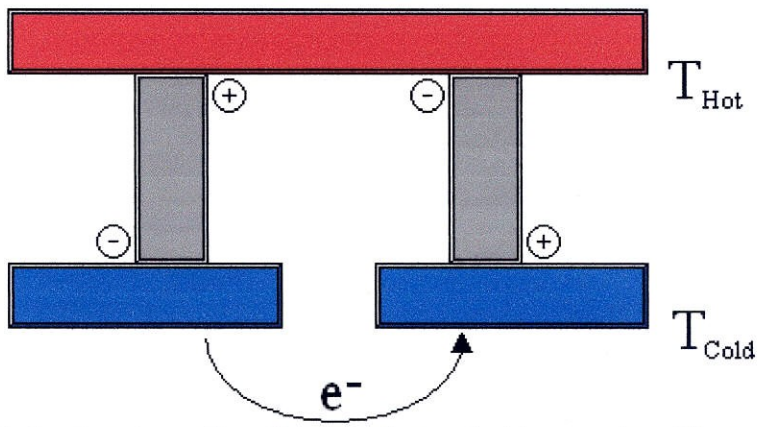

Figure 1.5: Typical unicouple configuration for a thermoelectric generator. The n and p-type legs are connected in series at the hot end and across the external circuit at the cold end, allowing power to be extracted from the thermoelectric generator.

To assure a strong current (large and steady), the Seebeck coefficient of the materials must be high, and the resistivity and thermal conductivity must both be low. Some of

these attributes come at the cost of one another in most materials systems. If the electrical conductivity is too low the charge carriers may not be free to carry much current at all, a poor design characteristic for a power generator. High electrical conductivity, however, tends to carry with it significant thermal conductivity since typical conductors have simple structures with low phonon scattering as well as thermal conduction via the majority charge carrier. If the thermal conductivity is too high, or the heat reservoirs are too small, the thermal gradient necessary to generate steady state power can collapse. These are some of the pertinent concerns in the search for new materials for thermoelectric generator applications.

1.2.2 Seebeck Coefficient

The Seebeck coefficient is a measure of proportionality between the thermal gradient on a material and the resultant potential gradient generated in response to that thermal gradient. The basic demonstration of the Seebeck coefficient can be seen in Figure 1.6 below.

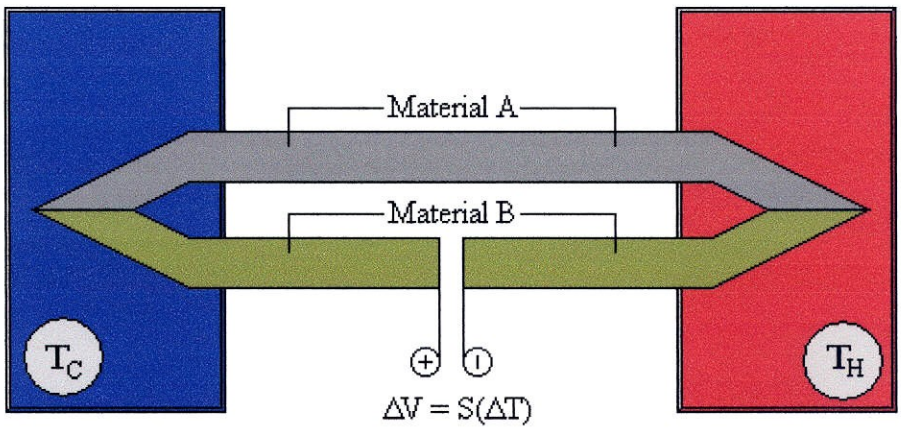

Figure 1.6: Simple configuration for the observation of Seebeck coefficient. When the temperature across the terminals is the same, the potential produced across the terminals of an open circuit made from two metals produces a temperature difference directly proportional to the difference in temperature between the hot and cold junctions.

Each end of a bi-metallic couple is maintained at a different temperature (and the terminals maintained at the same temperature) and the voltage across the gap is related to the difference in temperature difference between the two junctions by a constant of proportionality – the Seebeck coefficient. If a conductor is heated at one end the charge carriers at the hot junction will acquire increased thermal energy relative to those at the cold junction. The charge carriers from the hot end will diffuse to the cold end where their energy may be lowered; in other words, the temperature gradient creates a gradient in chemical potential of the charge-carrying species. This is one mechanism of heat conduction in metals and it is accompanied by the accumulation of charge carriers at the

cold end, thus establishing a potential difference between the ends of the material. This electric potential will build up until a state of dynamic equilibrium is established between the charge carriers biased to diffuse towards the cold end and the electrostatic repulsion due to the excess of charge at the cold end. The number of charge carriers passing through a cross section of the wire per second in both directions will be equal, but the kinetic energy of charge carriers passing from the hot to the cold end will be higher than the kinetic energy of charge carriers traversing from cold to hot. This difference ensures that there is a continuous transfer of heat down the temperature gradient without net charge transfer once dynamic equilibrium is established. From this we have the basis for the flow equations that will generate the familiar equation for the Seebeck Coefficient.

Electrons and phonons bring heat from the hot side to the cold side, but the electrons also produce a potential gradient as they accumulate. Once the gradient in electric potential opposes that from the chemical potential gradient, only heat transported via phonons and that associated with particle migration in a thermal gradient continues to flow. An electron-current-flux equation including the thermal gradient effects will look like this

$$j_e = |e| D_e[\frac{\partial n}{\partial x} + \frac{en}{kT}\frac{\partial \phi}{\partial x} - \frac{nH^*}{kT^2}\frac{\partial T}{\partial x}] \tag{1.4}$$

At steady state $j_e = 0$, and we can rearrange equation 1.4 to yield the Seebeck Coefficient S,

$$S = \frac{\partial \phi}{\partial T} = \frac{\partial \phi / \partial x}{\partial T / \partial x} = [-\frac{k \partial \ln n}{\partial (1/T)} + H^*] \frac{1}{eT}$$

$$S = [-\frac{k \partial \ln n}{\partial (1/T)} + H^*] \frac{1}{eT}$$

[17] (1.5)

Values for the Seebeck coefficient range from 0 to ±1 mV/K, with common thermoelectric materials falling in the 0 to ±200 μV/K range. Table 1.1 shows some values of the Seebeck coefficient for a variety of materials.

Material (Pure Elements)	Seebeck Coefficient (μV/°K)	Material (Compounds)	Seebeck Coefficient (μV/°K)
Aluminum	3.5	Zn_4Sb_3	200
Antimony	47.0	PbS	
Bismuth	-72.0	Bi_2Te_3	200
Cadmium	7.5	$Si_{0.8}Ge_{0.2}$ *n*-type	-500
Carbon	3.0	$Si_{0.8}Ge_{0.2}$ *p*-type	400
Copper	6.5	$IrSb_3$	77
Germanium	300.0	$CoSb_3$	190
Gold	6.5	$Ce_{0.05}Co_4Sb_{12}$	-190
Iron	19.0	$Ce_{0.25}Co_4Sb_{12}$	-110
Lead	4.0	PbTe	-350
Mercury	0.6	$Pb_{0.9}Sn_{0.1}Te$	-175
Nickel	-15.0	$Pb_{0.95}Sn_{0.5}Se$	-210
Platinum	0.0	$Sr_8Ga_{16}Ge_{30}$	-300
Potassium	-9.0	ZrNiSn	-300
Rhodium	6.0		
Selenium	900.0		
Silicon	440.0		
Silver	6.5		
Sodium	-2.0		
Tantalum	4.5		
Tellurium	500.0		
Tungsten	7.5		

Table 1.1: Values for the Seebeck Coefficient of various materials.

1.2.2 Electrical Conductivity

Electrical conductivity at the simplest level is the product of the number of charge carriers, the charge per carrier, and the charge mobility. The electric-current density j is the charge transported through a unit area in a unit time. If the number of charged particles of type i per unit volume is n_i and those particles have a drift velocity v, and charge per particle $z_i q$, where z_i is the valence and q is the fundamental charge, then the electric-current density is given by

$$j_i = n_i z_i q v \tag{1.6}$$

The electrical conductivity σ_i is the electric-current density due to i particles per electric field strength, but the drift velocity also depends on the local field strength, so we introduce the mobility μ_i, the ratio of the drift velocity to the electric field intensity:

$$\sigma_i = n_i z_i q \mu_i \tag{1.7}$$

Unfortunately, as the field goes to zero and the particle moves at constant velocity we end up with infinite conductivity. The solution to this is the relaxation time approximation, which acts as a drag force on the moving charge and represents the time required to return to equilibrium. Under the relaxation time approximation the conductivity is

$$\sigma = \frac{n z^2 q^2 \tau}{m} \tag{1.8}$$

where τ is the relaxation time and m is the particle mass.

Metallic conductors have a fixed ratio between electrical and thermal conductivity, meaning a very large Seebeck coefficient would be required to produce a high efficiency device from metals. Most metals, some of which can be seen in Table 1.1, have low Seebeck coefficients, making them poor choices for high-performance thermoelectrics. Outside of the metallic case, the Wiedemann-Franz law no longer describes the entire conduction process, and the electrical and thermal conductivities can be partially decoupled. A more detailed understanding of the conduction process is then required to produce a high performance thermoelectric by selectively decreasing the thermal conductivity without drastically decreasing the electrical conductivity. The Wiedemann-Franz law describes a very general relationship between conduction electrons and the thermal conductivity associated with them

$$\lambda = \frac{\pi^2}{3}\frac{k^2}{q^2}T\sigma \tag{1.6}$$

Each electron carries with it a charge q and the current per unit field will be proportional to q^2. The thermal conduction carried by each electron will be its thermal energy, kT. The heat current per unit thermal gradient will be proportional to k^2T. The ratio of the electrical conduction to the thermal conduction must be proportional to k^2T/q^2. The constant of proportionality $\pi^2/3$ comes from the limit on participating electrons, specifically those near the Fermi surface.

Material	Electrical Resistivity (mΩcm)	Material	Electrical Resistivity (mΩcm)
Aluminum	2.45	Potassium	6.1
Antimony	39	Silver	1.51
Bismuth	107	Sodium	4.2
Cadmium	6.8	Tellurium	15
Copper	1.56	SiO2	. 10^{19}
Gold	2.04	Germanium	$4.7x10^{4}$
Iron	8.9	Silicon	$2.3x10^{8}$
Lead	19	GaAs	. 10^{11}

Table 1.2 Electrical resistivity for various metals and thermoelectric materials [39, 40].

1.2.3 Thermal Conductivity

The Wiedemann-Franz law relates the electrical conductivity to the thermal conductivity, but that relation does not hold when electrons and phonons interact with energy of *kT*. Breaking the contributions down to the various components will help illustrate where the thermal conductivity can be modified independently of the electrical conductivity. A general form of the thermal conductivity is

$$\lambda = \lambda_L + \frac{\left(\frac{5}{2} - s\right)k^2\sigma T}{q^2} + \frac{k^2\sigma T\left(5 - 2s + {}^{E_g}\!/_{kT}\right)^2 np\mu_n\mu_p}{\left(n\mu_n + p\mu_p\right)^2} \tag{1.7}$$

The three terms represent the lattice, electron, and mixed conductor contributions to the thermal conductivity. The Wiedemann-Franz relationship can be seen in the electron and mixed contributions, but it is missing from the lattice contribution to the thermal conductivity. The lattice thermal conductivity is a combination of the acoustic and optical phonon modes in the crystal and requires no interaction from the charge carriers.

Material	Thermal Conductivity (W/cmK)	Material	Thermal Conductivity (W/cmK)
Aluminum	2.38	Potassium	1
Antimony	0.18	Silver	4.18
Bismuth	0.09	Sodium	1.38
Cadmium	1	Tellurium	0.5
Copper	3.85	SiO2	0.014
Gold	3.1	Germanium	0.6
Iron	0.8	Silicon	1.5
Lead	0.38	GaAs	0.46

Table 1.3 Thermal conductivity for various metals and thermoelectric materials [39, 40].

1.2.4 Thermoelectric Figure of Merit

The primary tool for comparison of thermoelectric materials is the dimensionless figure of merit, ZT (Equation 1.3). The dimensionless figure of merit is proportional to the Seebeck coefficient squared, the temperature, and the electrical conductivity (or inversely proportional to the resistivity) and inversely proportional to the thermal conductivity. Typical ranges in ZT are from zero, for poor thermoelectric materials, to 1.5 for high performance thermoelectric materials (Figure 1.7). Some examples of thin film thermoelectrics have been reported with ZT values reaching 2.5 or above [18], but these for the most part rely on thin film effects for their high efficiency thus limiting their general applicability to large-scale power generation problems. ZT depends on several material characteristics and does not have any theoretical upper limit; any value above ZT = 1.5 for a bulk material is seen as a very encouraging result.

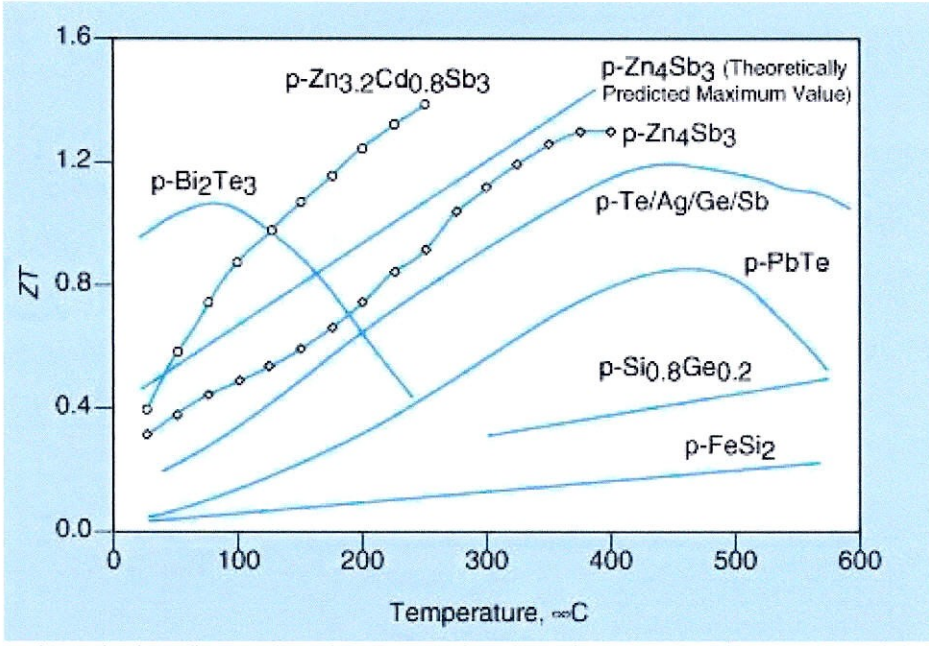

Figure 1.7 Dimensionless figure of merit, ZT, as a function of temperature for a variety of thermoelectric materials [19].

There are some well-known systematic behaviors and trade-offs that affect the thermoelectric figures of merit of various materials. One important factor, although it does not appear directly in the ZT formula, is carrier concentration; one can readily see why thermoelectric research is concentrated in semiconductors instead of metals or insulators. Although thermoelectric properties were first put to use with metal systems, forming the basis of thermocouple operation, the high associated thermal conductivities make for poor thermoelectric generators. In the case of insulators, insufficient current flows for use in power generation. The various terms in the figure of merit, as plotted against carrier concentration, and therefore on an Insulator-Semiconductor-Metal axis, can be seen in Figure 1.8.

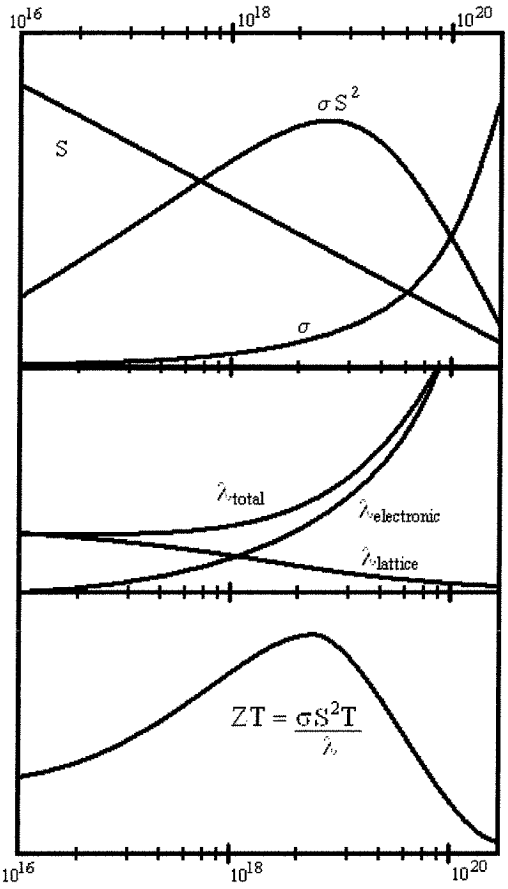

Figure 1.8: As the carrier concentration increases from insulator through semiconductor to metal the Seebeck coefficient drops linearly. The conductivity increases sharply as the material becomes metallic. The total conductivity increases sharply as well with increasing carrier concentration. The ZT, however, peaks between 10^{18} and 10^{19} charge carriers per cubic centimeter, in the range of doped semiconductors.

Alloying two thermoelectric materials is a common route to improving ZT, as reducing the phonon thermal conductivity through alloying is a proven approach [9]. The direct positive impact on the power-factor is slight as the alloy can have a lower conductivity than the end members; however the positive impact on ZT from the strongly reduced thermal conductivity is significant. The alloy of two thermoelectric materials can yield a new thermoelectric material with far better properties than the constituent parts, as shown in Figure 1.9.

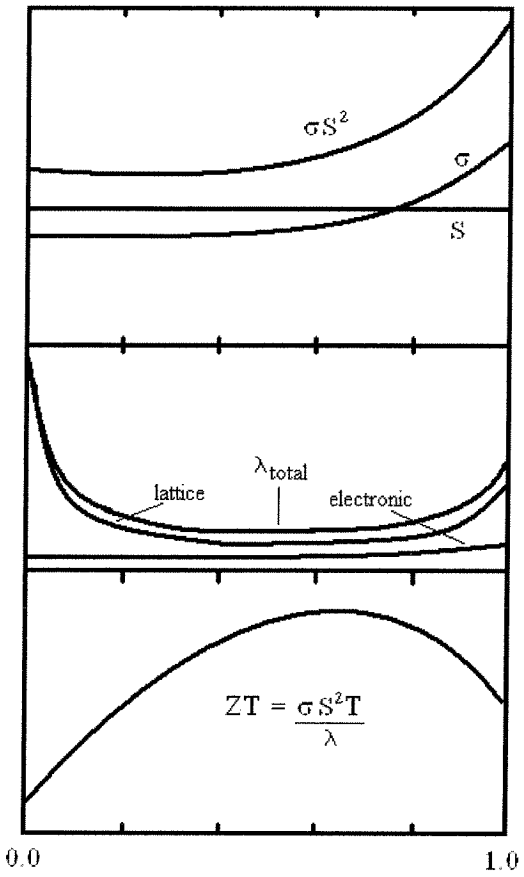

Figure 1.9: Impact of alloying on the components of ZT as a function of alloy composition for an arbitrary thermoelectric alloy. While the impact on the Seebeck coefficient is slight and the conductivity suffers an unfavorable mixing, the thermal conductivity is quickly and significantly reduced with alloying. As a result the figure of merit increases rapidly with alloy composition.

1.2.5 Thermoelectric Generators

A thermoelectric generator converts a thermal gradient into an electrical current. Thermoelectric generators are limited firstly by the operating differential in temperature that is available, and secondly by the materials appropriate for that temperature range. The highest common thermoelectric operating temperatures are the 900-1000 °C range. These generators are usually $Si_{0.8}Ge_{0.2}$ based devices [37]. Mid-range thermoelectric generators, operating at up to 700 °C, are beginning to utilize several recently developed skutterudite and filled skutterudite compounds [35].

1.2.7 Thermoelectric Generator Efficiency

The voltage generated as a result of the thermal gradient and Seebeck coefficient yields the useful potential for power generation

$$V = S\Delta T. \tag{1.7}$$

The electrical power (P) that can be extracted from this voltage is

$$P = \frac{V^2}{R} = \sigma(S^2\Delta T^2), \tag{1.8}$$

where R is the electrical resistance of the material (σ=1/R). The temperature gradient across the generator results in transport of heat by thermal conduction from the hot end to the cold end of the device. This heat flux (Q) is given by

$$Q = \lambda\Delta T \tag{1.9}$$

where λ is the thermal conductivity of the material. The ratio of power output to the heat transported gives a measure of the efficiency of the device. As can be seen from the previous two equations, this ratio produces the thermoelectric figure of merit Z (eq. 1.2) times the temperature gradient.

$$\frac{P}{Q} = \frac{S^2\sigma\Delta T}{\lambda} = Z\Delta T = \eta \tag{1.10}$$

Like all heat engines, thermoelectric generators are bound by the Carnot limit on efficiency

$$\eta_{Carnot} = \left(\frac{T_{Hot} - T_{Cold}}{T_{Hot}} \right) = \frac{\Delta T}{T_H} \tag{1.11}$$

The device efficiency (η_D) for a thermoelectric generator is given by

$$\eta_D = \left(2 + \frac{4}{ZT_H} + \frac{\Delta T}{4T_H} \right)^{-1} \tag{1.12}$$

The thermoelectric generator efficiency is then given by the Carnot efficiency multiplied by the device efficiency (η_D).

$$\eta = \eta_C \eta_D = \left(\frac{\Delta T}{T_H} \right) \left(\frac{1}{2} + \frac{ZT_H}{4} + \frac{4T_H}{\Delta T} \right) \tag{1.13}$$

From Equation 1.13 it is easy to see the usefulness of the dimensionless figure of merit, ZT. The device efficiency of a hypothetical thermoelectric generator depends directly on this dimensionless factor. The two routes for improving thermoelectric generator efficiency are then improving η_C by improving the temperature differential and improving η_D by improving the thermoelectric figure of merit, ZT.

1.3 Skutterudite Thermoelectrics

Skutterudite, in the strict sense, is a natural mineral with end-member composition $CoAs_3$. Substitutions on the various sites in the skutterudite structure lead to a large family of Skutterudite-structured materials generically called "Skutterudites." Skutterudites are of interest for thermoelectric applications for the high power factors ($S^2\sigma$) present in the binary compositions. Binary Skutterudites also have very high thermal conductivities, preventing their use as thermoelectric materials as they appear in nature. A second advantage of the skutterudite structure, only revisited in the last 15 years, is the incredible flexibility provided by the structure. Most Skutterudite thermoelectrics make use of this structural freedom to selectively reduce the thermal conductivity while maintaining the appealing power factor characteristics of the binary systems.

1.3.1 Phonon Glass - Electron Crystal (PGEC) Approach

The large voids in Skutterudite form cages into which atoms may be inserted. Many workers [20-22] have hypothesized that the heavy atoms, often rare earth atoms, inserted into these cages will rattle around, disrupting the phonon modes in the system and reducing the thermal conductivity. The notion is that electron conduction and lattice thermal conduction are sensitive to different time scales and that conduction electrons (or holes) do not see the perturbation of the rare earth rattling on their time scale, whereas the thermally conducting phonons are frustrated by it. This is, in broad strokes, the electron crystal - phonon glass description of the ideal thermoelectric material, and possibly of a

suitably optimized skutterudite structure. The key here is that the ion sitting in the large void vibrates out of phase with the lattice. This results from the very large size of the void relative to the ion and the relatively weak binding of that interstitial atom.

1.3.2 Structural Features of Skutterudites

Interest in Skutterudites is due in part to the open cages in the crystal structure. These large voids are often filled with rare earth ions in an attempt to modify the thermal or electrical properties of the material. Skutterudite is a cubic system (IM3) with 36 atoms per unit cell. The structure includes two large voids per unit cell as illustrated in Figure 1.10. The remaining six octants of the structure contain four member rings of pnictides, while a cubic framework of transition metal cations bounds the cell.

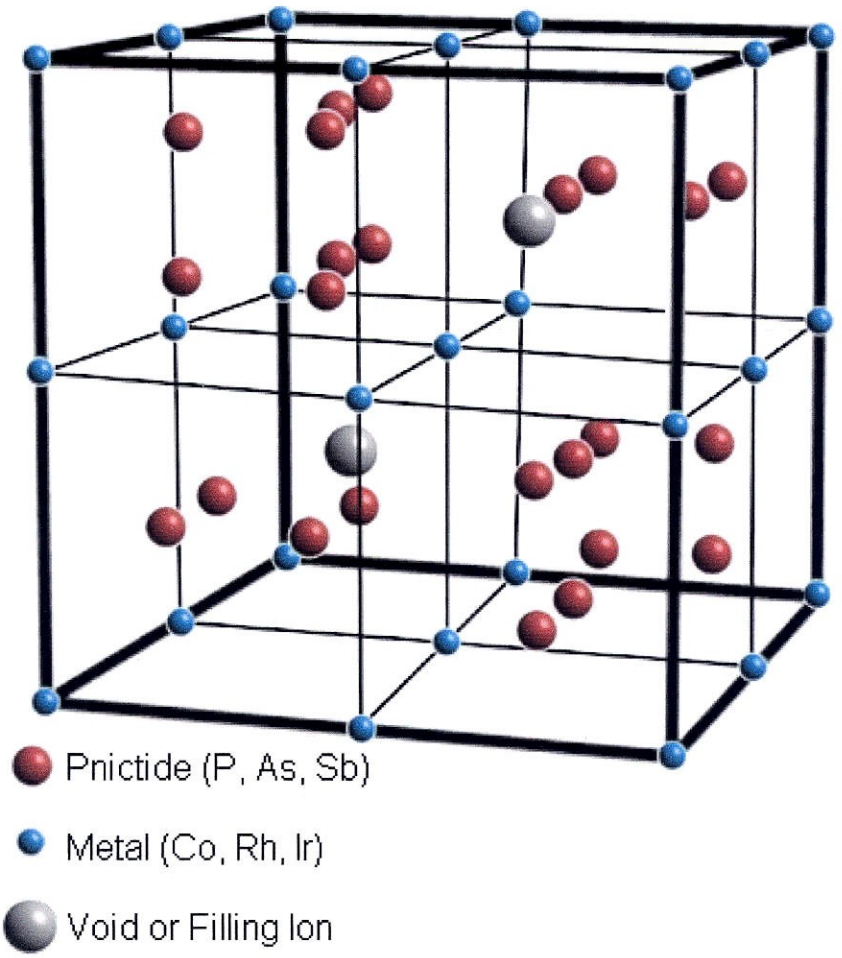

Figure 1.10: The crystal structure of Skutterudite. The two large voids in the structure are often filled or partially filled with rare earth atoms as indicated.

Unlike many other thermoelectric systems, such as Bi_2Te_3 and PbTe, skutterudites allow many isostructural compounds. In the skutterudite family 11 binary compounds and many solid solutions exist, as well as many more skutterudite related phases [23]. One method of predicting semi-conducting behavior in candidate skutterudite compositions is to consider a simple bonding scheme where each transition metal contributes 9 electrons and each pnictide contributes 3 to the covalent bonding. This sum is known as the Valence Electron Count (VEC) [37, 38]. When the contributions are summed over the

unit VT_4Pn_{12}, where V represents the void, T represents the transition metal site, and Pn represents the pnictide site in skutterudite, the (VEC) for a semiconducting skutterudite will equal 72. Filled skutterudites fit into the VEC by replacing the void with a filling ion, which contributes its valence electrons (3 for many rare earth atoms) to the sum. VEC values of 71 or 73 result in metallic behavior, but the VEC scheme will only work when the atoms in the structure are behaving in accordance to the simple bonding scheme laid out.

1.3.3 Substitution in Skutterudites

The skutterudite structure is also very accommodating to a variety of substitutions on existing occupied sites in the structure. Skutterudite is a naturally occurring mineral, originally found in Skutterud, Norway. In the naturally occurring mineral it is found with a composition of (Co, Ni)As_{3-x}, empirically as: $Co_{0.75}Ni_{0.25}As_{2.5}$ [24]. For the transition metal site many different transition metals can be substituted. Commonly cobalt, nickel, iridium, iron, ruthenium, rhodium and palladium can be substituted on the transition metal site for synthetic skutterudites. The pnictide site also has wide substitution possibilities with potassium, arsenic, antimony, bismuth, tin, germanium, and tellurium making up most of these compositions. Substitution on the transition metal or pnictide sites is typically performed in order to dope the electrical properties of the material (most notably the carrier concentration), or to encourage void filling in the structure.

1.3.3 Void Filling in Skutterudites

Void filling in skutterudite systems is promising due to the extremely large void located in two of the octants of the skutterudite structure. These sites, 2a crystallographic sites in the IM3 structure, have a diameter that varies from 1.763 to 2.037 Angstroms for several common compositions as shown in Table 1.4.

Skutterudite Void Radius	
Binary Composition	Void Radius (Å)
CoP_3	1.763
$CoSb_3$	1.892
$RhAs_3$	1.934
$IrSb_3$	2.037

Table 1.4: Size of the void in Skutterudite for a variety of different skutterudites [25].

This is a very large void in the structure capable of accommodating many different impurity additions. Rare earth lanthanides are most commonly selected as filling ions [26-30], but thallium and uranium [30, 31], as well as calcium, strontium, and barium [30, 32] have also been explored.

One advantage of rare earth ions is their unambiguous position in the structure. Other filling ions can substitute onto the transition metal site as well as the void site, or even the anion site in the case of tin-filled cobalt antimonides. The range for candidate filling atoms in skutterudites depends on the radius of the void and the radius of the filling ion. Filling generally occurs when

$$1.0 \geq \frac{Ion\ Radius}{Void\ Radius} \geq 0.67 \tag{1.14}$$

For 8-coordinated trivalent cerium (radius = 1.283 Å) in $CoSb_3$ skutterudite, a composition of interest for much of this work, the ratio is 0.678, barely qualifying for this filling criteria. Experimental evidence suggests that under standard synthesis techniques there is a limit to the filling allowed for cerium in a $CoSb_3$ skutterudite of about 10% unless a substitution of iron for cobalt is made. In an iron-cobalt skutterudite system full cerium filling is achieved at $CeFe_4Sb_{12}$, while the cerium content drops off strongly with cobalt substitution [33]. This joint operation of substitution and void filling has been the dominant method of obtaining high filling fraction skutterudites for study. Nine ternary skutterudite compounds have been reported in the literature and at least 17 more have been discovered [34].

1.4 Skutterudite Thermoelectrics

The current state of the art for skutterudite thermoelectrics involves the use of segmented unicouples and a variety of filled and unfilled skutterudite compositions. One such couple, built at JPL, is illustrated at the left in Figure 1.11. With segmented thermoelectrics such as these the Thermoelectrics Group at JPL has recently demonstrated conversion efficiencies of up to 15% in the 25-700°C temperature range [35]. Skutterudites are limited to moderate temperature ranges, and can only work with high temperature thermoelectric materials in a cascade configuration as shown at the right in Figure 1.11.

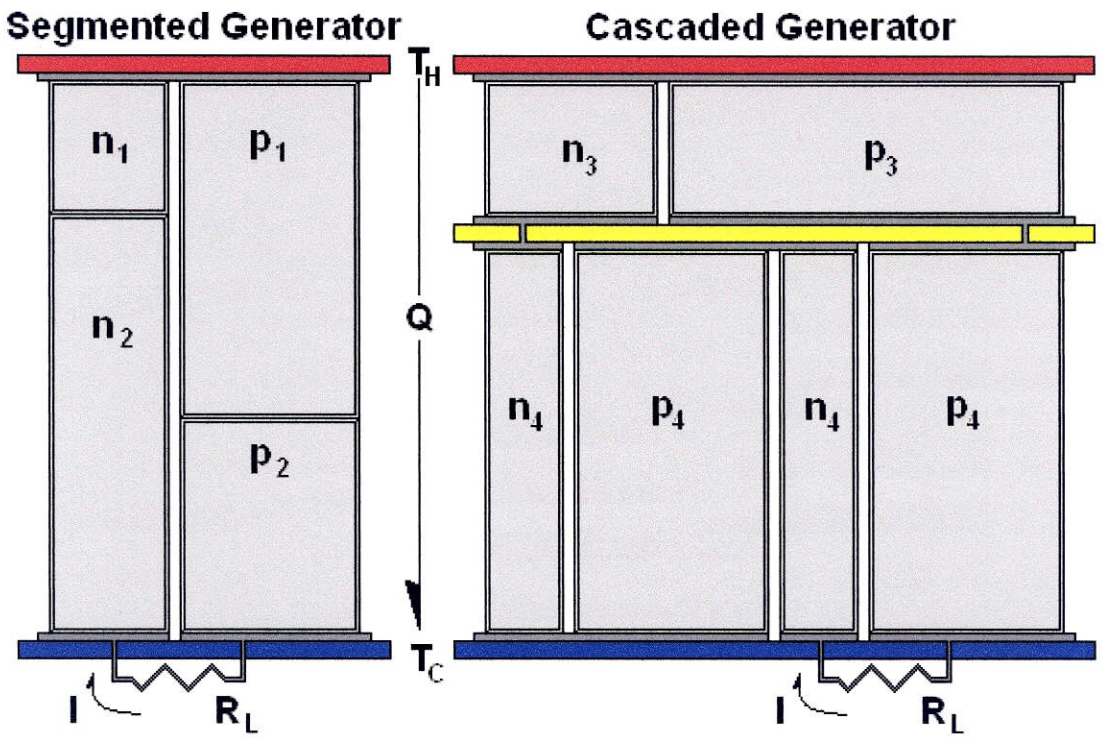

Figure 1.11: Schematic of segmented and cascaded thermoelectric generator configurations. In the segmented configuration the materials' compatibility must match well or the performance will suffer across each junction. The cascaded configuration allows for the use of mismatched materials to span a large temperature differential [36].

While in both designs a high-temperature material is coupled with a lower-temperature material, in the segmented case the materials must be compatible. The segmented generator combines high and low temperature thermoelectric components in straightforward junctions: n_1:n_2 and p_1:p_2 as in Figure 1.11. Since the cross section is constant from the hot side to the cold side along each leg of the segmented unicouple, it is important that the materials have similar transport properties, such as current density. In a cascaded thermoelectric device mismatched materials can be used to span a given temperature gradient. The cascade design allows the transitions between high temperature and low temperature materials to normalize current densities in an attempt to reduce the deleterious effects of the mismatch. By splitting the temperature gradient into

separate temperature drops each one can support the best possible material for that temperature range.

The current direction in skutterudite thermoelectric research is to search out solid-solutions of filled skutterudites in order to maximize all possible components of thermal conductivity reduction. Combinations of filled and unfilled phases provide the maximum mass differential for phonon scattering, while the metal substitutions often employed to encourage void filling can produce beneficial electrical transport properties. These mixed and multi-component skutterudites often have moderately low melting points and poor thermal stability, requiring the use of segmented or cascaded generator designs.

Chapter 2

Experimental Methods

2.1 Synthesis

Synthesis of the materials reported in this work required multi-step procedures including (1) possible high-temperature, low-pressure alloying; (2) either solid-state medium-temperature, low-pressure reaction or high-temperature, low-pressure melting and quench; (3) in many cases, medium-temperature, high pressure reaction; (4) in some cases, re-powdering and physical cold-pressing.

2.1.1 Precursors and Initial Processing Steps

Initial synthesis in all the skutterudite systems combined high purity elemental precursors at elevated temperatures. Typically these were cerium chunk, antimony shot, and cobalt, ruthenium, and rhodium powders. These precursors were stored in a glove box under argon to prevent oxidation of the metals. Synthesis of cerium-containing compositions first required alloying of all metal precursors with the aid of a radio-frequency induction furnace at a temperature of 1400 °C for 30 seconds. This alloying step was to ensure that the metals would not oxidize during the balance of the synthesis process. The alloyed metals were then combined with antimony shot and prepared for the main ambient-pressure synthesis step.

2.1.2 Ambient-Pressure Synthesis

During both the solid-state reaction and quench synthesis methods the precursors were contained in boron nitride crucibles and evacuated quartz ampoules. The mixed materials were heated to 700 °C for 48 hours for the samples using the solid-state reaction synthesis and 1200 °C for 30 minutes for those samples using the quench synthesis. While the precursors are air-sensitive, the synthesized skutterudites are stable in a standard atmosphere. These low-pressure skutterudite products were typically low filling fraction skutterudites with $CeSb_2$ and $CoSb_2$ impurity phases interspersed throughout. Subsequent synthesis steps were designed to homogenize the material and remove impurity phases.

The solid-state reaction route relies upon solid–solid diffusion to arrive at a homogeneous skutterudite composition. Since the impurity phases, diantimonides, are thermodynamically stable from room temperature up to higher temperatures than the skutterudite phase they were quite difficult to remove once formed. Performing the synthesis at too high a temperature resulted in both significant antimony sublimation and diantimonide formation, while temperatures too low resulted in un-reacted precursors. In the right ratios a slightly filled skutterudite composition can be synthesized directly from the solid-state reaction method, typically for cerium contents representing 0-10% filling. This solid-state reaction synthesis route is a standard practice in the field [41-43].

The quench synthesis method circumvents some of the difficulties in the solid-state reaction method by quenching directly from the melt into a skutterudite phase. The

resulting material, although possibly containing impurity phases, is homogeneous on a finer length-scale than products of the solid state reaction route. This method was adopted during the course of this work and by the end represented the preferred initial synthesis route used in the formation of new skutterudite materials. Other researchers following similar quench synthesis methods typically rely on carbon coated quartz ampoules instead of boron-nitride crucibles sealed in quartz ampoules [44, 45]. Our experience with boron-nitride crucibles has been that the reactants do not adhere strongly to the crucible, making it a viable and simple to manage option. Quench synthesis is often followed by a regrinding and annealing at moderate temperatures to homogenize the crystal structure. This is suitable for those compositions that can be synthesized at standard pressures, like low (<10%) filling fraction skutterudites, but is not helpful for high filling fraction studies where impurity phases can consolidate into unwanted microstructural features [46].

2.1.3 High Pressure Synthesis

Most compositions in this work required high-pressure synthesis techniques, more familiar in experimental petrology than in materials research, in order to reach favorable synthesis conditions. Skutterudites with modest filling fractions could be synthesized without the high-pressure techniques used here, but for the high filling fractions targeted in this project further processing was required. Raw materials were prepared for high-pressure synthesis by milling the products of ambient-pressure solid state or quench synthesis reaction routes. Powders were milled to a particle size of 25 microns before being subjected to the high-pressure techniques. This experimental technique is rare in

materials synthesis, as very few labs have the pressure facilities on hand [51, 52], and therefore requires detailed description.

High-pressure experiments were carried out with a 1000-ton press and two multi-anvil modules, the Walker octahedral design [47] and the Getting cubic design [61]. Experimental conditions ranging up to 2500 ˚C and 25 GPa were available using the octahedral technique, and conditions of up to 2500 ˚C 6 GPa were available using the cubic technique. Two different configurations were used in part to allow a larger sample volume through the use of the lower pressure cubic device. The sample volume for the octahedral device was limited to a cylinder with diameter and length of 2.5 mm, while the cubic device allowed a sample volume with diameter and length of 5.5 mm. While the octahedral device was suitable for survey experiments, the sample volume required for properties measurement and device fabrication are more easily satisfied by the larger cubic device apparatus.

The octahedral module is comprised of a hardened steel ring with six hardened steel primary drivers and eight second stage tungsten-carbide anvils to compress the 14/8 octahedral assemblies. The 14/8 nomenclature refers to the octahedral edge length of the pressure medium and the truncation edge length of the second stage anvils in millimeters. Figure 2.1 illustrates the press and anvil configuration for the octahedral device. Two different pressure medium and gasket designs were employed. The first was a semi-sintered Cr-doped MgO octahedron containing zirconia sleeves and a graphite furnace. The octahedron was seated within the second stage anvils with the aid of pyrophyllite

gaskets with cardboard and teflon tape behind the gaskets for support and electrical insulation. The octahedra of pressure medium were imported from Japan and the twelve gaskets consumed in each experiment were individually machined and arranged on the second stage anvils making this assembly costly and time-consuming, but reliable to extreme pressures in excess of 14 GPa.

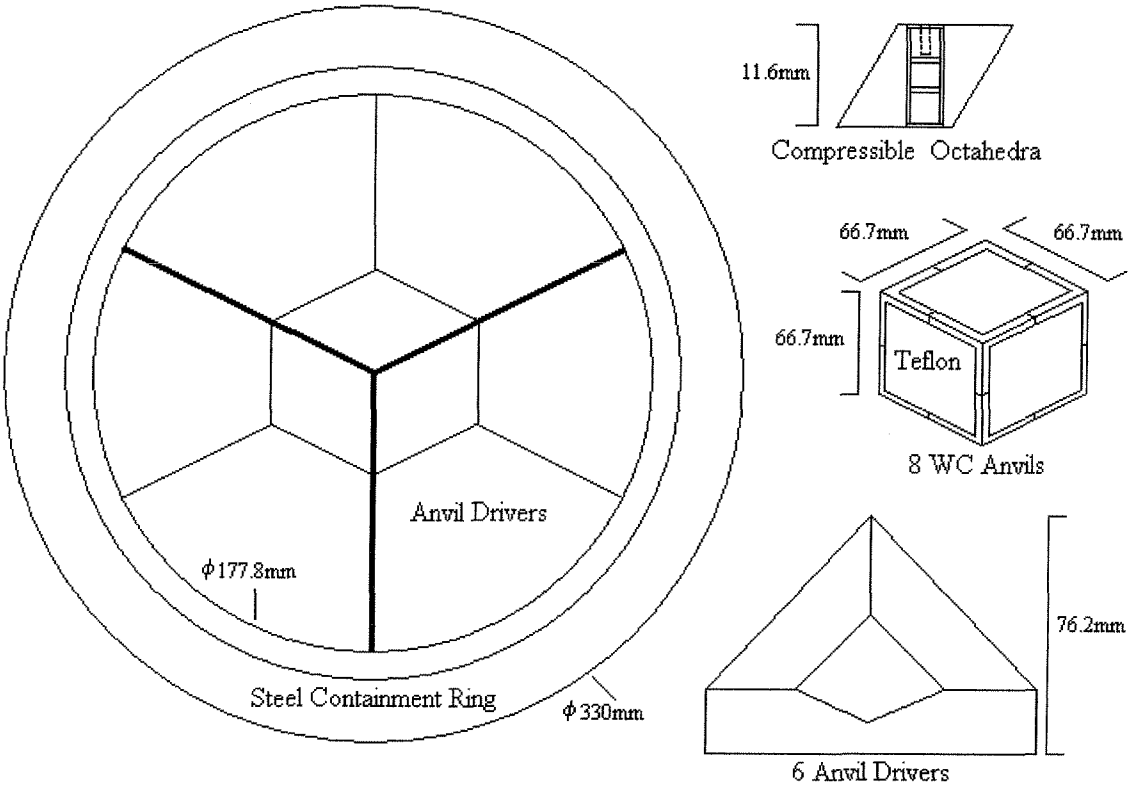

Figure 2.1: Schematic of the high-pressure octahedral assembly and press. The detail shows a break-away view of the interior of the octahedral pressure medium, showing the components in the assembly and the sample location in the device. The octahedral pressure medium is centered within the eight tungsten carbide anvils, which in turn are centered in the six anvil drivers. The device is known as a 6-8 device for the 6 primary drivers and 8 secondary drivers that, with the weak pressure medium and gasket materials, are utilized in generating the quasihydrostatic pressure on the sample.

The second pressure medium was an MgO-based cast octahedron with built-in gaskets. These pressure media simplified the gasketing in the octahedral device, were produced in-house, and could tolerate greater wear of the tungsten-carbide second stage anvils.

These pressure media were used for many exploratory experiments at moderate pressures up to 6 GPa. The assembly was also simplified to maximize the sample volume within the graphite furnace. Figure 2.2 illustrates the differences in assembly and gasketing with these two techniques.

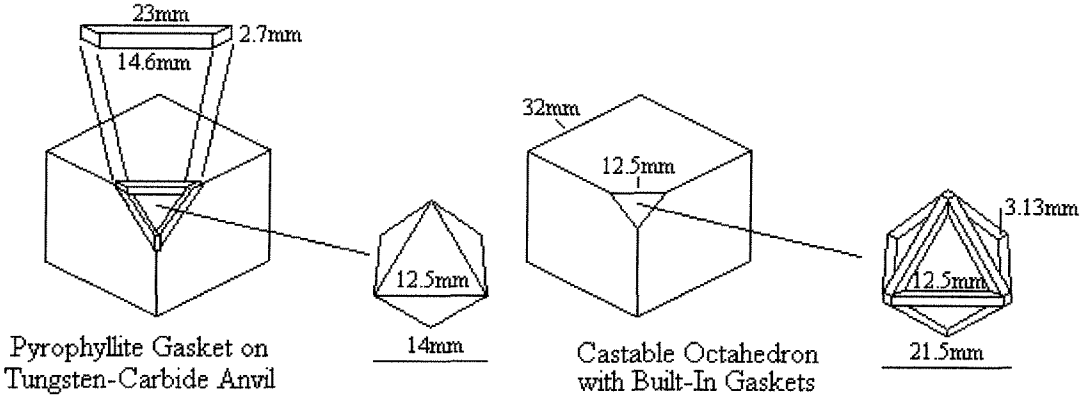

Figure 2.2: Main features of gasketing in the octahedral device, showing components of the semi-sintered octahedron and the MgO based castable octahedron [48].

The cubic device was used for the bulk of our synthesis results. The cubic module, shown in Figure 2.3, employs eight primary anvil drivers and six tungsten-carbide anvils. The pressure medium employed was a 21 mm soft-fired pyrophyllite cube. The pyrophyllite was prepared by drilling a 12.7 mm hole through the center of the cube into which a $BaCO_3$ sleeve was inserted. Inside this, a 7.7 mm outer diameter, 5.5 mm inner diameter graphite cylinder comprises the heating element. The sample was sandwiched in the central 4mm region of the hotspot between graphite disks meant to prevent contamination of the skutterudite materials. Crushable MgO spacers and molybdenum end-disks comprised the remainder of the volume in the cube, with an axially mounted thermocouple abutting one graphite disk for accurate measurement of the sample temperature.

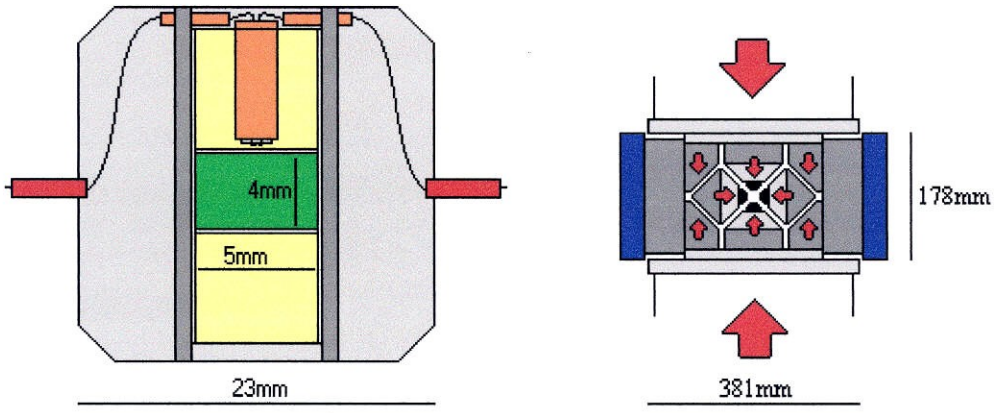

Figure 2.3: Schematic of the high-pressure cubic assembly and press. The detail in 2.3.a shows a break-away view of the interior of the cubic pressure medium, clearly showing the components in the assembly and the sample location in the device. The 8 primary drivers and 6 secondary drivers compress the weak pressure medium to generate the quasihydrostatic pressure on the sample.

Temperature in both the cubic and octahedral modules was controlled with a W5%Re - W26%Re axial thermocouple (Type C). $LaCrO_3$ furnace components with metal sample capsules are typically used in high-pressure experiments, but skutterudites react with the $LaCrO_3$ and capsule materials. In this work, graphite furnaces were used because carbon did not react with the skutterudite materials, but this limited the experimental temperatures to under 1300 °C. The use of a graphite furnace alleviated the requirement of keeping the sample separate from the furnace; this allowed the furnace to serve as the sample capsule walls and provided the greatest possible sample volume.

Calibration of high-pressure experiments was performed by bracketing well known phase transitions in P-T space. The 14/8 octahedral device was calibrated against Bi I-II, Bi II-III, and BI III-V transitions at room temperature[62], the garnet-perovskite transition in $CaGeO_3$ at 1200 °C [10], the coesite-stishovite transition in SiO_2 [63], and the forsterite-wadsleyite transition in Mg_2SiO_4 [64]. Calibration experiments began with a mixture of

high and low pressure phases across the transition being targeted. Single phase results represented experiments far from the transition point, while modest changes in the ratio of phases indicated experimental conditions very close to the transition. Calibration of the cubic device relied on observation of the Bi I-II and Bi II-III transitions, the quartz-coesite transition in SiO_2 [49], and the fayalite-ringwoodite transition in Fe_2SiO_4 [104].

Initial survey experiments were conducted over a range of pressure and temperature to find the stability limits of filled skutterudite synthesis. Starting with a mixture of filled and unfilled skutteruditescontaining dispersed metal diantimonides, under successful conditions a single filled skutterudite phase was obtained. Early in the process images such as Figure 2.4 were common.

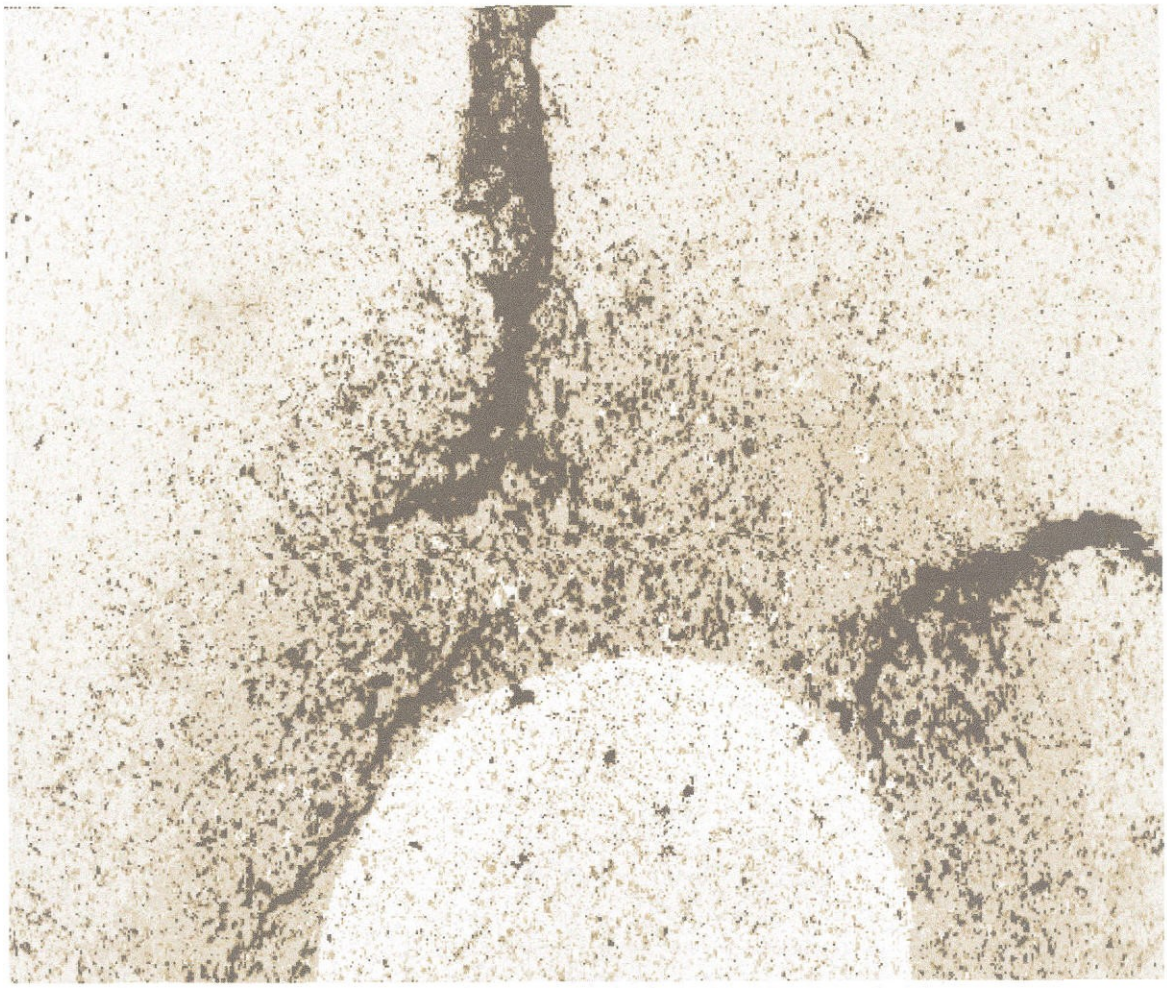

Figure 2.4: SEM micrograph of survey experiment with composition $Ce_{0.25}Co_4Sb_{12}$ at 5 GPa and 550° C. The $CeSb_2$ impurity imaged is roughly five times the radius of the initial particle size. The surrounding, darker, region is a cerium depleted region of $CoSb_3$, while the lighter matrix comprising the remainder of the sample is a filled skutterudite with composition $Ce_{0.1}Co_4Sb_{12}$. The cracking observed is attributed to the differences in temperature and pressure expansion coefficients between diantimonide and triantimonide phases.

Unsuccessful synthesis attempts resulted in further segregation between skutterudite at low filling fraction and metal diantimonide impurities. Previous work in skutterudite synthesis utilized hot pressing techniques and tended to produce better results at higher temperatures and pressures. While the pressures obtained under conventional synthesis techniques are much lower than those reached through these high-pressure techniques, the trend towards higher pressures and higher temperatures guided our initial work.

However, mapping in the cerium-filled cobalt triantimonide system showed, contrary to expectations, that the upper temperature limit above which only diantimonides were formed decreases with increasing pressure. These survey experiments suggested synthesis conditions for subsequent high-pressure skutterudite synthesis attempts, providing reliable guidelines for several skutterudite compositions. A plot of these results can be seen in Figure 2.5. Synthesis conditions of 4 GPa and 700 °C for 4 hours, followed by 450 °C for 24 hours were fairly typical for cerium filled skutterudites and well within the routine operating limits of the cubic configuration.

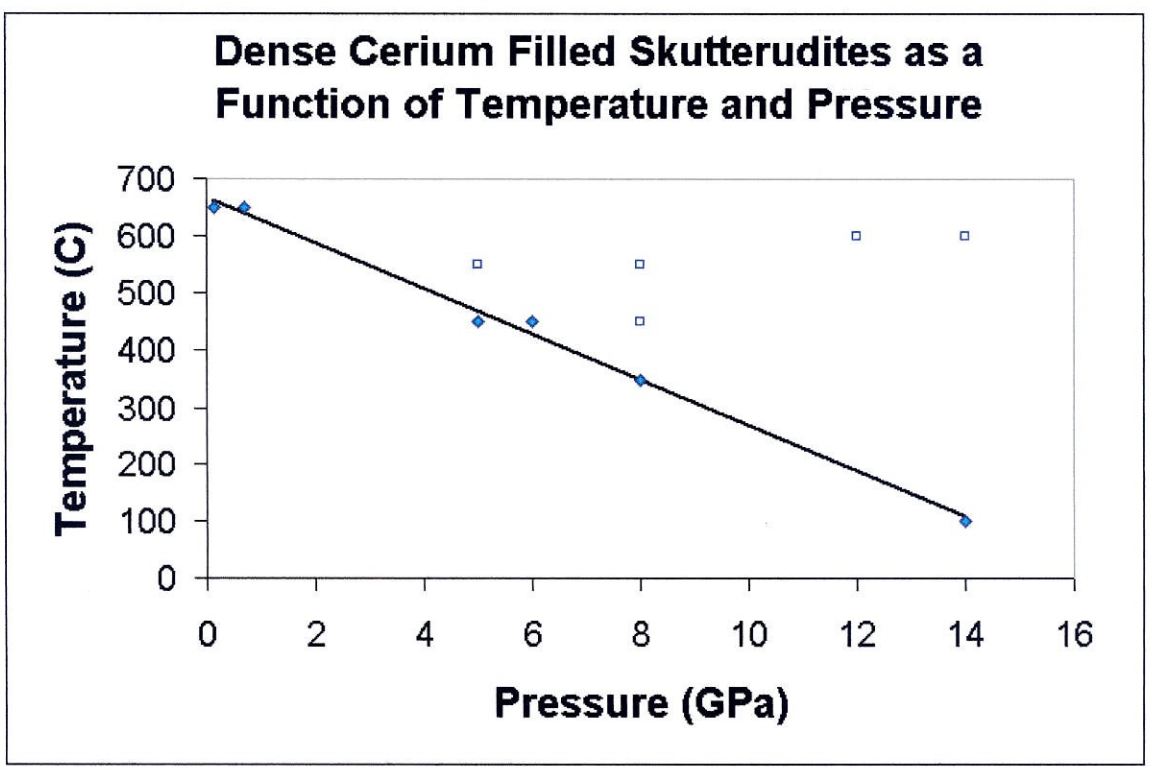

Figure 2.5 Single-phase cerium-filled Skutterudite synthesis success (closed diamonds) and failure (open squares) as a function of temperature and pressure. These data show a decreasing synthesis temperature limit with increasing synthesis pressure.

2.1.4 Regrinding and cold pressing.

After the high-pressure synthesis the skutterudite sample was extracted from the press and the crushable pressure medium surrounding it. Due to the deformation of the cube, the recovered sample was not typically a regular cylinder 4 mm tall and 5 mm in diameter. Often the sample was out of round and the center of the cylinder was of smaller diameter than the ends. These samples were often manually broken up, ground with mortar and pestle, and cold-pressed into a more suitable geometry for thermoelectric characterization using standard pressing techniques. X-ray diffraction spectra of the samples were collected between these steps to ensure this final processing was not modifying the bulk characteristics of the material.

2.2 X-ray Diffraction

X-ray diffraction methods were used to identify the phases present in the materials at various stages as synthesized above. Polycrystalline samples were characterized via powder diffraction techniques which provided a quick determination of the phases present and the homogeneity of the sample. Further analysis of appropriate powders, often with the addition of a silicon internal standard, revealed structure information as well as a measure of the filling fraction through the relative intensities of the 211 and 310 integrated peak intensities. The bulk of X-ray characterization was performed on a Scintag PAD V diffractometer, though a Siemens D500 and Phillips X'Pert system were also used for the improved data quality for X-ray refinements. All X-ray data were collected from Cu Kα radiation (λ = 1.5418 Å).

Powder diffraction provided a spectrum that could be analyzed to determine which phases were present as well as their relative population within the sample. It was this mode of analysis that made up the bulk of X-ray measurements; this served as quality control on the synthesis process and a source of alerts when difficulties appeared between the stages such as during initial synthesis or the high-pressure synthesis steps.

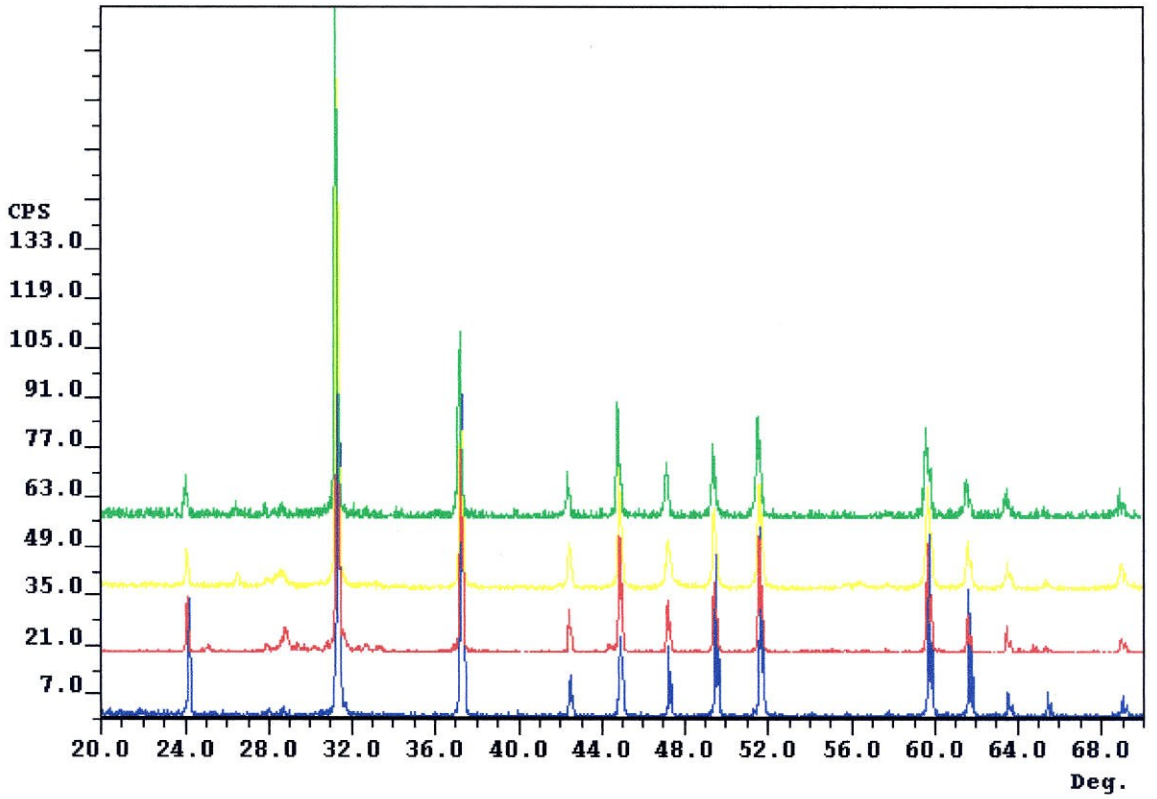

Figure 2.6: Typical filled skutterudite histograms, the 211 skutterudite peak is at 24 degrees 2Θ and the 310 main peak for skutterudite is at 31 degrees 2Θ.

Void filling in the skutterudite structure can be determined directly from the X-ray data through careful examination of the 211 and 310 reflections. As the void site is filled with rare earth atoms, the 211 peak is driven towards extinction. By comparing the unchanged intensity of the reflection at 310 (the primary reflection in skutterudite) with the reflection at 211, one can determine the filling fraction in the skutterudite sample [51]. The ratio of 211 to 310 peak intensity is known experimentally for $CoSb_3$ and can be calculated for $Ce_xCo_4Sb_{12}$ as shown in Figure 2.7. This technique depends on a homogenous powder sample, otherwise both filled and unfilled skutterudite compositions will contribute overlapping peaks to the pattern making determination through this technique unappealing. Samples submitted to this analysis were scanned over the 211

and 310 reflection peaks specifically to improve the counting statistics and the signal-to-noise ratio.

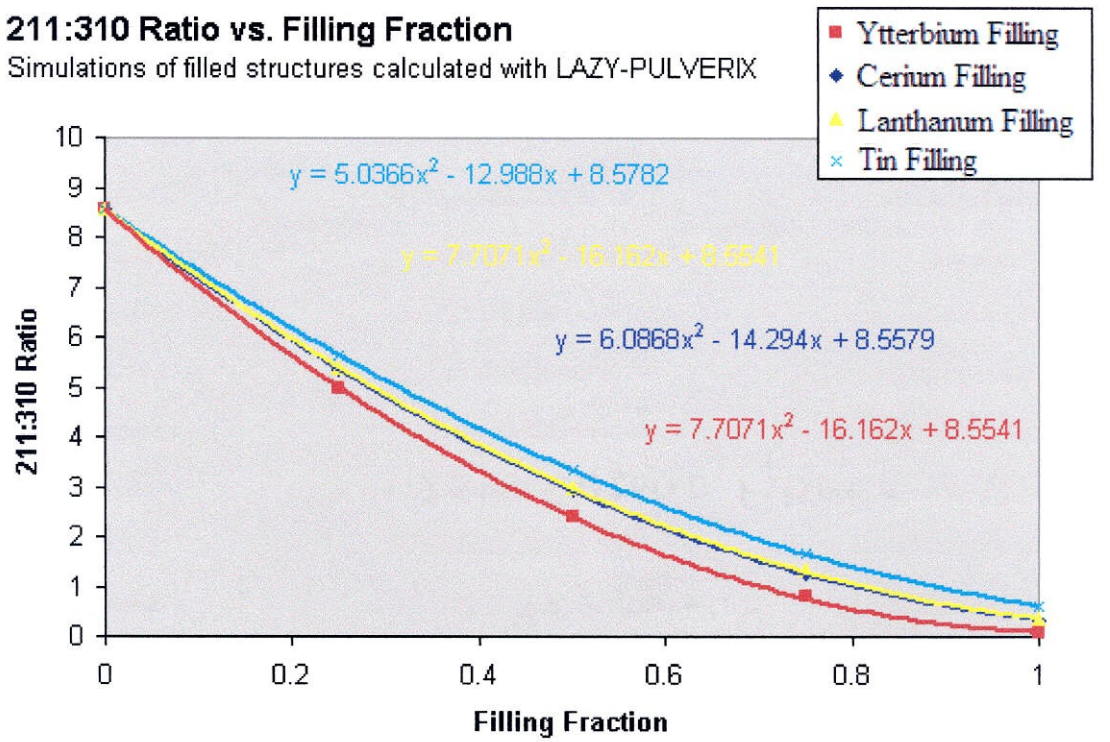

Figure 2.7: Calculated peak intensity ratio between the 211 and 310 peaks in filled skutterudite. Increasing the atomic number of the filling ion drives the 211 peak to extinction faster. LAZY-PULVERIX was used to simulate the peak intensities for the filled skutterudite compositions.

The compositions with cerium content above 0.1 in $CoSb_3$ and all of the ruthenium-rhodium skutterudites are new materials, so Rietveld refinements were performed on these samples. The Rietveld method is a whole-pattern, least-squares refinement. The least-squares refinements are carried out until the user is satisfied that a best fit has been found between the entire observed pattern and the entire calculated pattern. A silicon internal standard was combined with the skutterudite samples to improve the accuracy of the refinements. The program Rietica [53] was used in these refinements as well as the

X'Pert Plus [54] refinement package, both of which use the Reitveld analysis method [55].

2.3 Chemical Analysis

The composition of skutterudite compounds was measured using a JEOL JXA-733 electron microprobe. This microprobe can acquire digital secondary-electron and backscattered-electron images as well as digital x-ray maps. Chemical composition is characterized through the use of five wavelength-dispersive spectrometers and an energy-dispersive spectrometer. The probed volume in this electron microprobe is a few cubic microns, making this technique ideal for exploring compositional variation on a small length scale.

Pressed powder samples were mounted in epoxy resin, polished, and coated with carbon by evaporation. Skutterudite samples were mechanically soft and processed surfaces were easily polished to reveal the bulk material. Microprobe data were taken over multiple points on each sample for statistical averaging. On multiphase samples the impurity phases were often identified by backscattered electron contrast in scanning mode on the electron probe, followed by full Wavelength Dispersive Spectral (WDS) analysis of selected points on each of the impurity phases. Common impurities such as $CeSb_2$ and $CoSb_2$ had very narrow compositional ranges and were not of interest in and of themselves for our study, beyond their occurrence as a diagnostic to refine the synthesis process. Skutterudite matrix phases, on the other hand, were our primary interest and compositions were probed over tens of points to generate a statistical average of the composition. Pure elemental standards were used for all elements except cerium, for which a cerium phosphate standard was used. Measured x-ray peak intensities were converted to elemental atomic percentages using the CITZAF program [56]. Typical

analytical totals were above 98 % for well-prepared samples with operating conditions of 15 keV and 25 nA. Magnification of 40x was used for general imaging; elemental analyses were collected while rastering at 170kx, i.e. over a square <200 nm on a side. This sampled volume is effectively a point analysis, as it is smaller than the activated volume for the experimental probe.

2.4 Electrical and Thermal Characterization

2.4.1 Hall Mobility and Resistivity

Hall mobility and resistivity were measured over a range of temperatures from room temperature through 550 °C for many samples. The resistivity of the material is a factor in the dimensionless figure of merit for thermoelectric materials, while the information returned from the Hall measurement itself is a useful diagnostic for behavior of the material. The sign of the Hall Coefficient can serve as a confirmation of the sign of the Seebeck coefficient in determining the majority charge carrier in the material. The carrier concentration is also returned from the Hall measurement; this parameter is a useful indicator of the suitability of the material for a thermoelectric application. The carrier concentration and the mobility do not appear directly in the ZT formula, but both can serve as early warnings of poor thermoelectric performance.

Skutterudites suffer degradation, usually due to antimony sublimation, resulting in variation in resistivity values on heating and cooling above 550 °C; hence the Hall effect measurements were kept below this temperature. Samples were prepared for measurement by polishing the top and bottom surfaces smooth and parallel. High pressure samples were often of too small a radius for this technique and were typically ground to a powder and pressed under more conventional pressures to produce a suitable pellet. The configuration was that of a four probe technique using the van Der Pauw method [17, 18], which is advantageous because it allows the small sample of arbitrary shape (5-20 mm x 1 mm). This is achieved by measuring across the sample twice, with the V and I probes swapped, and taking the average for each data point generated.

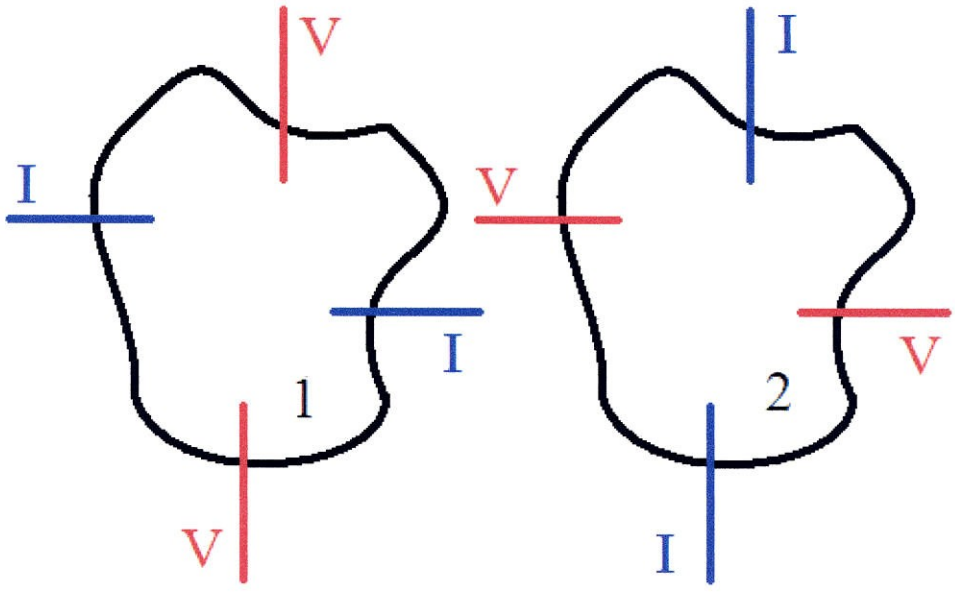

Figure 2.8: Schematic showing the Van der Pauw configuration for Hall effect measurement.

Four molybdenum contacts were applied evenly about the sample each held in place with a set screw. A thermocouple measured the experimental temperature on the sample stage. The entire stage, with sample firmly held in place with the four electrical leads, was inserted into a heater and electromagnet for Hall characterization. The chamber was then evacuated to 10^{-7} torr and testing conducted in alternating plus and minus 10,000 gauss (1 Tesla) fields. From this technique carrier type, Hall mobility, carrier concentration and resistivity could be determined.

2.4.2 Small ΔT Seebeck Coefficient

The Seebeck coefficient is the ratio of proportionality between the thermal gradient applied to a material and the resultant electrical gradient established in response to that thermal gradient. The Seebeck coefficient squared is proportional to the dimensionless

figure of merit, and describes the electrical potential of any device operating between two known heat reservoirs.

Samples were prepared for Seebeck characterization by polishing until a regular cylindrical sample with parallel ends was obtained. The Seebeck coefficient was measured in an apparatus that maintained good electrical and thermal contact with each end of the sample. The electrical potential was measured through the thermocouple leads ensuring the thermal and electrical measurements were taken over the same point on the sample. The bottom plate was made of copper and water cooled, maintaining a temperature of 15-16 °C. The top plate was a ceramic heater capable of generating a small thermal gradient, though this plate is typically 22 °C for room temperature Seebeck measurements. Temperatures are measured with four thermocouples, two for each side, to provide a greater measure of accuracy and reliability in the Seebeck value.

2.4.3 Large ΔT Seebeck Coefficient

In a similar manner, high temperature Seebeck measurements can be conducted over a gradient as temperature is varied over a wide range, or over a much larger thermal gradient. This apparatus is similar to the room temperature device but operates in an evacuated chamber to minimize thermal loss and noise. The electrical leads and thermocouples are separate as well but observation of the Seebeck Coefficient at temperatures of up to 1000 °C is possible.

2.4.4 Thermal Conductivity

Thermal conductivity was measured in a range from room temperature to just below decomposition, usually around 600 °C. The measurement was conducted with a flash diffusivity technique [60] where the time lag between an incident light flash on one side of a sample and a temperature increase measured on the dark side of the sample was observed. The light is conducted to the sample through a quartz light pipe which is masked on each end to prevent bleed-over into the detector. An analytic solution exists that relates the thermal diffusivity of the material to the rise time of temperature on one side of an infinite slab, given a step function in heat flux applied to the far side; if absorption properties of the surfaces are standardized by carbon coating, then the magnitude of the temperature rise allows determination of thermal conductivity as well.

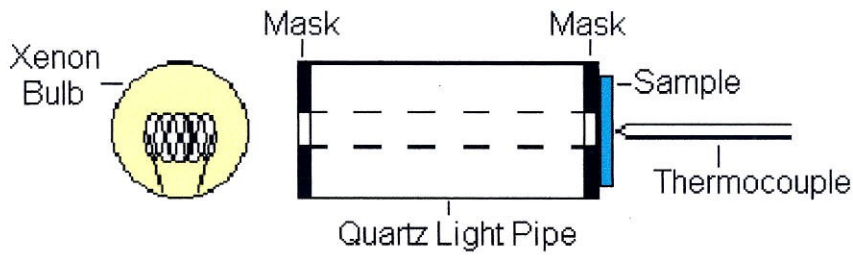

Figure 2.9: Schematic of the flash-diffusivity measurement. Incident light from a high intensity xenon bulb is conducted through a quartz light pipe towards the sample.

Such a configuration requires precise measurement of temperature and standardization of approach. Samples were prepared by cutting and polishing to ensure parallel surfaces and carbon coating those surfaces to normalize sample emissivity and reflectance. This aids the normalization of the experiment so the test can be calibrated. It was also important to mask the light pipe to prevent spillover of the xenon flash, which drowns out

the temperature change on the back side of the sample. The entire apparatus was contained in an evacuated chamber to minimize thermal loss and prevent oxidation of graphite components. Samples tested to temperatures above 550 °C showed signs of thermal damage, mainly antimony sublimation. Such damage manifests in the data as hysteresis in the thermal conductivity between heating and cooling curves.

Chapter 3

High-Pressure Synthesis of $Ce_xCo_4Sb_{12}$ Skutterudites

Abstract

Explorations of cerium filling in $CoSb_3$ were undertaken using high-pressure synthesis as the primary synthesis technique. The high-pressure techniques employed provided synthesis conditions up to 14 GPa and 1000 °C. Survey experiments provided a guide for successful synthesis of single phase filled skutterudites, at filling fractions far in excess of the limit observed by employing conventional synthesis techniques (50% cerium filling). Filling was confirmed using X-ray and SEM Microprobe analysis. While no trend in lattice constant was observed with increasing filling fraction, there was a clear trend in the Seebeck coefficient. Higher filling fractions resulted in a smaller magnitude in the Seebeck coefficient. The implication of the trend in transport properties was unclear, as at very high filling fractions, above 25%, the conduction was n-type by Seebeck coefficient and p-type by Hall mobility measurements. We conclude that some degree of charge compensation is occurring in these very high filling fraction compounds, which might otherwise be expected to have an overabundance of valence electrons and a n-type metallic behavior. The synthesis technique developed here has opened new ranges of void filling fractions. The pressure, temperature and time systematics revealed in successful $Ce_xCo_4Sb_{12}$ synthesis predict experimental results in a useful way that has already been applied to related systems.

3.1 Introduction

Skutterudite materials have recently seen renewed interest as candidate thermoelectric materials. This interest has been spurred by the observation that the skutterudite structure allows for selective reduction in thermal conductivity through incorporation of filling ions [22, 59]. A wide variety of skutterudites have been reported in the literature including more than 11 binary compositions, 26 ternary compositions, and several skutterudite related phases and doped varieties [37, 65, 66]. The phonon-glass electron-crystal [20] approach to optimizing thermoelectric performance has motivated efforts to fill the large voids in the skutterudite structure with a variety of heavy ions. Typically these atoms are lanthanoids, but results with alkaline earth elements or actinoids have also been reported [30]. These weakly bound cations incorporated into the structure are free to vibrate out of phase with the lattice and thereby scatter phonon modes in the material. This causes a significant reduction in thermal conductivity without necessarily having a large impact on the electrical properties of the host material.

The skutterudite structure is a cubic system consisting of a simple cubic array of transition metal atoms (Co, Rh, Ir) with square rings of pnictides (P, As, Sb) in six of the eight cubes making up a single unit cell. The orientation of the square rings is different in neighboring octants such that the voids in the remaining two octants are coordinated by 12 pnictide anions. The skutterudite space group is IM3 and in the unfilled end member there are two empty "cage" sites per unit cell [67]. Figure 3.1 illustrates the structure of

skutterudite with grey spheres identifying the locations of the voids and marking the sites of potential filling ion incorporation.

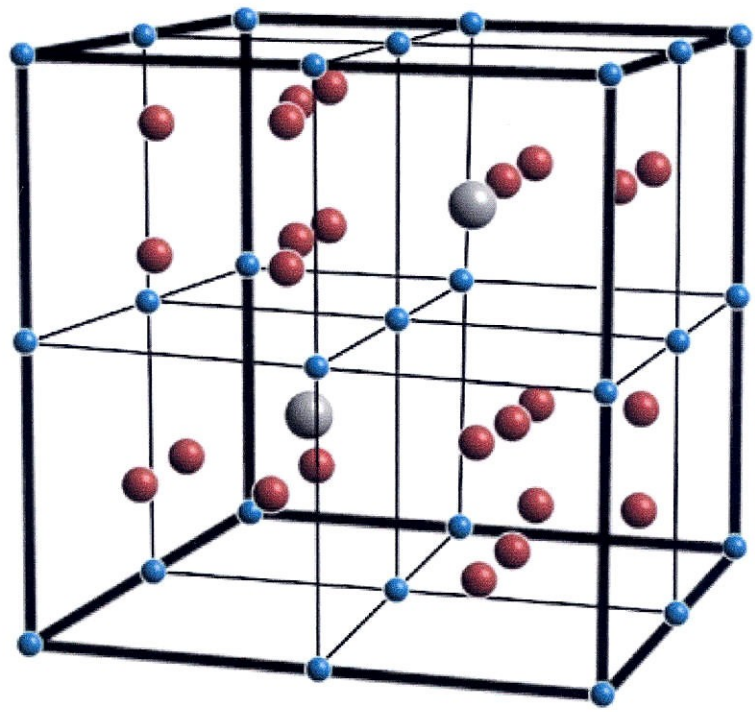

Figure 3.1: The skutterudite crystal structure is a cubic system in space group IM3. The transition metal cations form a simple cubic frame, eight of which make up the skutterudite unit cell (blue spheres). Three quarters of the octants have a square ring of anions (red spheres), while the last two octants are large voids in the structure (grey spheres used to emphasize void location).

It has been suggested that large atoms inserted into these cages will "rattle around" and reduce the thermal conductivity of the material by disrupting phonon modes in the crystal [68, 69]. This makes possible the separation of thermal and electrical conductivity, allowing one or the other to be specifically targeted for modification through compositional control of the material. Ideally a filling ion would be selected to simultaneously improve the electrical transport properties and suppress the thermal transport properties. The incentive for our efforts to lower thermal conductivity for candidate thermoelectric materials is improvement in the thermoelectric figure of merit.

The figure of merit is a factor in overall device efficiency and is inversely proportional to the thermal conductivity of the material

$$ZT = \frac{S^2 \sigma T}{\lambda}$$

where S is the Seebeck coefficient, σ the electrical conductivity, and λ the thermal conductivity of the candidate thermoelectric material. Void filling in skutterudite is characterized by large thermal parameters for filling ions and significantly reduced thermal conductivities for the filled compounds with respect to the unfilled [26, 43]. This selective depression of thermal conductivity is close to the ideal behavior of a phonon-glass electron-crystal hypothetical material. However, this approach requires careful consideration of the impact of filling on the electrical properties of the material, specifically the Seebeck coefficient, the electrical conductivity, the carrier concentration, and the sign of the charge-transporting species. It has been noted that the solubility limit of cerium filling ions in iron-cobalt skutterudites by conventional synthesis techniques is close to the p-type to n-type crossover point. If high pressure synthesis allows filling beyond the conventional limit then perhaps the extra conduction electrons donated by cerium cations would allow fabrication of n-type components from this normally p-type material. In this case an exception to the electrical-thermal decoupling approach might in fact prove useful in device fabrication.

Void filling in skutterudite systems is usually tied to the degree of solid solution on the transition metal site. Skutterudites containing pure cobalt or iridium, for example, are limited to 7% filling under normal synthesis conditions, while those with a solid solution

of iron and cobalt achieve full filling under the same synthesis conditions [43]. High-pressure techniques, however, allow synthesis of otherwise unreachable compositions [51, 46]. Of interest for our work is the potential to achieve high filling fractions without modifying the balance of the species occupation on the transition metal site. Given past success with hot pressing synthesis techniques [70, 34] and reported success of extraordinary filling via high-pressure synthesis in other skutterudite systems [71], it was decided to explore cerium filling in cobalt triantimonide to arbitrarily high filling fractions using high pressure synthesis techniques. The extraordinary synthesis conditions obtained in this work relied on techniques developed in experimental petrology [47]. The unusually high filling fractions obtained were of interest in exploring the effects of filling fraction on the properties without the entanglement of simultaneous substitutions on the host lattice.

These high filling fraction skutterudites were characterized through a variety of structural and electrical techniques. The phase identity and structural parameters were determined by X-ray diffraction (XRD) and rietveld refinement. Phase compositions were determined by electron microprobe. Thermoelectric properties were measured including Hall resistivity, Seebeck coefficient, and carrier concentration.

3.2 Selection of Filling Ion

Results reported below use cerium as the filling ion, but we began by investigating Sn-filled compositions in order to extend apparently promising published results on Sn-filled cobalt triantimonide [51]. Takizawa et al. [51] reported synthesis of triantimonide skutterudites at 0.03-5 GPa and 600 °C with tin exclusively filling the void site, based mostly on XRD analysis. We were unable to reproduce this result. First, we found that tin was clearly substituting on the antimony site in addition to filling the void site. Although tin and antimony, having similar atomic mass, are difficult to distinguish by XRD, our microprobe analysis showed in each case more tin in the composition than was estimated to occupy the void site based on integrated peak intensity ratios in the powder XRD pattern. In some cases microprobe analysis showed a tin to antimony ratio greater than 1:12 ratio, which is impossible if tin exclusively occupies the void site. Tin is known to substitute on the anion site in other skutterudites and related phases, e.g. $CoSn_{1.5}Te_{1.5}$ [65, 66]. We suggest that replacement of antimony by tin on the anion site compensates for sublimation of antimony during synthesis and leads to single-phase skutterudite product despite antimony loss. Placement of tin on the anion site rather than the void site offers a probable explanation for the increase in lattice constant with increasing tin content reported by Takizawa et al. [51]. Substitution of tin for antimony removes an electron from the delocalized bond across the anions, resulting in a weaker interaction overall. Expansion of the square pnictide rings in the octants of the skutterudite structure leads to a stronger interaction with the cation lattice than void filling. Indeed, the primary mechanism described for lattice expansion in the tin filled $CoSb_3$ skutterudite was reported to be elongation of the Sb-Sb bonds [71]. Other groups working on tin filled

skutterudites have since abandoned bulk high-pressure synthesis to concentrate on thin film techniques [74]. In place of the ambiguous dopant tin, we investigated cerium filling in $CoSb_3$. Cerium does not readily form anions and cerium is too large to occupy any site except the void. Prior work has shown that low cerium filling fraction compositions can be achieved with purely cobalt on the transition site and that any fraction up to complete filling can be achieve with suitable concomitant transition metal substitution [43, 44].

3.3 Experimental Details

Precursor powders of $Ce_xCo_4Sb_{12}$ with $0 < x < 0.5$ were prepared using methods previously described [72]. These powders were typically a mixture of $Ce_{0.07}Co_4Sb_{12}$ and $CeSb_2$. This precursor was then pressed at pressures up to 14 GPa, representing a two hundred-fold increase in pressure over typical hot pressing techniques [70]. This synthesis utilized a 1000 ton press and Walker type 6-8 multianvil apparatus [47, 48]. Pressure calibration in the device was performed by bracketing well-characterized phase boundaries in the temperature and pressure ranges of interest [49, 50]. The bulk of our materials synthesis was conducted with a porous MgO pressure medium that included built in pressure gaskets. The octahedron and gaskets were wrapped with Teflon tape and drilled through for the insertion of a graphite furnace. Molybdenum end caps were used to provide solid electrical contact between the furnace and the anvils providing the current. Figures 3.2 and 3.3 illustrate the assembly of a castable octahedral experiment. Temperature was monitored and controlled with a W5%Re - W26%Re axial thermocouple (Type C) loaded into the top of the furnace aperture and a power-feedback

system. Through control of the temperature, pressure, and time profile final materials with high filling fractions were obtained.

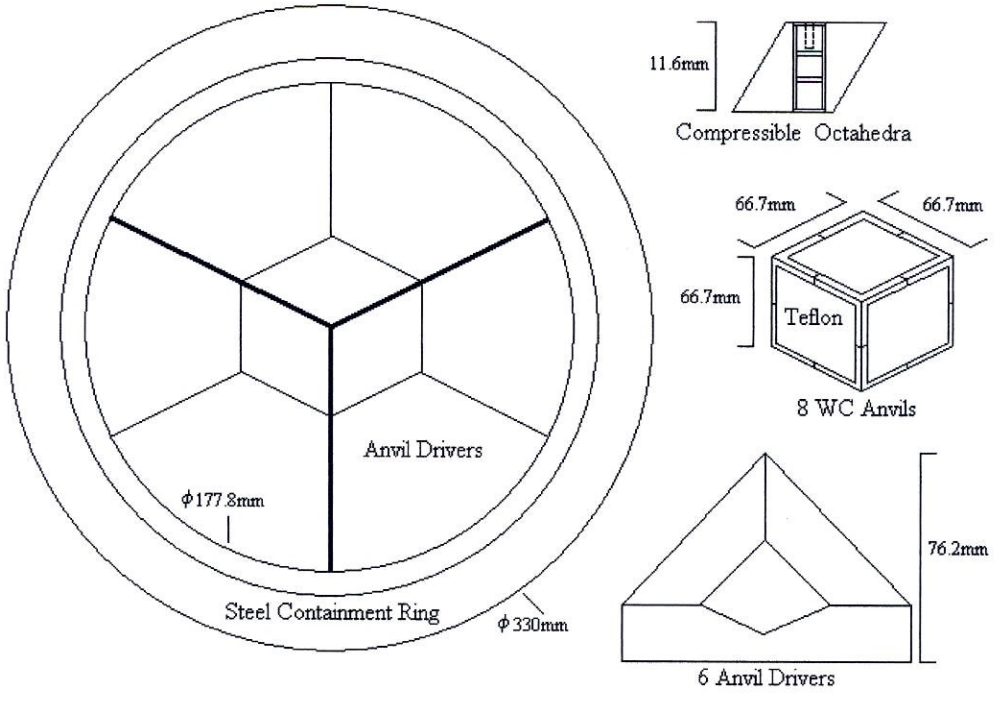

Figure 3.2: The primary components of a multi-anvil experiment in a Walker-type module. The sample is placed in the compressible octahedron, the compressible octahedron between the tungsten carbide anvils, the anvils between the hardened steel anvil drivers, and the anvil drivers within the steel containment ring on the press.

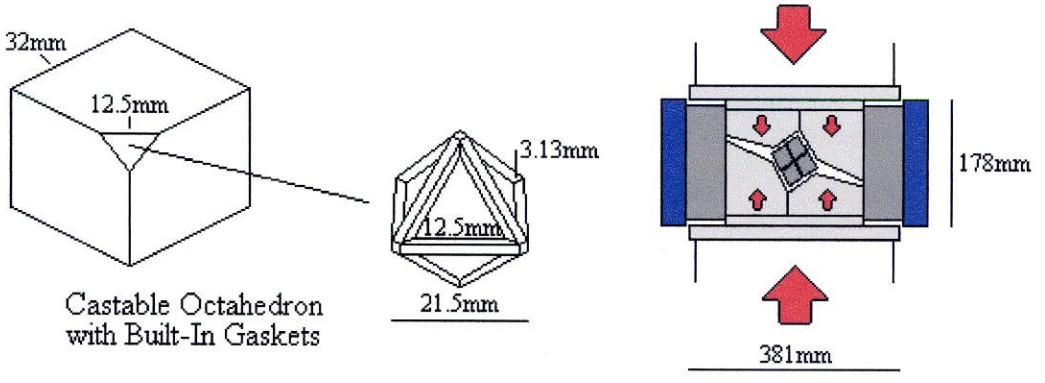

Figure 3.3: The compressible octahedron of castable octahedral assembly is formed with gaskets as part of the octahedron. The truncations on the eight tungsten carbide anvils fit into the octahedron between the gaskets, resulting in a cube of tungsten carbide surrounding the sample assembly. This is then loaded into the module where the six anvil drivers transmit the uniaxial load from the press to each of the eight anvils evenly.

Samples were characterized structurally by powder XRD. X-ray data were collected with Cu Kα radiation and a silicon internal standard. The Phillips X'Pert system was operated with a counting time of 1 sec per 0.02 degree in a θ-2θ configuration [54]. Compositional analysis was conducted on a JEOL 733 Superprobe with electron backscatter imaging and Energy Dispersive Spectroscopy (EDS) for quick phase identification and standardized wavelength dispersive spectroscopy (WDS) for quantitative analysis [56]. The microprobe data were sampled over 5-15 points per sample with a 10 μm rastered beam; analytical totals exceeded 98%. The thermoelectric properties were characterized through Seebeck coefficient, resistivity, and Hall effect measurements and thermal conductivity was measured via the flash diffusivity technique [60].

3.4 Results and Discussion

Related skutterudite systems show stability at ambient temperatures over a tremendous range of pressures. In $IrSb_3$, the skutterudite structure was observed from ambient pressure up through 42.5 GPa [41]. Such a wide range of pressure stability suggests great freedom in selecting hot pressing parameters to synthesize our desired high filling fraction material. Previous work by Takizawa et al. [51] reported that filled skutterudite synthesis was limited only by the 5 GPa limit on their pressure system and the 600 °C sublimation point of antimony at standard pressure. If antimony sublimation is the limiting factor, then increasing pressure ought to enable synthesis at increasing maximum temperatures. Our early results showed, however, that the addition of a filling ion provides an alternative decomposition routes to the high-density diantimonide structure

(the density of the diantimonide is about 10% greater than that of the triantimonide for cobalt and iridium antimonides, specifically 7.62 g/cm^3 for $CoSb_3$ and 8.34 g/cm^3 for $CoSb_2$ [73]). The process parameters of the sample in Figure 3.4 matched those reported for 40% tin-filled $CoSb_3$, 5 GPa and 550 ˚C. In this and similar experiments, the decomposition to unfilled skutterudite and diantimonide was favorable and rapid and led to compositional heterogeneity on a scale much larger than the starting particle size of 25 μm.

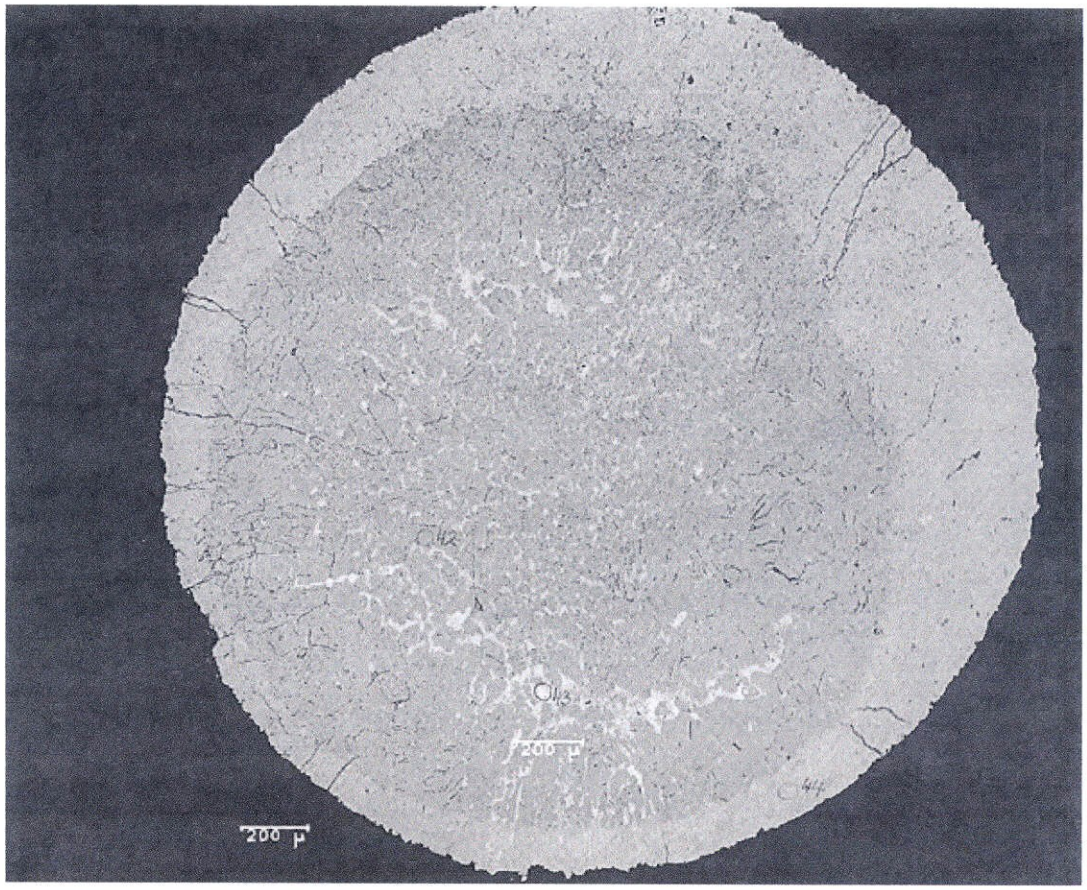

Figure 3.4: Micrograph showing the aftermath of a filled skutterudite synthesis attempt decomposing into $CeSb_2$ surrounded by a depletion layer of $CoSb_3$, in a low filling fraction matrix ($Ce_{0.05}Co_4Sb_{12}$).

A survey of the temperature and pressure range of our experimental setup, aided by a fortuitous heating failure, led to the discovery that the limit in temperature for

decomposition into diantimonides decreases with increasing synthesis pressure, consistent with the negative volume change of this reaction. Our first high filling fraction composition, $Ce_{0.15}Co_4Sb_{12}$, was obtained serendipitously at 14 GPa and 100 °C, whereas high temperature synthesis at 14 GPa repeatedly failed. Figure 3.5 shows the general trend in synthesis conditions for filled $Ce_{0.15}Co_4Sb_{12}$, with a 40 °C decrease in maximum temperature for every 1 GPa increase in pressure.

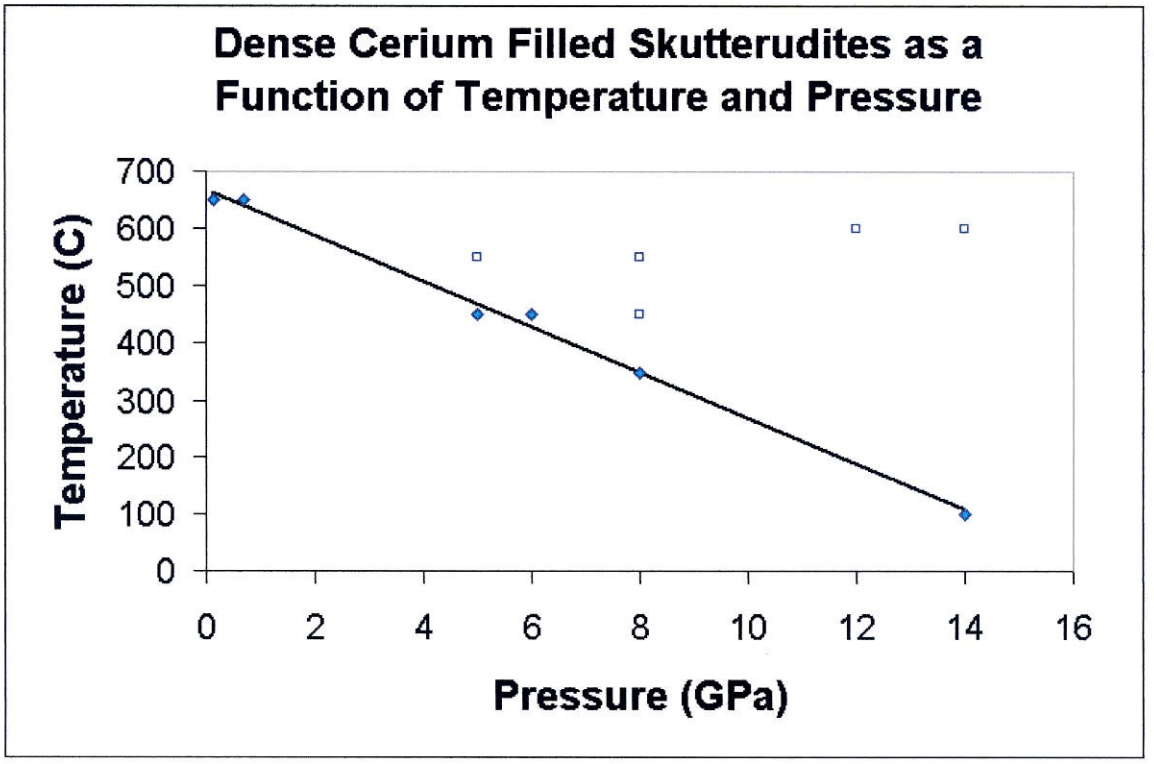

Figure 3.5: Results of survey experiments probing the P-T relationship in filled skutterudite synthesis. The time at temperature was constant in these experiments, at 30 minutes. Open symbols indicate experiments with decomposition to diantimonide; filled symbols indicate experiments with one-phase filled skutterudite products.

The 14 GPa, 100 °C experiments resulted in extremely small samples, less than 2 mm in maximum dimension and suffered from significant cracking; however, they were free of diantimonide contamination or segregation into high- and low-filling regions. Figure 3.6 shows a micrograph from a 14GPa experiment conducted at 100°C that resulted in a final

composition of $Ce_{0.15}Co_4Sb_{12}$. With these observations we refined our synthesis conditions and were able to reliably produce high filling fraction $Ce_xCo_4Sb_{12}$ materials with filling fraction $x \leq 0.5$. The samples characterized below were all synthesized in a two-stage heating protocol at 6 GPa: 30 minutes at 600 °C followed by 2 hours at 350 °C. In the larger version of the multi-anvil apparatus suitable for 6 GPa pressures, and with the smaller decompression stresses, we were able to recover samples large enough for thermoelectric, structural, and compositional measurements either as-recovered or after regrinding and ordinary cold-pressing to obtain a pellet.

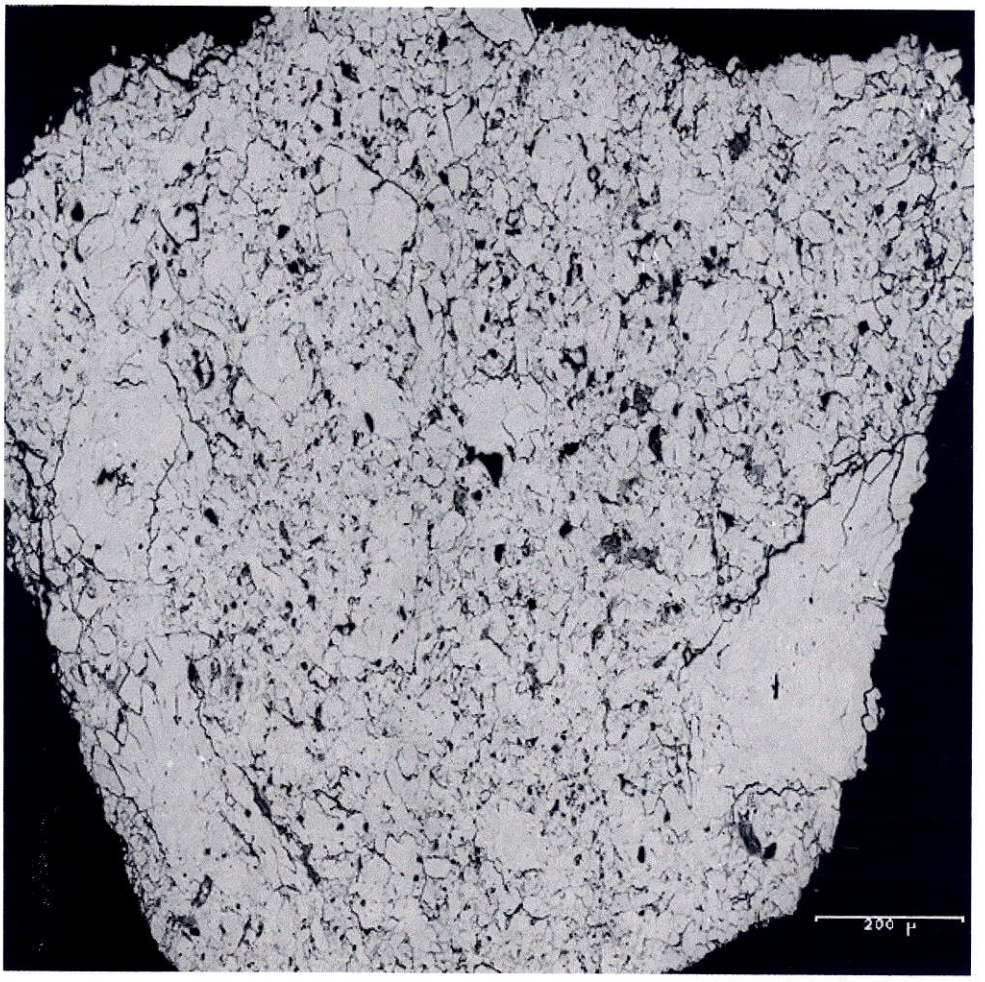

Figure 3.6: 15% Cerium filled cobalt triantimonide skutterudite produced via high pressure technique from a 15% nominal cerium content mixture of low filling fraction skutterudite and $CeSb_2$. Synthesis conditions of 14GPa, 100°C and 30 minutes were utilized to prevent formation of diantimonides prevalent in higher temperature synthesis.

3.5 Structure

Structural analysis of our $Ce_xCo_4Sb_{12}$ materials was conducted with powder XRD, supported by microprobe analysis to determine composition and ensure single-phase samples. Figure 3.7 shows a typical powder XRD spectrum from our high filling fraction, high-pressure run products. Note the very weak 211 reflection, characteristic of filling fractions near 50%. Reitveld refinements on our x-ray data produced a lattice constant largely independent of filling fraction (Table 3.1 and Figure 3.8); there is only a small lattice expansion in the first 10% filling. This stands in contrast to monotonically increasing lattice constants reported by Takizawa for $Sn_xCo_4Sb_{12}$. We argue that lattice expansion in the tin bearing system is due to substitution of tin on the antimony site, rather than to any effect of filling the void site. Cerium does not substitute on antimony sites, and we find that cerium filling does not cause lattice expansion. Even the relatively large cerium atom has a diameter of only 1.40 Å, while the void in skutterudite is 1.89 Å in diameter, and can readily accommodate cerium filling without lattice expansion.

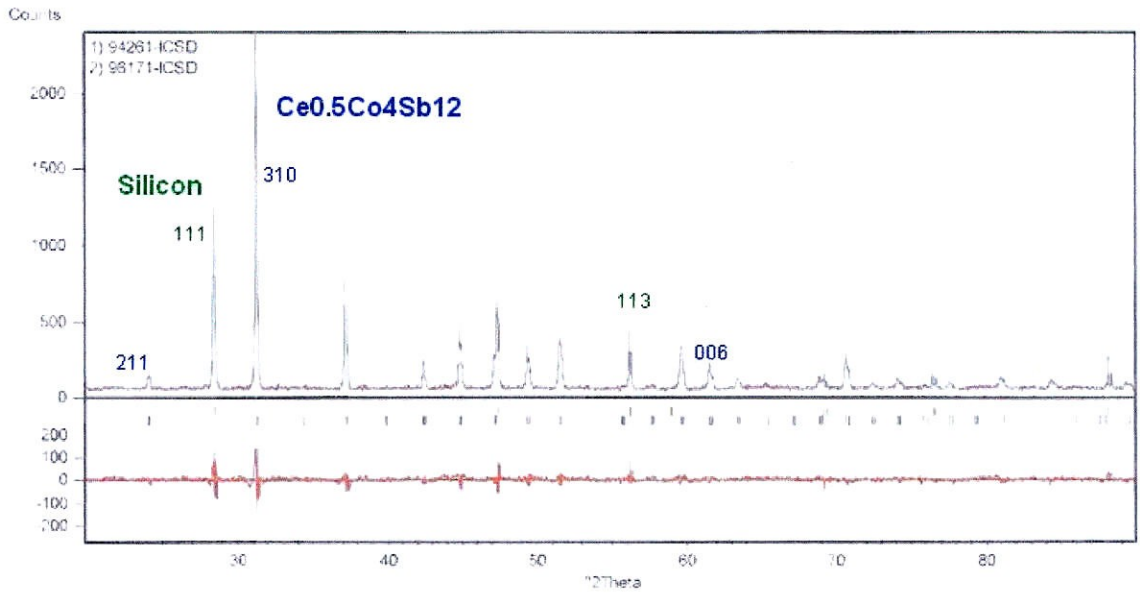

Figure 3.7: Typical histogram of x-ray data, in this case for $Ce_{0.5}Co_4Sb_{12}$.

Composition of the Skutterudite Phase	Lattice Constant (This Work)	R_{xp}	R_p	R_{wp}	GOF
CoSb3	9.035	11.07	10.85	13.62	1.515
Ce0.15Co4Sb12	9.0448	11.795	10.93	16.16	1.877
Ce0.25Co4Sb12	9.0445	11.363	16.18	23.87	4.414
Ce0.5Co4Sb12	9.0438	10.966	9.793	12.61	1.323

Table 3.1: Lattice refinement details for $Ce_xCo_4Sb_{12}$ where x = 0, 0.15, 0.25, 0.5. Samples were characterized with Copper k_α radiation with a silicon internal standard.

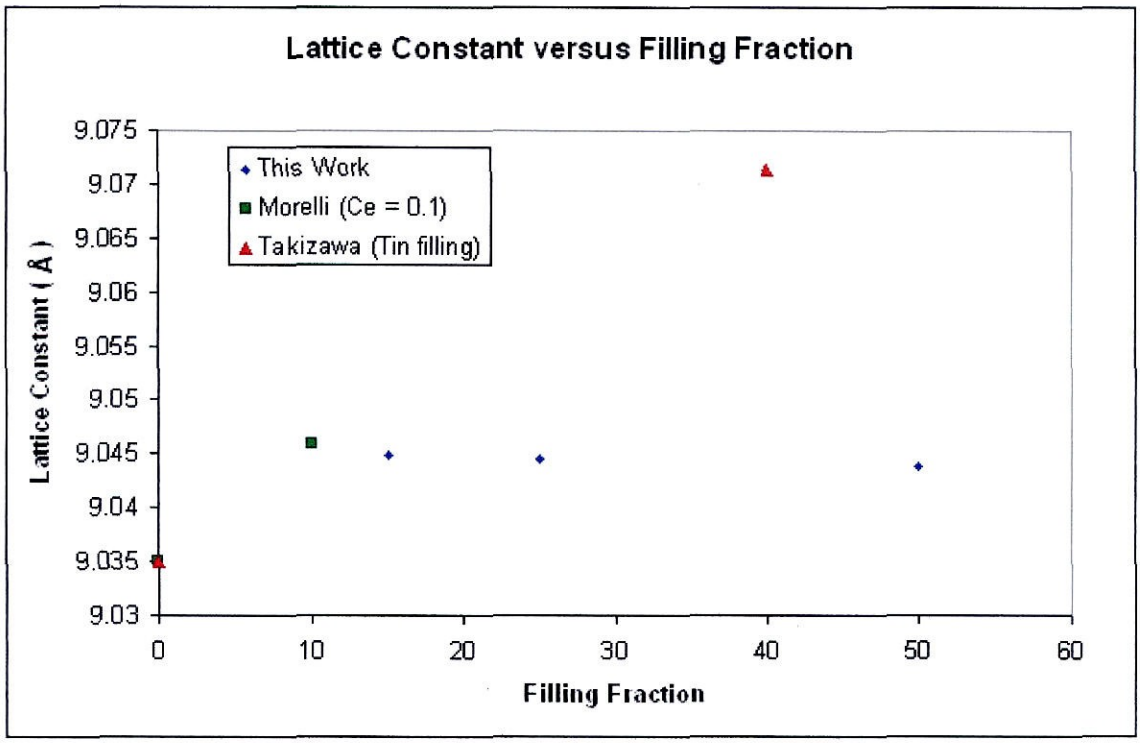

Figure 3.8: The lattice constant of the cubic unit cell as a function of filling fraction x for $Ce_xCo_4Sb_{12}$. The lattice constant increases up to the neighborhood of 10% filling and then is insensitive to further increases in cerium content. For reference are data reported by Takizawa for the $Sn_xCo_4Sb_{12}$ and Morelli for the $Ce_xCo_4Sb_{12}$ systems [51, 43].

3.6 Thermoelectric Characterization

The electrical property data are presented in Figure 3.9 and Table 3.2. We expected that addition of each atom of cerium to $CoSb_3$ per formula unit would contribute three additional electrons to the conduction band. Such an addition would correspond to additional electrons on the order of 10^{21} per cubic centimeter and lead to n-type metallic behavior. In general we found the opposite behavior. The carrier mobility and conductivity dropped while the carrier concentration increased modestly. This would seem to indicate incomplete ionization of the filling ion, contributing fewer conduction electrons than expected. The result is a decrease in the magnitude of the Seebeck

coefficient with increasing filling, and a transition to mixed type conduction near 20% filling.

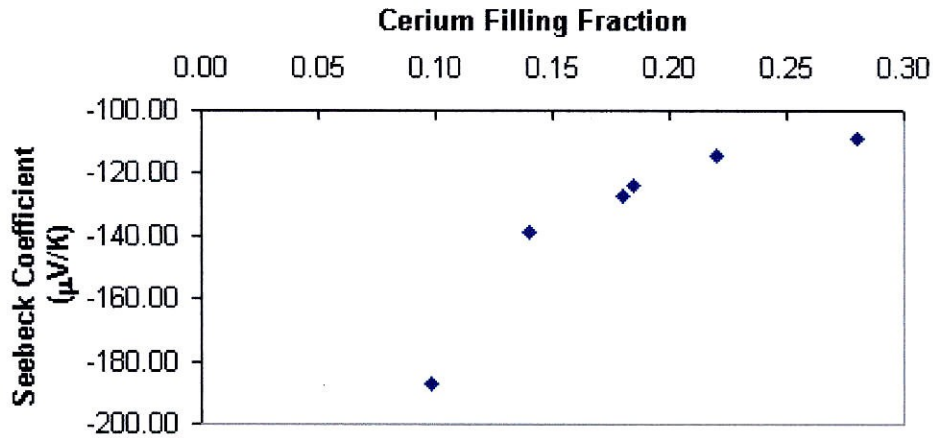

Figure 3.9: Seebeck coefficient as a function of cerium filling for $Ce_xCo_4Sb_{12}$. Samples with higher cerium filling fractions have a smaller magnitude Seebeck coefficient, and despite increased cerium content the behavior is less n-type at higher filling fractions.

Composition of the Skutterudite Phase	Carrier Concentration (cm^{-3})	Resistivity (mΩcm)	Mobility ($cm^2V^{-1}s^{-1}$)	Seebeck ($\mu V\ K^{-1}$)	Secondary Phases
$Ce_{0.098}Co_4Sb_{11.9}$	-6.10E+19	2.38	-43.00	-187	$CeSb_2$
$Ce_{0.14}Co_4Sb_{12}$	-2.17E+19	16.25	-17.74	-139	$CeSb_2$ + $CoSb_2$
$Ce_{0.18}Co_4Sb_{12.2}$	-2.13E+20	5.22	-5.61	-127	$CeSb_2$ + $CoSb_2$
$Ce_{0.185}Co_4Sb_{12.52}$	-3.31E+20	7.56	-2.50	-124	$CeSb_2$
$Ce_{0.22}Co_4Sb_{12.02}$	2.86E+20	1.31	1.81	-114	$CeSb_2$ + $CoSb_2$
$Ce_{0.28}Co_4Sb_{12}$	5.16E+19	58.85	2.06	-109	$CeSb_2$ + $CoSb_2$

Table 3.2: Carrier concentration, resistivity, mobility and Seebeck coefficient of $Ce_xCo_4Sb_{12}$. Sample composition is from Microprobe EDS analysis over 5-15 point samples.

The power factor for our high filling fraction skutterudites was quite poor. Two orders of magnitude separated $Ce_{0.3}Co_4Sb_{12}$ from the binary $CoSb_3$ compound. The trends in carrier concentration and appearance of a mixed conduction type, reflected in the sign disagreement between Seebeck and carrier concentration, seems to indicate significant charge compensation across the cations in the lattice.

3.7 Conclusions

High-pressure, low-temperature synthesis techniques were developed to create samples of cerium filled cobalt triantimonide skutterudite ($Ce_xCo_4Sb_{12}$) with observed cerium contents up to x = 0.5. The compositions, X-ray refinements, and electrical properties all require that cerium is entering the structure exclusively through filling of the void sites, up to one per unit cell. This represents 50% cerium filling, a significant improvement over the limit of 7% available to standard techniques. However, the lattice constant of these high filling fraction skutterudites did not continue to increase beyond that seen at much lower filling fractions. The electrical properties resulting from this filling were disappointing and result in low ZT values and so the particular compositions so far synthesized are poor candidate thermoelectric materials. Insertion of excess cerium does not drive the material towards n-type conduction; instead it appears that some degree of charge compensation is active across the structure and the cerium ions do not achieve their nominal valence of 3^+. We conclude that further optimization of electrical properties through doping on the metal or semimetal site will be required to make a useful thermoelectric material in this system.

The high-pressure technique outlined here has opened new ranges of void filling fraction, allowing future work in exotic compositions previously outside the range of available hot-pressing techniques. The pressure, temperature and time systematics revealed in the successful Ce_xCoSb_3 triantimonde syntheses predict experimental results in a useful way and should generalize to related systems. These results have already been applied in the synthesis of filled iridium skutterudites and filled rhodium-ruthenium skutterudites [52].

Chapter 4
Synthesis and Thermoelectric Properties of $Ce(Ru_{0.67}Rh_{0.33})_4Sb_{12}$

Geoff D. Staneff[1], Paul D. Asimow[2], Thierry Caillat[3]
[1]Department of Materials Science, California Institute of Technology
Pasadena, CA 91125
[2] Division of Geological and Planetary Sciences, California Institute of Technology
Pasadena, CA 91125
[3]Jet Propulsion Laboratory
Pasadena, CA 91109

Abstract

Exotic filled skutterudite compositions show promise for thermoelectric applications. Current work was undertaken with a nominal composition of $Ce(Ru_{0.67}Rh_{0.33})_4Sb_{12}$ to experimentally verify its potential as an n-type thermoelectric material. Nominal electroneutrality was expected at 0.89 cerium filling and fully filled materials were expected to be strongly n-type. Filled precursors of the nominal composition were synthesized using straightforward solid state reaction techniques, but standard synthesis routes failed to produce a fully-filled homogenous phase. Instead, the filled thermoelectric $Ce(Ru_{0.67}Rh_{0.33})_4Sb_{12}$ was synthesized using a combination of solid state reaction of elemental constituents and high pressure hot pressing. A range of pressure-temperature conditions was explored; the upper temperature limit of filled skutterudite in this system decreases with increasing pressure and disappears by 12 GPa. The optimal synthesis was performed in multi-anvil devices at 4-6 GPa pressure and dwell temperatures of 350-700 °C. The result of this work, a $Ce(Ru_{0.67}Rh_{0.33})_4Sb_{12}$ fully filled skutterudite material, exhibited unexpected p-type conductivity and an electrical resistance of 1.755 mΩ–cm that increased with temperature. Thermal conductivity,

Seebeck coefficient, and resistivity were measured on single phase samples. In this paper, we report the details of the synthesis route and measured thermoelectric properties, speculate on the deviation from expected carrier charge balance, and discuss implications for other filled skutterudite systems.

4.1 Introduction

In nature, skutterudite is a mineral of composition $(Co,Ni)As_{3-x}$. Its structure has a number of peculiar electrical and thermal properties that suggest an excellent potential for use in thermoelectric devices. This combination springs from the relatively complicated structure of the simple binary $CoAs_3$ compound. The skutterudite unit cell is comprised of thirtytwo atoms arranged in a cubic array of corner shared octahedra. These octahedra contain a central cobalt atom surrounded by six shared arsenic atoms. The misalignment of this array creates large void sites between the octahedra and in practice there is significant freedom for chemical substitution on all three of these crystallographic sites. Many transition metals can occupy the cobalt site, either as sole occupants or in solid solution with other transition metals even of disparate valence states. Likewise, the pnictides (P, As, Sb, Bi) can all form skutterudites. The As site can also be doped either p-type with the removal of electrons with a $Ge_{Sb}^{'}$ substitution or n-type with the addition of electrons with a $Te_{Sb}^{'}$ substitution. Into this significant compositional space one may also introduce substitutions onto the void sites without disrupting the skutterudite structure. Many workers have introduced rare earth metals into this void in the hopes of reducing the thermal conductivity.

The compositional freedom afforded by the structure coupled with the natural electrical properties of binary skutterudites nominated the system for further study with the goal of improved thermoelectric efficiency. The thermoelectric efficiency of different materials can be judged through a comparison of the dimensionless figure of merit, *ZT*

$$ZT = \frac{\sigma S^2 T}{\lambda}$$

Where σ is electrical conductivity, *S* is the Seebeck coefficient, *T* is the temperature, and λ is the thermal conductivity. Maximizing the electrical conductivity and Seebeck coefficient while minimizing the thermal conductivity leads to high *ZT* values and useful thermoelectric behavior. High-performance thermoelectric materials typically have *ZT* values on the order of 1-1.5. While the binary skutterudite has reasonably high electrical properties σ and *S*, the thermal conductivity is unreasonably high for thermoelectric applications. However, the addition of a void-filling atom, a solid solution on the transition metal or pnictide sites, or any combination of these three substitutions can greatly reduce the thermal conductivity of the skutterudite [75]. Such potential sets skutterudite materials up to serve as excellent thermoelectric materials, if the right combination of thermal and electrical properties can be found in a given skutterudite composition.

Previous work by Fonari and Singh identified the rare-earth filled rhodium-ruthenium skutterudite system as a candidate for thermoelectric device applications on the basis of theoretical calculations [76]. Predictions of low thermal conductivity and a band structure favorable to electrical conduction made this system an appealing direction for further research. The compositions suggested, however, were beyond the reach of

standard synthesis techniques. To that end, building upon the initial work of Takizawa [51], a high-pressure synthesis route was developed to yield a single phase, fully filled, quaternary skutterudite composition. Here we present some of the properties of this cerium filled rhodium-ruthenium skutterudite.

4.2 Experimental Details

Samples were prepared using a multistage synthesis process. Initial synthesis combined cerium chunk with rhodium and ruthenium powders, which were melted in an induction furnace at 1400 °C. The resulting alloy was combined with antimony shot, placed in a boron nitride crucible and sealed in an evacuated quartz ampoule. The precursors were then held at 650 °C for 48 hours and quenched to room temperature. This product was ground to a particle size no greater than 25 microns.

The next synthesis stage involved a high-pressure, relatively low-temperature, synthesis process. High-pressure synthesis experiments were conducted on a Rockland Research Instruments 1000 ton press. This press is capable of reaching experimental conditions of 2500 °C and 25 GPa, although the sample size decreases with increasing pressure. Experiments were conducted in two internal geometries. Exploratory experiments at 6 GPa and above used an octahedral geometry with an MgO-based solid pressure medium. The successful synthesis and results reported here used a cubic geometry module with a

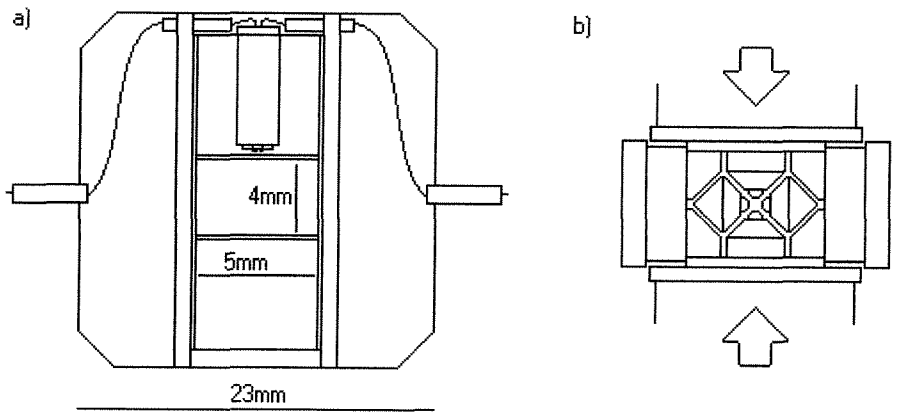

Figure 4.1. a) Schematic of pressure medium and sample assembly typical of cubic multi-anvil experiments. **b)** Diagram of press action converting uniaxial load into isostatic pressure.

21 mm soft-fired pyrophyllite cube as pressure medium. A 12.7 mm hole is drilled through the cube and a $BaCO_3$ sleeve inserted as thermal insulation. Inside this, a 7.7 mm outer diameter, 5 mm inner diameter graphite tube makes up the heating element. The sample is sandwiched in the central 4 mm region of the hotspot between graphite disks. Temperature was controlled using an axially mounted type C W/Re thermocouple. Remaining space inside the heater is filled with crushable MgO spacers (Figure 4.1a). The entire assembly is compressed by six tungsten carbide anvils driven together along the cubic axes by a set of steel guide blocks within a steel containment ring. Deformation of the pressure medium creates a quasihydrostatic load within the sample (Figure 4.1b). Pressure is calibrated as a function of hydraulic load on the press using phase transitions of bismuth at room temperature and, at elevated temperature, the quartz-coesite transition in SiO_2 (3.1 GPa) and the alpha-gamma transition in Fe_2SiO_4 (5 GPa).

Initial survey experiments were conducted over a range of pressure and temperature to find the stability limits of filled skutterudites. Mapping in the cerium-filled cobalt

triantimonide system showed, contrary to expectations, that the upper temperature limit above which only diantimonides were found decreases with increasing pressure (Figure 4.2). This survey suggested that synthesis conditions of 6 GPa and 600 °C for 24 hours, within the practical range of the largest volume configuration of the octahedral multianvil device, would provide successful syntheses of large enough samples for full characterization of thermoelectric properties. However, with these parameters the initial target composition of $Ce(Ru_{.75}Rh_{.25})_4Sb_{12}$ was not achieved. Typically a wide variety of diantimonides were mixed in with a filled skutterudite with a composition $Ce_{0.8}(Ru_{0.67}Rh_{0.33})_4Sb_{12}$. This composition had been observed in previous synthesis attempts using standard hot pressing techniques (0.1 GPa, 600 °C). Adjusting the nominal composition to reflect this preferred ratio of ruthenium to rhodium and a fortuitous failure in the pressure control system resulted in a single phase $Ce(Ru_{0.67}Rh_{0.33})_4Sb_{12}$ sample. With our understanding of the *P-T* relations in these filled skutterudites, the synthesis parameters were adjusted to a pressure of 6 GPa and a

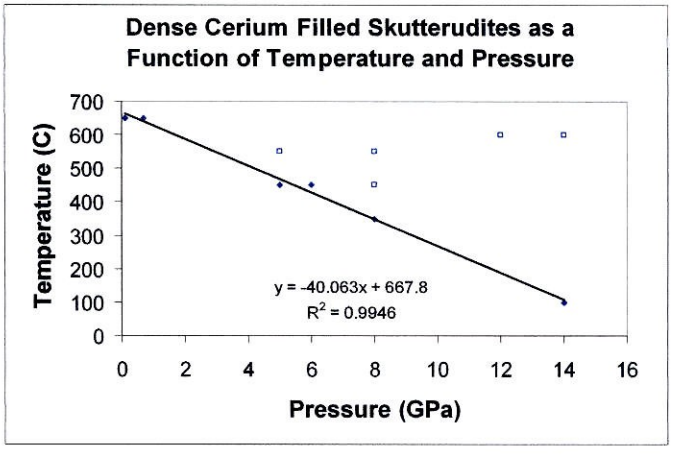

Figure 4.2. Single phase cerium-filled skutterudite synthesis success (closed diamonds) and failure (open squares) as a function of temperature and pressure. These data show a decreasing synthesis temperature limit with increasing synthesis pressure in $CeCo_4Sb_{12}$, which proved useful in setting the synthesis conditions for $Ce(Ru_{0.67}Rh_{0.33})_4Sb_{12}$.

temperature profile of 600 °C for 4 hours and 350 °C for 24 hours. Subsequently, conditions were successfully adjusted down to 5 GPa and 4 GPa, allowing the use of the still larger sample volumes of the cubic geometry shown in Figure 4.1. A pressure of 4 GPa and temperature profile of 700 °C for 4 hours followed by 450 °C for 24 hours represents the current synthesis parameters.

Once the high-pressure synthesis was completed the skutterudite compositions proved stable to moderately high temperature at standard pressure. The recovered materials were then processed for the last time, grinding them to powder and sintering using standard hot pressing techniques to reconfigure the shape and porosity of the sample to facilitate thermoelectric characterization. Powder x-ray diffraction and electron microprobe analysis before and after this step confirmed the phase stability of the material through this stage. Electrical properties were characterized with Seebeck coefficient, resistivity, and thermal conductivity measurements using techniques previously reported [33].

4.3 Discussion

Thermal conductivity as a function of temperature is shown in Figure 4.3. Thermal conductivity of $Ce(Ru_{0.67}Rh_{0.33})_4Sb_{12}$ was half that of the binary skutterudite $CoSb_3$. The thermal conductivity is low and stable over a wide range in temperature, with no temperature dependence from 175 to 625°C. However, antimony sublimation was observed above 550°C. This breakdown was severe enough to revert the triantimonide to a wide variety of diantimonides. Once reverted samples were of no further use so great

care was exercised to ensure the samples never experienced temperatures above the projected stability limit.

Electrical resistivity and Seebeck coefficient are shown in Figure 4.4. Again the samples showed signs of sublimation when held at temperatures exceeding 550 °C for extended periods of time. The filled rhodium-ruthenium skutterudite showed an electrical

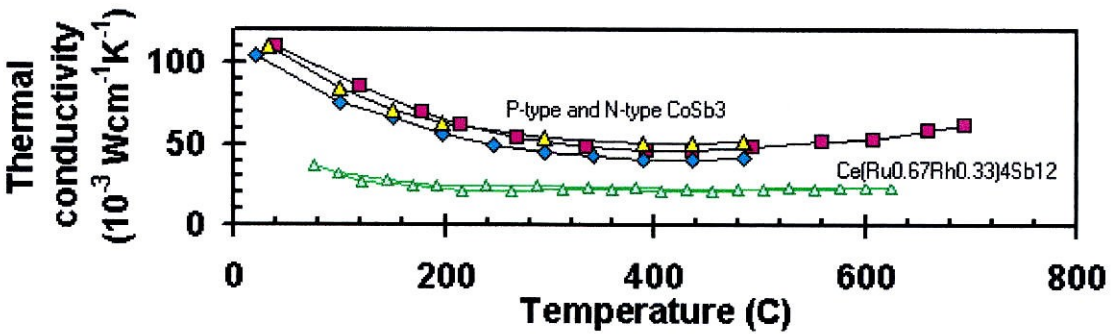

Figure 4.3. Thermal conductivity as a function of temperature from room temperature to 625 °C showing a much lower value for $Ce(Ru_{0.67}Rh_{0.33})_4Sb_{12}$ than for the typical binary skutterudite $CoSb_3$.

resistance of 1.755 mΩ–cm that increased with temperature. The Seebeck coefficient over the same range was p-type and increasing with temperature. Although the low thermal conductivity confirmed expectations, the electrical properties are surprising for the fully filled $Ce(Ru_{0.67}Rh_{0.33})_4Sb_{12}$ composition. Strong n-type conductivity was expected. from the heavy n-type doping implied by the stoichiometry of the material; the electrical breakpoint was expected at a cerium content of 0.89 while this work achieved a cerium content of 1.00, confirmed by microprobe analysis. The substitutions in this system were as follows:

$$Ce_V''' + 2\ ⅔Ru_{Rh}^{\bullet} + 1\ ⅓Rh_{Rh} + 12\ Sb_{Sb} = ⅓\ e^-$$ (3 sites v=void, rh=rhodium, sb=antimony)

The Ce filling fraction 0.89, this excess of one-third of an electron per unit cell indicates an addition of 2.27 x 10^{21} electrons per cm^3 relative to the binary skutterudite. At Ce filling fraction of 1.00, the addition of 2.68 x 10^{21} electrons per cm^3 should be sufficient to yield unambiguous n-type behavior. The p-type behavior of the fully cerium filled rhodium-ruthenium skutterudite is thus a strong indicator of charge compensation across the transition metal site. The significant number of missing conduction band electrons is

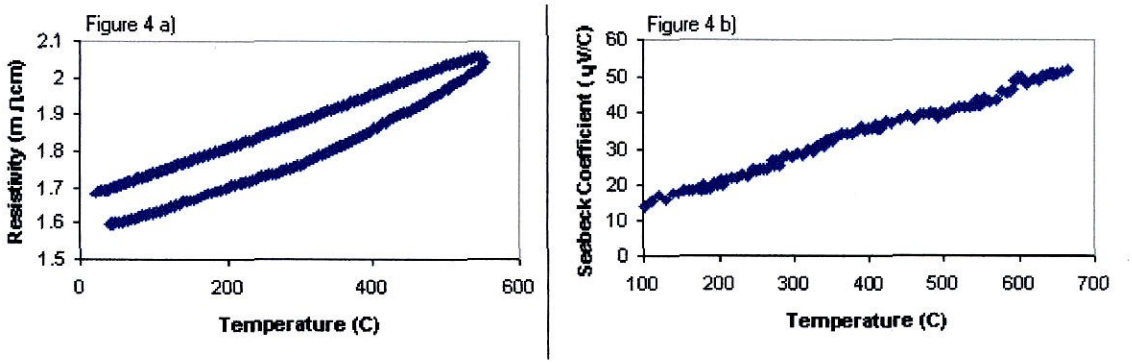

Figure 4.4. a) Resistivity as a function of temperature from room temperature to 625 °C showing an electrical resistance of 1.755 mΩ–cm that increased with temperature. Note hysteresis between heating and cooling cycles due to partial decomposition above 550 °C. **b)** Seebeck coefficient as a function of temperature from room temperature to 625 °C showing increasing p-type behavior with increasing temperature.

likely related to strong electron localization, which hinders the thermoelectric efficiency of this material.

As noted previously in our work with high cerium filling in cobalt triantimonide [46], the filling ion does not have the expected impact on electrical properties while it does have the expected impact on the thermal properties. Future work will require electrical doping on the transition metal or pnictide site in the skutterudite structure.

4.4 Conclusions

We have prepared samples of a cerium-filled rhodium-ruthenium skutterudite material in pursuit of excellent figure of thermoelectric merit *ZT* due to low thermal conductivity, large n-type Seebeck coefficient and high electrical conductivity. The resulting thermal properties were a significant improvement over binary skutterudites, showing that the combination of cerium filling and doping on the transition metal site is a powerful method of reducing the thermal conductivity in skutterudite materials. However, the resulting electrical properties were unexpected: the observed p-type conduction runs contrary to simple electron counting and indicates a charge compensation mechanism at work. Doping of this system could push the electrical properties back into a range useful for thermoelectric applications; work in this direction is presently underway. The high-pressure synthesis techniques developed working with the cerium-filled rhodium-ruthenium triantinomide and cerium-filled cobalt triantinomide skutterudite systems will facilitate further exploration of alternate skutterudite compositions and we expect to synthesize new skutterudite compositions with further doping on the transition metal, pnictide, or the large void site. The interest in systems with four or more components is driven by the difficulty in arriving at both low thermal conductivity and high electrical conductivity in the same material.

Acknowledgements

This work was made possible through the assistance and guidance of the Thermoelectrics group at the Jet Propulsion Laboratory.

Chapter 5

Nano-Structured Silicon Germanium

Abstract

In the course of our previous advanced thermoelectric materials research, high-pressure techniques were utilized to synthesize new skutterudite compositions that were beyond the reach of standard techniques. Here we exploit the large stresses that are initially present in high-pressure assemblies in order to manufacture composite materials with enhanced thermoelectric properties. The very large stresses allow control over the sintering mechanism, resulting in preservation of nanometer-scale grain structure of the material. The silicon and germanium compositions explored have been in used in thermoelectric generation for over fifty years, but control on a nanostructure scale has been limited to thin films [18] or membranes [77], neither of which are suited to the high temperature and current demands of large-scale thermoelectric power generation. The main objective for this work was to start with nanoparticles of silicon and germanium and produce a fully dense monolithic solid with initial grain size and chemical heterogeneity intact. Previous attempts using standard hot-pressing techniques have resulted in significant grain growth and chemical homogenization. Guided by a simple Nabarro-Herring creep model, we achieved densification without excessive grain growth or chemical homogenization through the application of compaction stresses of a few GPa.

5.1 Introduction

Silicon-germanium thermoelectrics have a long history of successful device applications, including the 1977 Voyager I and II spacecraft. Due to the high melting point and great temperature stability of silicon-germanium compounds, devices are able to operate at much higher temperatures in thermoelectric generators than many newer advanced thermoelectric materials. This allows the less efficient silicon-germanium systems to produce as much or more power than some cutting edge thermoelectric materials. A common thought in thermoelectric device research is to build a compound device combining the best materials for a given temperature range into one multi-component unicouple [35]. Such devices, however, have not performed up to expectation due in part to the innate mismatch between the silicon-germanium system and cutting edge moderate temperature thermoelectric systems [78]. Such compound devices often perform worse than the sum of their parts, or provide minimal improvement in efficiency for greatly increased complexity. The work on compatibility factors suggests that improvements in silicon-germanium thermoelectric devices will come as a result of improvement in silicon-germanium like materials.

One such route to improving the silicon-germanium system is control of the structure. A two phase system with small grain size could be useful in disrupting thermal conductivity and improving the thermoelectric figure of merit [79]. However, standard techniques in use at the Jet Propulsion Laboratory (JPL) have thus-far proved fruitless in achieving the desired two phase nano-structure in a sintered solid. Diffusion between silicon and

germanium proved too fast relative to sintering rates, and grain growth is a common densification route. In some aggregates, standard sintering methods yield a total lack of densification as nano-particle inclusions pin grain boundaries and prevent consolidation and pore removal. However, our success in synthesis of exotic single-phase thermoelectrics using high-pressure techniques borrowed from the Earth Sciences pointed the way to a method of achieving a dense material with small grain size and short-range chemical heterogeneity. Typically high-pressure experiments are to synthesize phases that are not stable at ambient pressures [82], but high-pressure sintering has also been used in ceramics processing to limit grain growth during the sintering process [81]. A simple approximate theory of sintering by diffusion creep was developed using a Nabarro-Herring model to predict the densification rate at high stresses. This model suggested that densification by creep could be made to dominate over both grain growth and chemical diffusion. The development of this simple model and tools for applying it sintering performance is the subject of the next section.

The terms stress and pressure are used with caveats in this chapter. The experimental apparatus is primarily designed to achieve near-hydrostatic high-pressure conditions. At these conditions the differential stresses are much smaller than the mean stresses. This is accomplished through the use of weak solid pressure media around the sample volume. However, when the starting material is a powder or porous material there is necessarily a transient period upon compression where the stress field is quite complicated. Under this condition the pressure in the void space is approximately zero, whereas the maximum compressive stress in the solid network approaches the applied uniaxial load. This is a

difference in stress of a few GPa, which will drive the sintering process. The sintering process of interest will continue to operate until this stress difference relaxes. The stress state, however, cannot relax into a near-hydrostatic state until the sintering stops. We therefore approximate the differential stress driving the sintering by the applied uniaxial compressive stress, which is numerically equal to the expected pressure at the end of the compaction transient if the experiment were run long enough to achieve the near-hydrostatic state. While it is differential stress that drives creep and densification, it is appropriate to loosely speak of the applied pressure as the driving force and as one of the independent variables in the experiment.

5.1.1 Preliminary Sintering Model

In order to guide our experiments a model was found to describe the densification mechanism at high pressure. For this line of experimentation to bear fruit it was critical that plastic deformation mechanisms far outstrip grain growth and chemical diffusion. The pressure range of experimental conditions suggested a suitable flow law; in our case a volume diffusion or Nabarro-Herring creep model. Hot pressing techniques have been rigorously employed for materials densification applications since the 1950s [80]. Our choice of the Nabarro-Herring model is justified from empirical observation of densification mechanisms in other materials systems. A map of densification mechanisms for very fine-grained materials invariably attributes the bulk of high-stress densification to a Nabarro-Herring mechanism. The factors on densification include temperature, pressure, time, as well as materials properties: grain size and microstructure. At our high-stress (several GPa) experimental range the Nabarro-herring theory provides

us with a useful model of densification via plastic deformation. In order to justify our experiment, however, it must be clear that the plastic deformation mechanism does dominate the densification behavior. As a first indication of what to expect from our experiments, we defined a sintering figure of merit. This value is the ratio of a diffusion creep strain rate to a pure chemical diffusion rate. In real systems both rates would contribute to the total densification observed in the material. Since densification is limited by the slowest diffuser along the fastest path, we can pick a value for our sintering figure of merit such that the plastic deformation mechanism completely dominates the behavior of densification under those conditions. We then designed test experiments to achieve a predicted sintering figure of merit greater than ten. Combinations of pressure, temperature and time parameters predicted to achieve this criterion are in fact well within the reach of our equipment. Success in our preliminary experiments shows *a posteriori* that the simple theory is a useful guide to choice of sintering conditions.

The Nabarro-Herring model requires information that is easily accessible *a priori*. The self-diffusion coefficient, grain size, temperature, time and stress are the required components of the equations. With grain size and self-diffusion coefficient fixed by our starting materials, we were able to vary the remaining variables to determine those conditions suitable for our work. This approach confirmed several trends that one would expect in a densification experiment:

- Increasing the temperature at constant pressure reduced the sintering time for a given densification to occur.

- Increasing the pressure at constant temperature reduced the sintering time for a given densification to occur.
- Typical hot-pressing conditions result in a densification mechanism dominated by chemical diffusion.

These trends neatly describe known behavior in the sintering of materials systems. This suggests that the model may make useful predictions about untried sintering conditions.

Indeed, preliminary high-stress syntheses resulted in very low-porosity bulk materials. Analysis by electron backscatter diffraction (EBSD) and electron-beam induced energy-dispersive X-ray spectroscopy (EDS) techniques confirms that these materials are crystalline, have grain sizes of tens of nanometers, and are chemically heterogeneous on the grain scale.

5.2 Theory

5.2.1 Densification Mechanisms

Sintering of materials is the consolidation of a powdered product during firing, typically undertaken to develop material properties and microstructural features. Partial sintering leads to a porous product, while full sintering leads to a fully dense product. Control parameters available to design sintering processes typically include the time, temperature and applied pressure or state of stress. In ceramic systems the "green body" is the unfired state where the material density is commonly 65% of theoretical or below [96]. After sintering, the material density is commonly much higher. The final goal of sintering is usually to approach the limit of full theoretical density. At low differential stresses, the densification mechanisms are mainly mass transport via diffusion across the neck of particle-particle contact and grain growth. All sintering is driven by the reduction in total free energy, which under low-stress conditions is usually dominated by the reduction in surface area

$$\Delta G_T = \Delta G_V + \Delta G_b + \Delta G_S \tag{5.1}$$

where ΔG_V, ΔG_b, and ΔG_S represent the change in free energy associated with the volume, boundaries (i.e. grain-grain contact areas), and surfaces (i.e. grain-void contact areas) of the grains [83]. Several mass transport mechanisms are active during the sintering process; many of them can lead to densification:

- Surface diffusion results in surface smoothing and particle joining without any real reduction of pore volume.

- An evaporation-condensation mechanism can result in similar effects, again without any increase in overall sample density.
- The boundary and lattice diffusion processes produce both neck growth between neighboring particles and volume shrinkage in the entire solid (Figure 5.1).
- Viscous flow results in densification, but is dependent on a wetting liquid at the surfaces to facilitate mass transport.
- Plastic flow is the inelastic deformation of a solid as a result of applied load and results in densification of the solid (Figure 5.1).

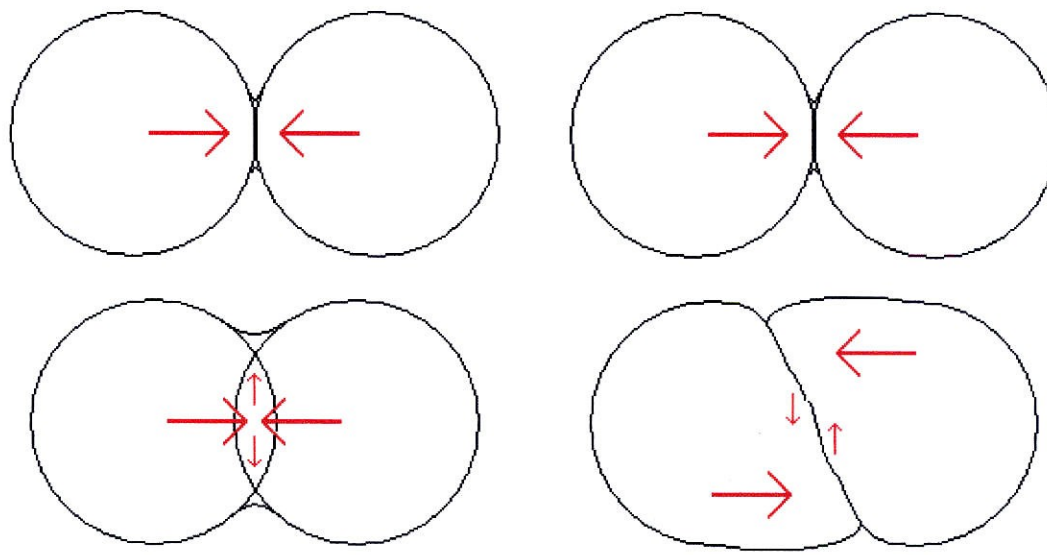

Figure 5.1: Diagram illustrating necking and volume reduction in a two sphere model on the left and the joining of particles via plastic deformation on the right.

The initial particle distribution has a significant impact on the sintering behavior of the solid. Smaller particles are more reactive, with larger surface to volume ratios, and therefore densify faster at a given temperature than coarser particles, reaching a higher final density for any given sintering time. Hot-pressing improves densification tremendously, outstripping particle size effects and resulting in higher density at lower temperatures and times.

Densification under plastic deformation is of particular interest for this work. Such flow processes are known as creep, which can be defined as continuing plastic deformation under constant stress. Creep models are utilized, e.g., to predict the safe lifespan of components held or cycled at elevated temperatures or pressures. Processing handbooks, however, may completely omit references to creep mechanisms, but the flow laws behind the models are applicable to synthesis, in addition to materials failure analysis.

While failure analysis may consider plastic deformation only as far as the onset of deformation at failure, continuous plastic deformation occurs so long as differential stress is applied. If the microscopic mechanism allowing creep is the diffusive transport of point defects (generally vacancies) through the bulk of grains, then the Nabarro-Herring model is used to describe the behavior. In this case the densification rate is inversely proportional to the square of the grain size [85, 90]. If the transport of matter is along the grain boundaries then a Coble creep model is used to describe the behavior. In Coble creep the densification rate is proportional to the grain boundary width, resulting in a densification rate inversely proportional to the cube of the grain size [91]. If the process conditions involve extremely high pressures or temperatures and favorable chemistry and microstructure are in evidence, then power law (i.e., dislocation) creep becomes a significant contributor to the densification rate [88].

In addition to creep mechanisms, superplasticity can be in evidence during high-pressure sintering. Superplasticity involves a combination of grain boundary sliding and grain

switching, which results in a change in physical grain configuration without requiring that atoms diffuse across grain boundaries [89]. The mechanism can be seen schematically in Figure 5.2.

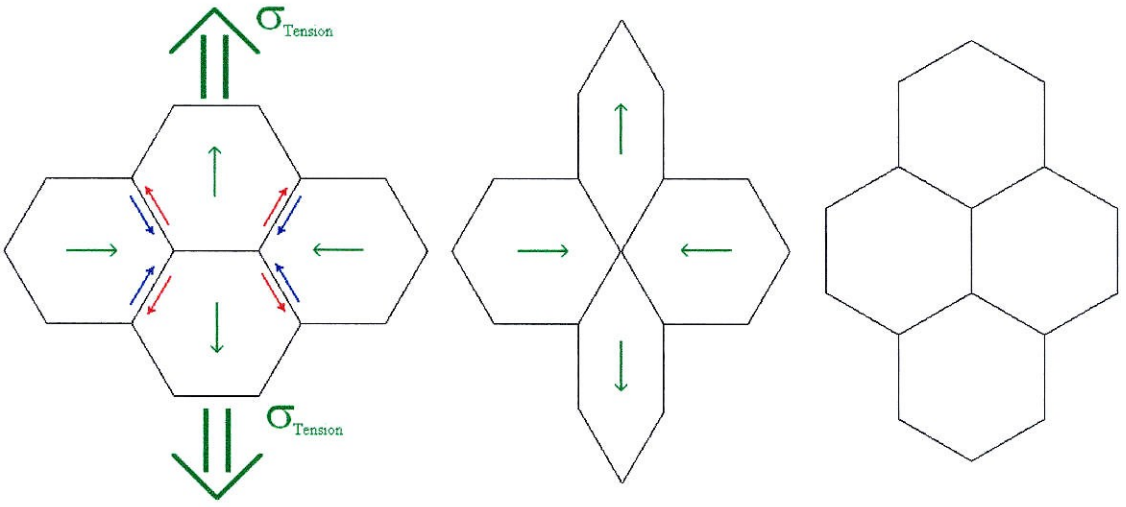

Figure 5.2: Initially, an array of grains is under some large stress. In a superplastic system neighboring grains slide along one another creating an unstable transition state (center) and finally resulting in a stable configuration that is dissimilar to the original.

These mechanisms all contribute to a system under plastic flow. In order to make a prediction, an appropriate governing equation must be selected. For our purposes, a flow law was selected that describes material behavior under great stress. At stresses between 0.5 and 5GPa the dominant mechanisms for deformation were found to be modes of plastic deformation [90]. The appropriate creep flow law should therefore provide an initial expectation for sintering rate.

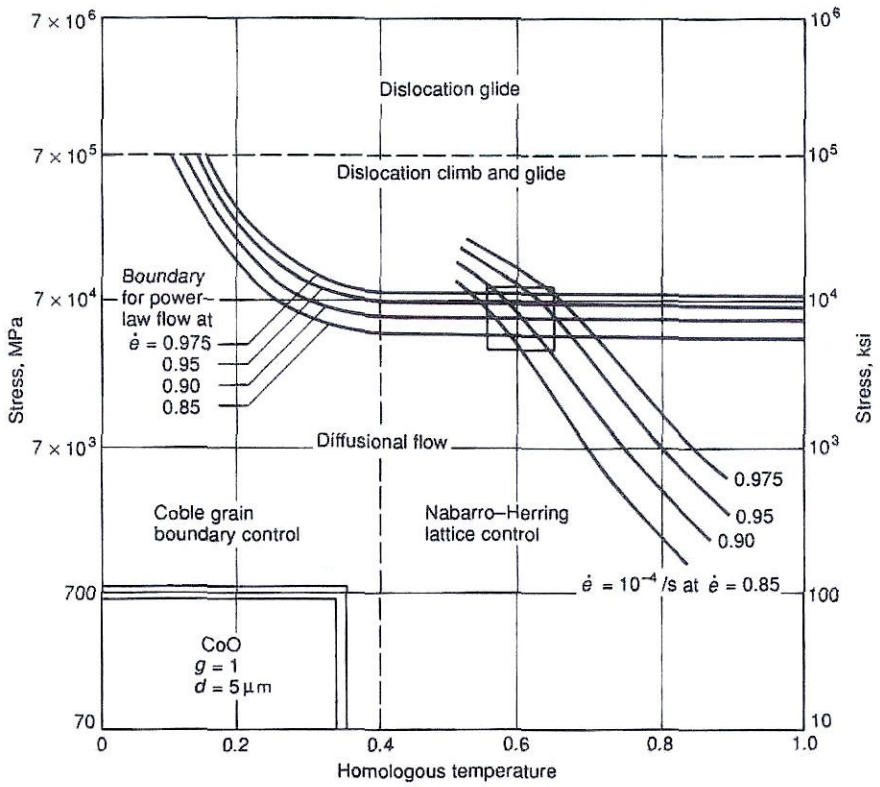

Figure 5.3 Deformation map for a ceramic system showing the active mechanism as a function of homologous temperature (T / Tm) [91].

The choice of a creep model for high-pressure densification can be further justified by examining a deformation map and extrapolating those results for the materials system of interest. The various densification mechanisms can be plotted together determining the relative contributions of each for a given set of process variables, such as temperature and stress [92]. Figure 5.3 shows one such deformation mechanism map, in this case for the CoO system [91]. The homologous temperature used on the axis is the process temperature normalized by the melting temperature for the material in question. The densification time, or strain rate, allows the prediction of the third parameter if a second is known. The use of a Nabarro-Herring model for high-pressure densification follows from the relative positions of the dominant mechanisms; in particular, the very small

grain size of the nano-particle aggregates of interest greatly enlarges the Nabarro-Herring field relative to the Coble and power law fields. This follows from the strain rate dependencies for both Nabarro-Herring and Coble creep; the strain rate in Nabarro-Herring creep is inversely proportional to the square of the grain size, while the strain rate in Coble creep is inversely proportional to the cube of the grain size. Armed with an appropriate model for high-pressure behavior during hot-pressing a prediction of appropriate sintering conditions can be attempted.

5.2.2 Nabarro-Herring Creep

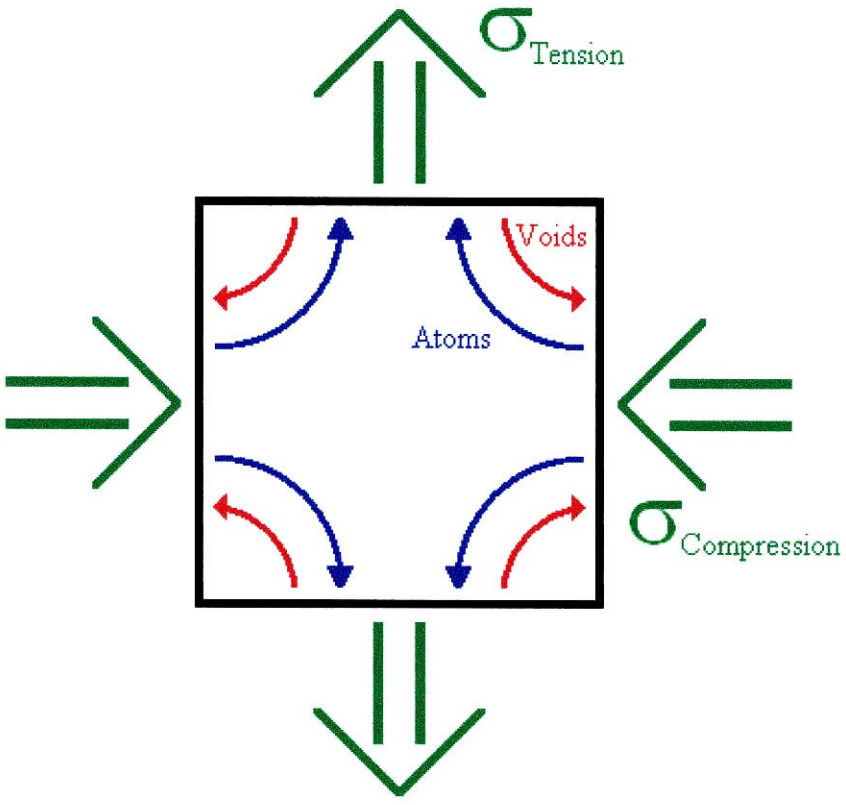

Figure 5.4: Illustration of square grain model for the Nabarro-Herring Creep model.

The Nabarro-Herring model describes a process schematically shown in Figure 5.4. The model is a simple square grain undergoing plastic flow in response to applied stress [19]. Atoms migrate from the compression face to the tension face of square grains while voids migrate in the opposite sense. Flow migration is stress induced, in response to stress gradients through the square grain. The following presentation is adapted from the work of Poirier [93]. The concentrations of vacancies on the compression face (C^-) and the tensile face (C^+) are a function of the equilibrium concentration of vacancies C_O, the applied stress σ, the vacancy volume V, the gas constant R and temperature T. A

compressive stress will decrease the concentration of vacancies, while a tensile stress will increase the concentration

$$C^- = C_o \exp\left(-\frac{\sigma V}{RT}\right) \qquad C^+ = C_o \exp\left(\frac{\sigma V}{RT}\right) \tag{5.1}$$

The flux of vacancies to the face in compression from the face in tension, and matter in the opposite direction, is then just the diffusion constant for vacancies times the concentration gradient

$$J = -D_V \, grad C = \frac{\alpha D_V \left(C^+ - C^-\right)}{d} \tag{5.2}$$

where α is a material constant and d is the grain size. Substituting equation 5.1 into 5.2 and computing the change in grain dimension as the flux times the volume of vacancies being transported, we recover a strain rate

$$\Delta d = \frac{J d^2 V}{d^2} = JV \qquad \dot{\varepsilon} = \frac{\alpha D_V C_O V}{d^2} \sinh\left(\frac{\sigma V}{RT}\right) \tag{5.3}$$

But the equilibrium concentration of vacancies times the volume of vacancies is just the volume per vacancies in the solid, or N_V, allowing one to cast the strain rate in terms of the self-diffusion coefficient, D_{SD}, for the material

$$D_V C_O V = D_V N_V = D_{SD} \qquad \dot{\varepsilon} = \frac{\alpha D_{SD}}{d^2} \sinh\left(\frac{\sigma V}{RT}\right) \tag{5.4}$$

For a low stress and high temperature case, or anywhere $\sigma V << RT$, the hyperbolic sine term can be replaced with its argument ($\sinh(x) = x$ as $x \rightarrow 0$)

$$\dot{\varepsilon} = \frac{\alpha D_{SD} \sigma V}{d^2 RT} \tag{5.5}$$

From either Equation 5.5 or 5.6 we can see that the materials constant required for this model is the self diffusion constant, a well known quantity for both silicon and germanium [94, 95]. We take an accumulated strain of unity as a characteristic criterion to define the sintering time. The assumption here is that a strain of one corresponds to sufficient deformation to approximately convert a loose powder to a fully dense state. With this assumption, knowledge of the self diffusion constant and the grain size, we can compare this densification mechanism against the competing mechanisms we wish to avoid. The sintering figure of merit is the Nabbaro-Herring creep densification rate (i.e. one over the time to reach a strain of unity) divided by the rate of the principal competing mechanism. In this case the competing mechanism is chemical homogenization by inter-diffusion (for silicon-germanium composites) or densification by grain growth (for pure silicon or germanium). We further assume that any value of the sintering figure of merit greater than 10 will result in a bulk structure where plastic deformation and grain sliding dominates the densification routes; this yields a simple criterion for a candidate synthesis experiment. Plotting our sintering figure of merit against sintering time produces the plots seen in Figures 5.5, 5.6, and 5.7. Initially the commonly used linear Nabarro-Herring model (Figure 5.5) was utilized. The linear regime holds only when $\sigma V << kT$, and since kT varies from 0.32 at 1000 °C to 0.14 at 1400 °C our pressure cannot exceed 10^3 or 10^4 Pa for the approximation to hold. Even under conventional hot-pressing techniques the pressure can reach 10^7 Pa, so we must switch to the non-linear Nabarro-

Herring model as seen in Figure 5.6. Figure 5.7 is the same non-linear model but for germanium instead of silicon. The hyperbolic sine term in the non-linear model greatly accelerates the stress activated densification mechanisms.

The plots of our sintering figure of merit illustrate why traditional hot-pressing techniques have failed to synthesize dense, nano-crystalline, chemically heterogeneous aggregates of silicon and germanium. The plots also indicate that conditions attainable in our high-pressure equipment will succeed. There is no combination of temperature and time at which the maximum stress generated by the low-pressure sintering commonly available to researchers in silicon-germanium thermoelectrics will reach a dense state without significant grain growth and chemical diffusion. The sintering figure of merit for standard synthesis techniques is well below unity, meaning the chemical diffusion and grain growth mechanisms are much faster than the plastic deformation mechanisms we need to maintain our chemical diversity and small grain size. Hence standard techniques necessarily lead to total loss of chemical diversity and nanostructure in sintered silicon and germanium nanoparticles. The plots of the sintering figure of merit versus time also show us that the experimental stresses attainable with high-pressure synthesis push the sintering figure of merit well above ten, which was the arbitrarily chosen target to pursue this experimental technique. A sintering figure of merit of 10 indicates that a diffusion creep sintering mechanism will act to sinter a material ten times as quickly as a chemical diffusion mechanism.

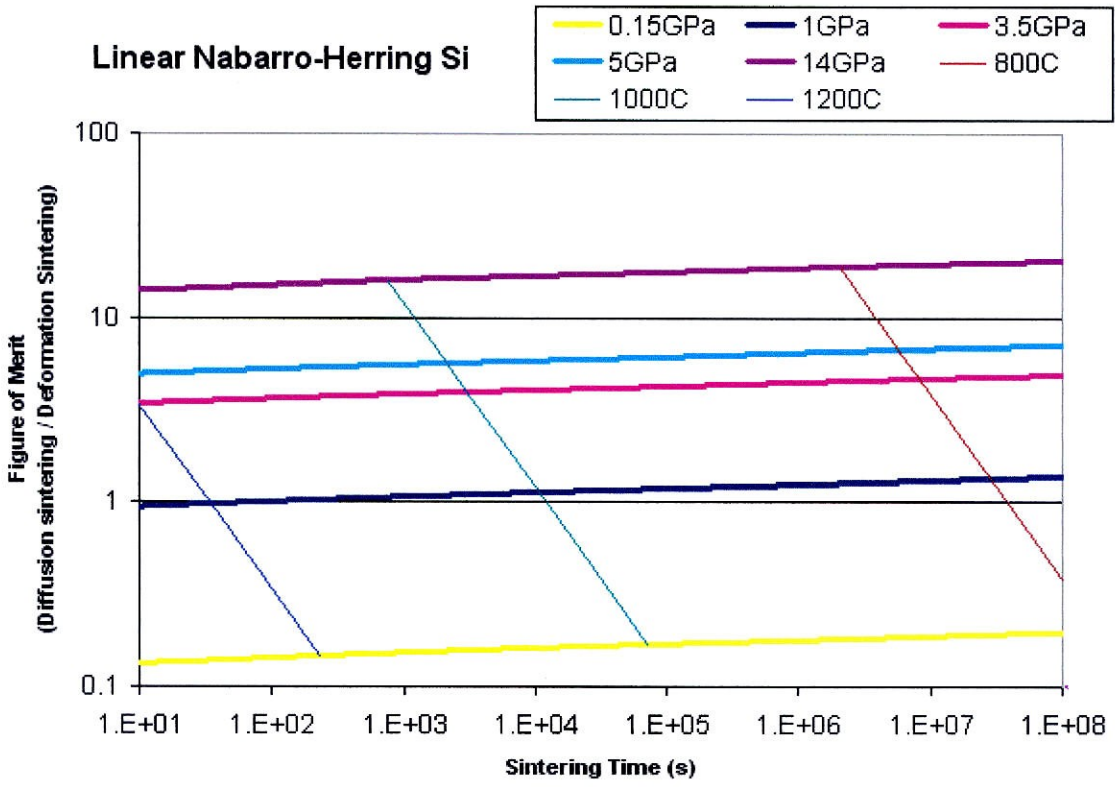

Figure 5.5: Synthesis figure of merit vs. sintering time for the linear Nabarro-Herring model in silicon.

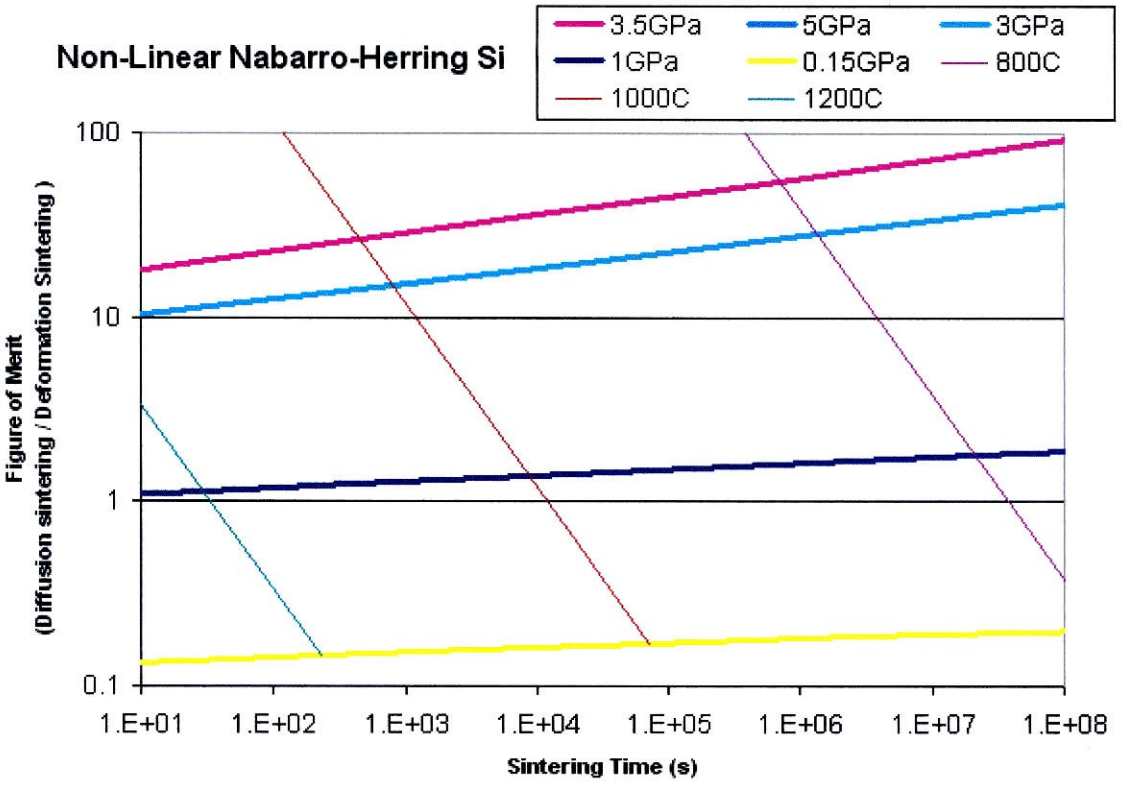

Figure 5.6: Synthesis figure of merit vs. sintering time for the non-linear Nabarro-Herring model in silicon.

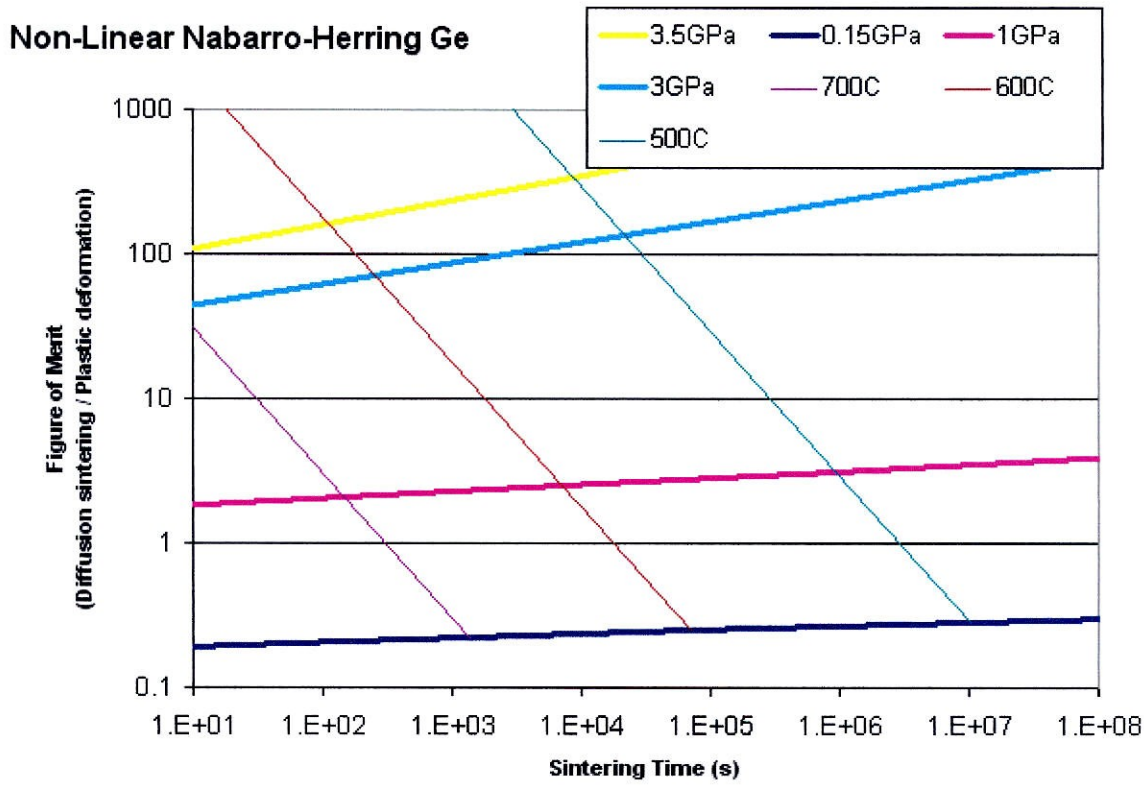

Figure 5.7: Synthesis figure of merit vs. sintering time for the non-linear Nabarro-Herring model in germanium.

5.3 Experimental

5.3.1 Synthesis

Bulk starting materials were acquired from several standard sources. Raw materials included: commercially available nano-particle silicon (Sigma-Aldrich) with a particle size of 60 nm, 10 nm germanium particles from the laboratory of Dr. P. Holder (Northwestern, Illinois), and 200 nm silicon and germanium compounds mechanically mixed in a high energy ball mill at JPL. These nano-particles, due to their high surface area, were highly reactive and were stored and used in a glove box with a controlled argon atmosphere. All sample loading, weighing, measuring, mixing, etc. was performed under controlled atmospheric conditions. During the final stages between assembly loading and pressing the packed furnace stack is no longer stored in a controlled argon atmosphere. The stack is not airtight, but the sample is buried inside the assembly and this brief opportunity for exposure has not resulted in any difficulties to date.

A 300-ton end-loaded piston cylinder device was used for the bulk of these high-pressure experiments. A piston cylinder device compresses a sample assembly and resistance heater by driving a piston into the cylinder wherein the sample assembly is confined. Heating is controlled by varying the power through the furnace and correcting the output with the use of a thermocouple inside the sample assembly and near the sample. The tungsten carbide cylinder is kept in a compressive state of stress radially by press-fitting into steel containment rings, and axially using a hydraulic end-load on our two-stage press frame. Together, these steps greatly increase the load the cylinder can bear,

allowing routine operating pressures of up to 3 GPa for the 0.5" device and 2 GPa for the 0.75" device [100]. The main components of the press are illustrated in Figure 5.8. Most of the components are steel; however the core and piston are tungsten carbide. Pressure during synthesis was maintained with hot piston-in control [97], wherein the pressure is brought up to the final desired load after the run temperature is achieved in order to minimize frictional hysteresis resulting from piston retraction as the assembly parts expand.

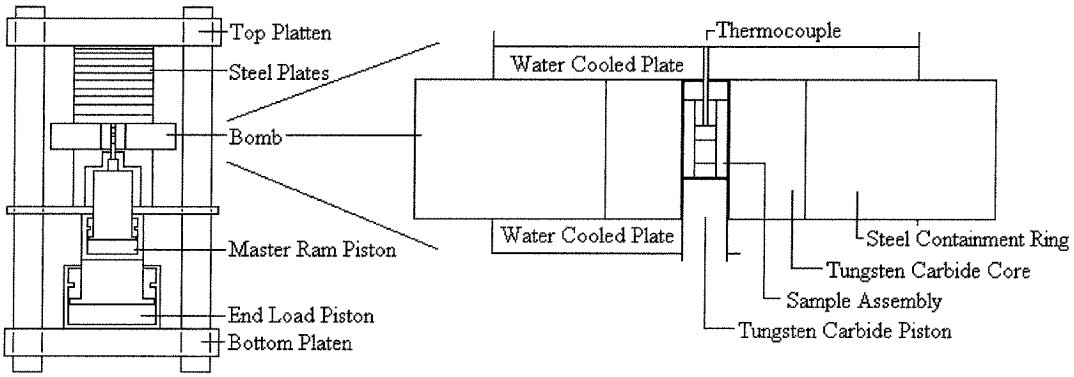

Figure 5.8: Schematic diagram showing the pressure vessel components and major features of an end-loaded piston-cylinder apparatus, adapted from Dunn [98].

The pressure assembly consisted of a CaF_2 sleeve with graphite furnace and bottom plug. The space inside the heating cylinder and below the sample was filled with either MgO or CaF_2 depending on the stage of synthesis. Graphite plates were used to contain the sample volume; this barrier was necessary to prevent leakage of our powders, contamination from assembly furniture, and contamination of our thermocouple. The space inside the heating cylinder and above the top graphite disk was single-hole crushable MgO, with a mullite sleeve protecting the axially-oriented thermocouple. For

lubrication purposes, a thin lead foil was wrapped around the CaF_2 sleeve before insertion into the cylinder of the piston cylinder press. Figure 5.9 illustrates this assembly.

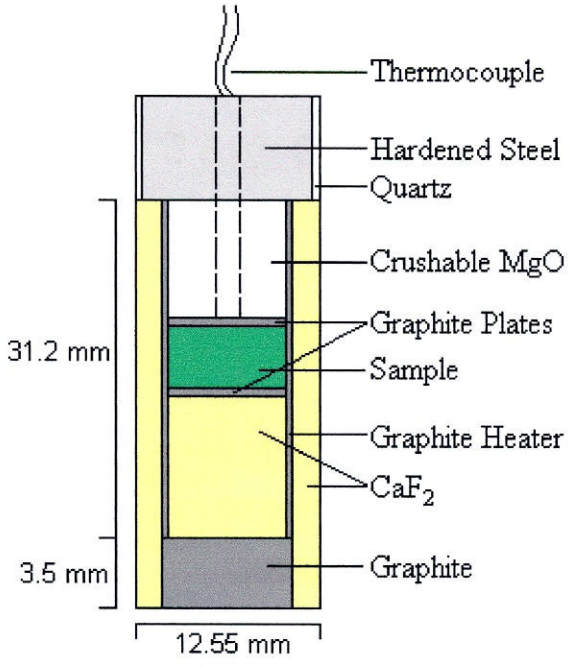

Figure 5.9: Piston-cylinder pressure assembly shown in cutaway view. The sample volume in these assemblies is typically 5.5 mm in diameter and 4 mm in height. Sample heights of up to 15 mm were experimented with in attempts to increase the volume of our synthesis experiments.

Pressure calibrations in the piston cylinder apparatus were performed by charting well understood phase transitions in pressure-temperature space with our particular press and methodology. The resulting empirical relation between sample pressure and oil pressure behind the piston is in practice more accurate than any attempt to account for every source of friction in the entire device [99, 100]. Our key calibration point is the quartz-coesite transition at 3.1 GPa and 900 °C. In the absence of other calibration points we assume a constant "friction correction" between the nominal pressure and sample pressure. The thermocouple electro-motive force (emf) was not corrected for pressure effects in our experiments, as the corrections are expected to be on the order of 10 °C [99]

and not critical for our synthesis work. A Type C W5%Re – W26%Re axially mounted thermocouple was used to read and control the sample temperature.

The high-pressure synthesis method has been refined over much iteration, resulting in a two-step pressing technique. The primary pressing starts with loose nano-particles while the secondary pressing takes the result of the primary pressing and finishes the compaction, resulting in a monolithic sample of our desired volume and nanostructure. Primary synthesis begins under an argon atmosphere. As nano-particle physical behaviors are dominated by surface charge effects rather than gravity care must be taken when handling them. Conventional weighing boat and papers build up static charge, while molybdenum foil can discharge any buildup easily. Initial starting materials are weighed out and loaded into a prepared furnace stack making use of molybdenum foil for weighing paper and a purpose-built aluminum funnel for loading the furnace stack. After the necessary volume of powders has been put into the furnace, the upper graphite plate and MgO anvil are put into place. The entire furnace stack is then wrapped with tape, to keep the top and bottom anvils in place, and sealed in a plastic bag for transit outside the glove box. Once at the press the pressure assembly is prepared for pressing and high-pressure synthesis begins.

The second pressing begins with the results of the primary pressing stage. The material is manually powdered and loaded into another pressure assembly. Since the particle size is approximately 60 μm the initial packing density in the furnace stack approaches 65%. This particle size is three orders of magnitude larger than in primary pressing and allows

a higher initial density in the powder compact. At this stage the particles are much less reactive and extraordinary environmental precautions are not required. The loaded pressure assembly is inserted into the press and the high-pressure experiment begins. The pressure assembly for the secondary pressing makes use of thick graphite plates and replaces the MgO below the sample with CaF_2 in an effort to assist in strain recovery as the pressure is released [49, 101]. This coupled with the careful control of decompression rate and temperature helps produce the largest volume samples and minimizes the occurrence of the delamination cracks always resulting from primary pressing [102].

5.3.2 Characterization

Sample density was measured using three techniques. A geometric estimate of density was used to confirm that samples had reached a sintered state during the high-pressure synthesis. While geometric measurements are reasonably accurate for products of standard hot-pressing synthesis in rigid containers, the quasi-hydrostatic pressure exerted on the sample in a high-pressure synthesis experiment deforms it from a regular shape that lends itself to the geometric measurement. Hence density of our irregularly shaped products was confirmed by immersion in toluene and by imaging in a Scanning Electron Microscope (SEM). The Archimedean technique of comparing weight of a sample in air with weight of the same sample suspended in toluene is accurate for measuring the density of samples with closed porosity. If A represents the mass of the sample dry, B represents the mass of the sample immersed, ρ_l is the density of the atmosphere and ρ_o the density of the immersion liquid (corrected for the temperature of the liquid) then the density of the sample is simply:

$$\frac{A}{A-B}(\rho_o - \rho_l) + \rho_l \tag{5.7}$$

Once our high-pressure experiments returned results of greater than 98% theoretical density we turned to SEM to image the surfaces and confirm the surface was free of open porosity. A typical image can be seen in Figure 5.10.

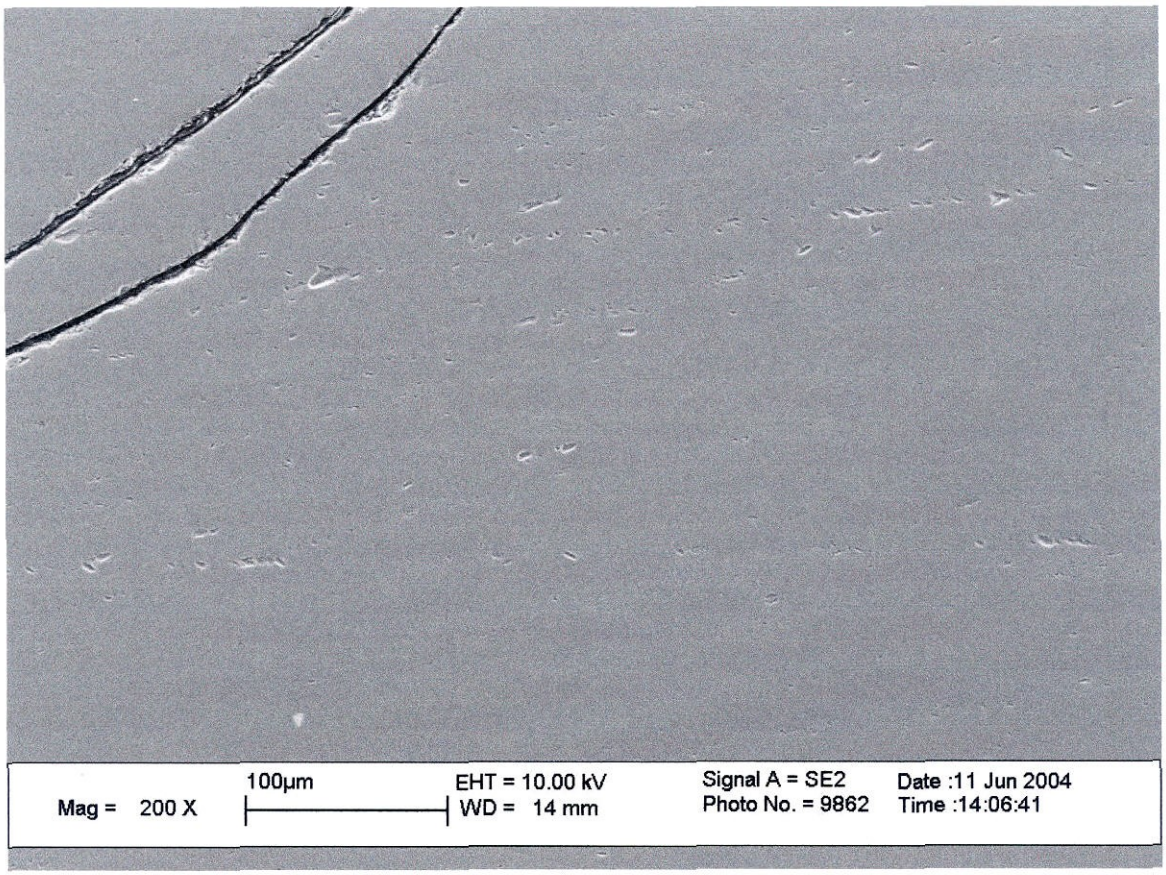

Figure 5.10: SEM image of silicon nanoparticles sintered at high pressures (3GPa). Horizontal pock marks are attributed to a polishing error, while the cracks in the upper left are due to internal stress in the sample.

Scanning electron microscopy (SEM) was used to characterize the surface features of our pressed samples and to explore the compositional and structural characteristics. The microscope used (Geological & Planetary Sciences Analytical Facility, Caltech) is a LEO 1550 VP FESEM, equipped with in-lens SE, below lens SE, variable pressure SE, and Robinson-type BSE detectors. Chemical analysis is performed with an Oxford INCA Energy 300 X-ray Energy Dispersive Spectrometer (EDS) system. Structural analysis is performed with a HKL Electron Back Scatter Diffraction (EBSD) system, including a Forward Scatter Electron (FSE) detector.

Scanning electron microscopy uses a beam of electrons scanned across the surface of the sample in order to excite secondary electrons from the sample that are subsequently observed in the detector. Imaging backscattered electrons is another mode of operation for the SEM, using high energy electrons that emerge nearly 180 degrees from the illuminating beam direction. BSE imaging yields an image that is sensitive to the mean atomic number of each point in the sample. Figure 5.11 shows the interior of the SEM chamber during an imaging session.

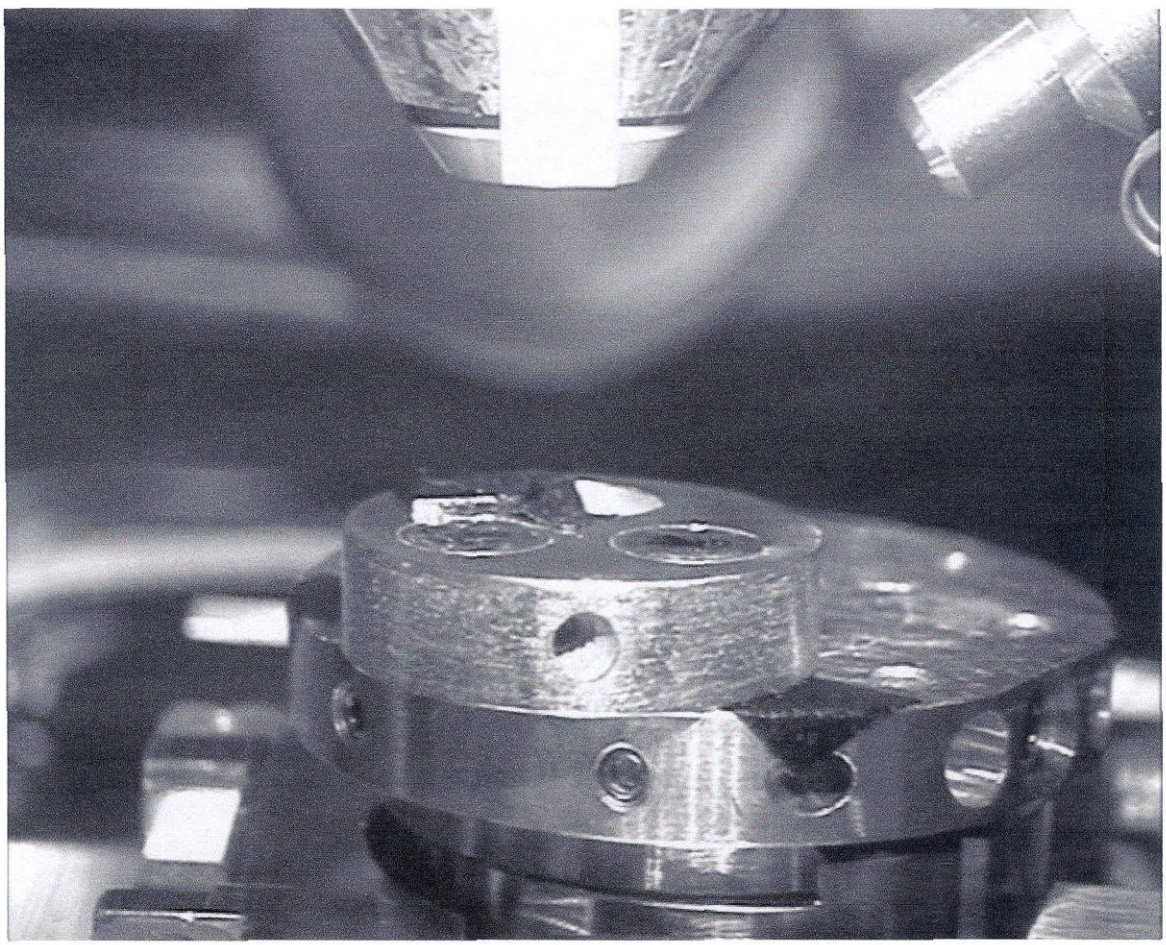

Figure 5.11: Interior of the sample chamber during imaging with the SEM. The objective lens and EDS detector are visible at the top and top-right portions of the image. On the central stage is a silicon standard and several of our pressed samples in epoxy. The silicon standard is fixed to the stage with graphite tape to prevent charge build up under the electron beam.

Energy Dispersive X-ray Spectroscopy (EDS) utilizes x-rays emitted from the sample when bombarded by the electron beam to identify the elemental composition. When the sample is bombarded by the electron beam of the SEM, electrons are ejected from the atoms on the surface. The resulting electron vacancies are filled by electron from higher shells and x-rays are emitted to balance the energy difference between the electronic states. In EDS analysis the energy of the X-ray photons is determined using a biased Si-crystal detector with a resolution of ~1.3 eV; the entire spectral range from ~250 eV to 20 keV is collected simultaneously. The resulting spectrum contains a background of bremsstrahlung X-rays together with the characteristic X-rays produced by the atoms in the sample. This spectrum can be used qualitatively to identify the elements present or quantitatively, with reference to standard materials and matrix correction algorithms, to determine sample composition to ~1% relative precision.

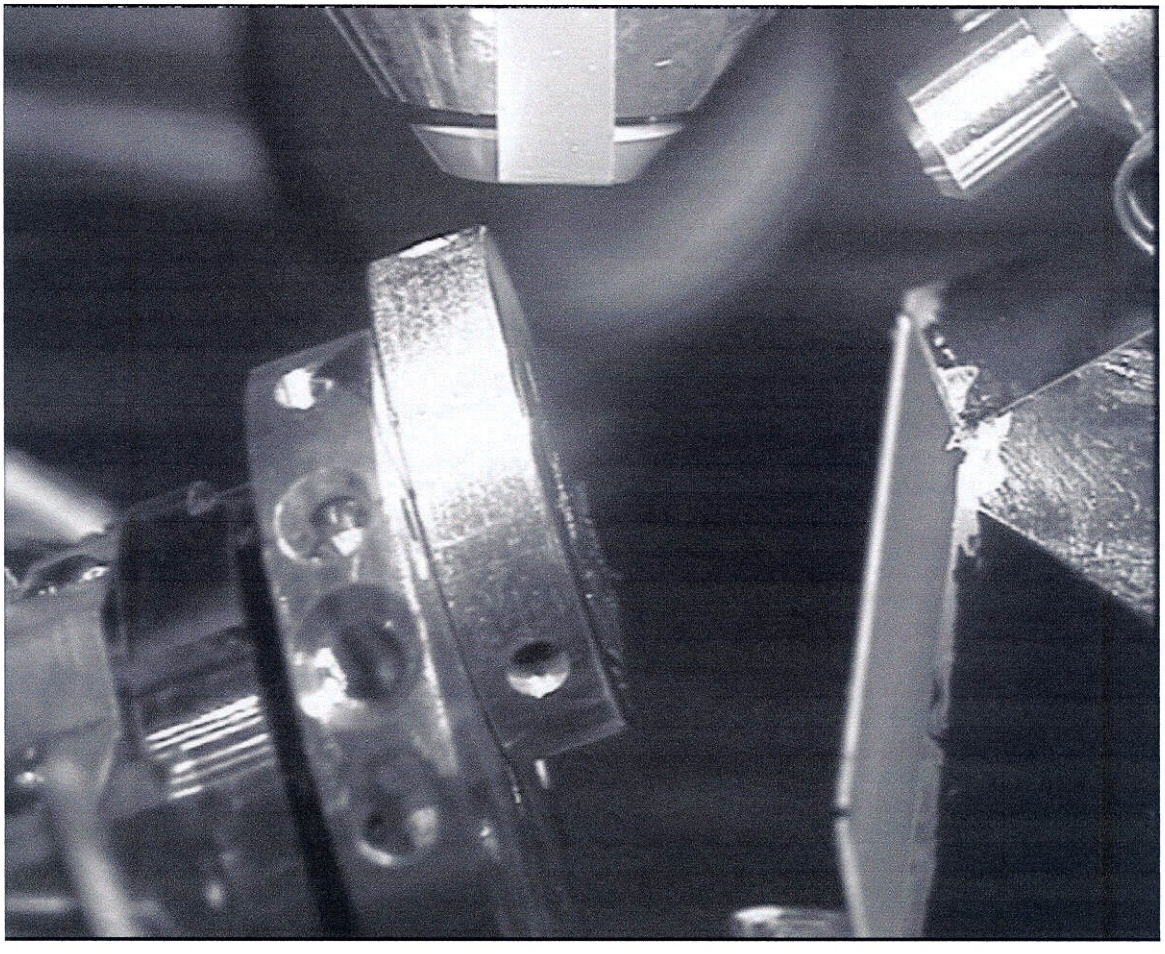

Figure 5.12: This image of the SEM sample chamber shows the stage tilted for EBSD analysis. The large square detector on the right is the EBSD detector.

Electron Back-Scatter Diffraction (EBSD) or Backscatter Kikuchi Diffraction (BKD) uses the incident electron beam to generate Kikuchi bands. The incident electron beam produces a divergent source of electrons within the activated volume of the sample, which interacts with the periodic charge distribution of the crystal lattice and diffracts according to the Bragg condition. These diffracted beams generate the band pattern where the diffraction cones intersect the detector. EBSD patterns can be used for crystal structure identification, orientation, and grain fabric analysis. Figure 5.12 shows the interior of the SEM chamber when configured for EBSD analysis. The box shape to the

right is the EBSD detector, and the stage is tilted aggressively such that the diffracted beams strike the detector array.

Samples were prepared for SEM characterization by mounting in epoxy and polishing the surface. The surface was polished to a submicron finish with a variety of polishing papers culminating with 0.25 μm diamond-paste on felt. An automatic vibratory polisher was then utilized (Buehler Vibromet 2, with Buehler Mastermet 2 non-crystallizing colloidal silica polishing suspension). The final polishing medium contains 0.03 μm colloidal SiO_2 and the samples were polished for a minimum of eight hours, providing a mirror finish.

Samples for transmission electron microscopy (TEM) were ion-milled to a thickness of several nm and supported on graphite foil. TEM techniques allow observation of grain orientation and atomic stacking. The TEM work was conducted by Dr. P. Holder II. (University of British Columbia, Canada).

Electrical and thermal properties were measured at JPL using their standard techniques, described previously (Chapter 2). Thermal conductivity, electrical conductivity, Seebeck and Hall coefficients were recorded for several silicon-germanium samples.

5.4 Results

Initial experiments resulted in sample masses of approximately 50 mg. These materials were mechanically unsound and easily parted into smaller pieces. The small initial sample volumes were a consequence of working with nano-particles. Nano-particle interactions are dominated by surface interactions, such as static charge. These particles do not compact together well and any agitation will cause the powders to leave whatever container they reside in. The second generation of high-pressure experiments generated sample volumes of up to 0.25 g. The samples recovered typically delaminated into pieces no more than 1.5 mm in height. While these samples were of suitable volume for some electrical and thermal characterization, the persistent delamination suggested that microscopic partings and fractures might be interfering with the bulk material property measurements. Further iterations of the high-pressure techniques have resulted in samples with heights of up to 6 mm. These samples are approximately 0.6 g, but continue to suffer the delamination of previous experiments.

SEM imaging of initial experiments showed a high density sample with decompression cracking but little pore space. Figures 5.13 through 5.15 show images from the first silicon and silicon plus mechanically mixed silicon-germanium samples. The lighter regions in the two-phase sample are the mechanically mixed silicon-germanium compound, which still shows porosity in these images (Figure 5.15). Such porosity was not apparent in the nano-silicon regions of those samples, nor in the entirely nano-silicon sample imaged in Figure 5.13. The difference is due to the initial grain-size of the starting materials. The mechanically-mixed silicon-germanium starting material has a

grain size of at least 200 nm. For this material, the grain size may be large enough that Nabarro-Herring creep ceases to be the dominant mechanism. The sintering figure of merit may be much lower than for the 50 nm or smaller grain size in the nano-silicon starting material. If these pore structures pre-exist in the silicon-germanium starting material, and are separated from grain boundaries, then it is possible the Nabarro-Herring creep acted to consolidate smaller pores within each grain. Such a mechanism would eventually lead to densification, but may require larger strains to accomplish.

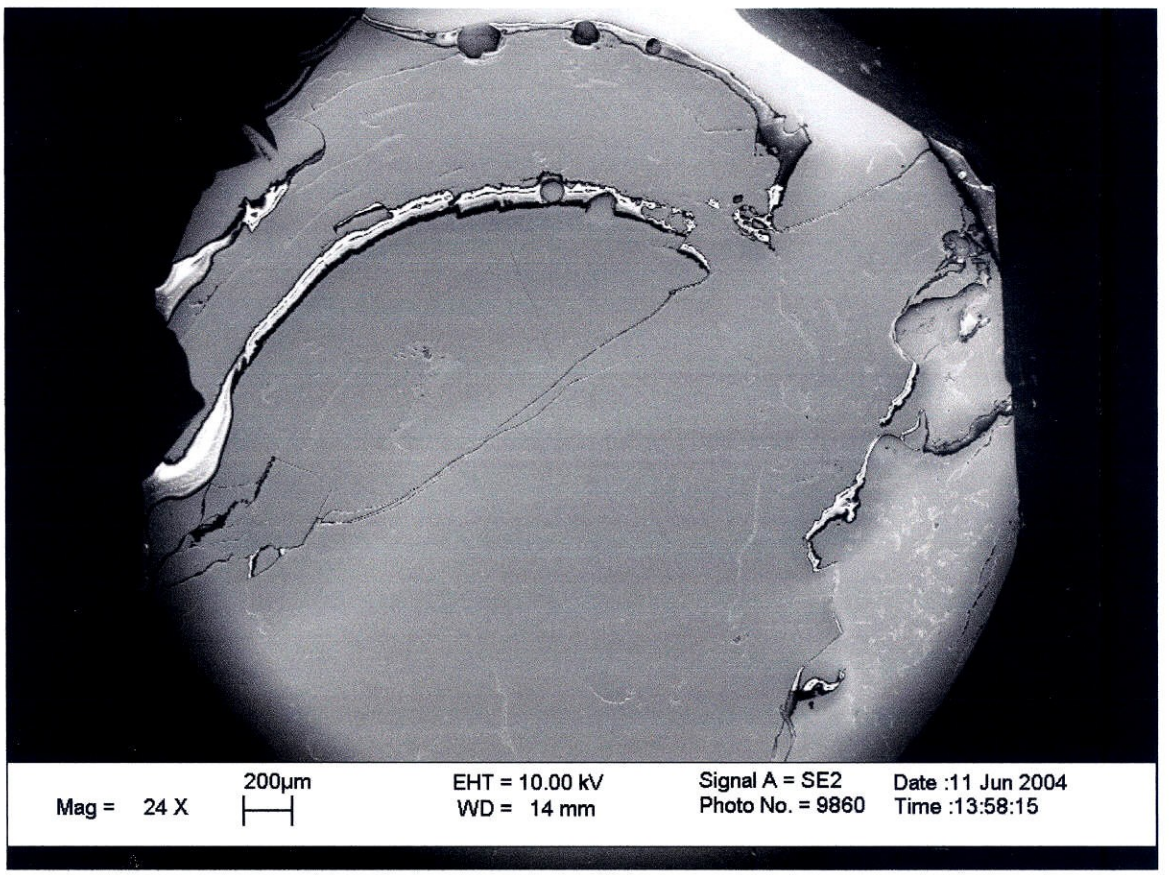

Figure 5.13: SEM image of nano-silicon powder hot-pressed at high-pressures.

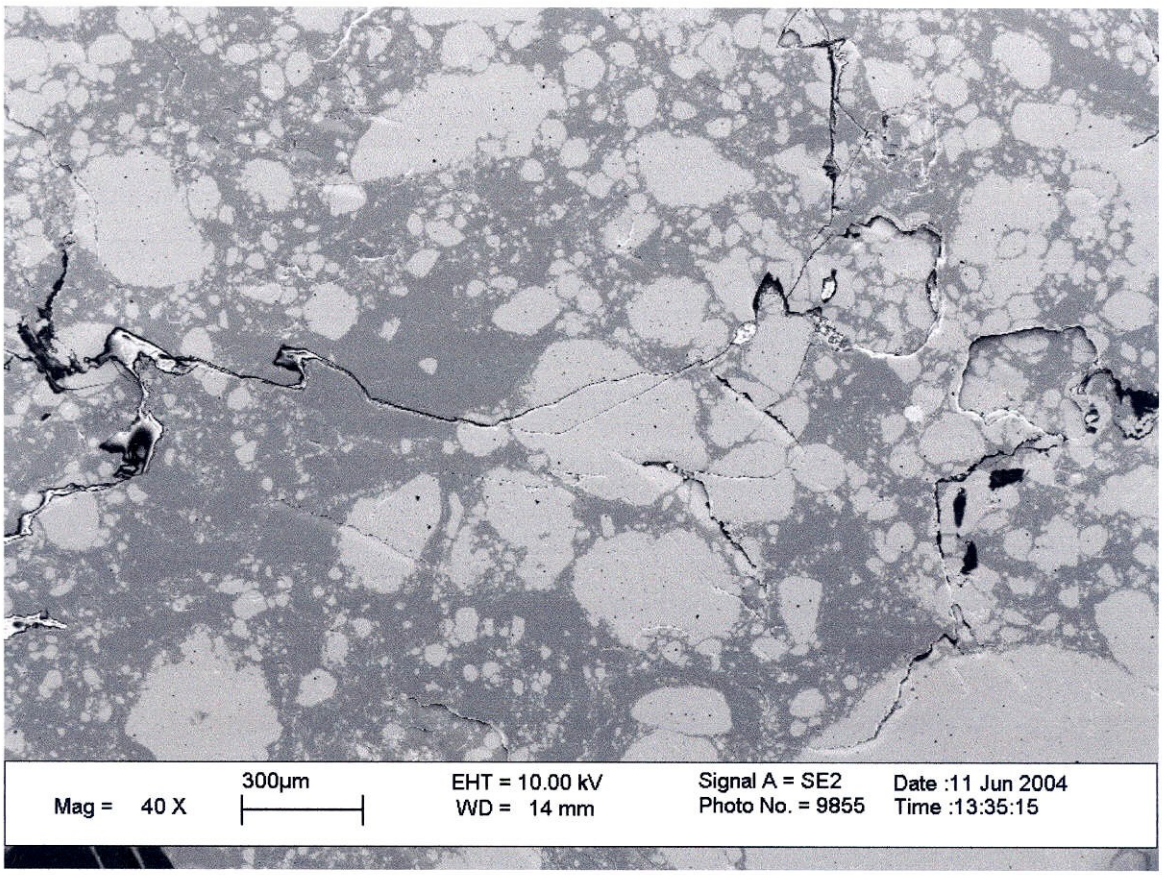

Figure 5.14: SEM image of mechanically mixed silicon-germanium plus nano-silicon sample. Starting materials were mixed in a 50-50 ratio, in this image the silicon-germanium mixture is the light colored phase. Cracking observed is attributed to the high-pressure technique.

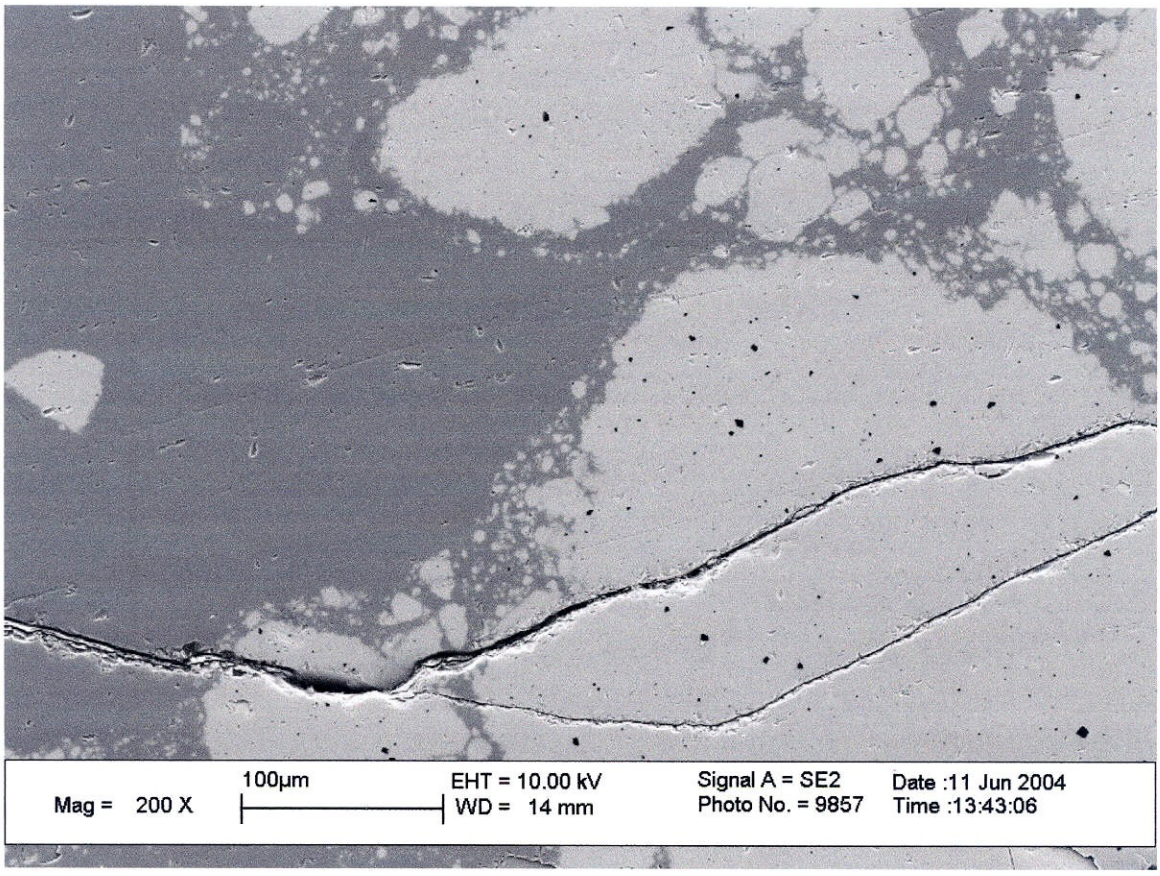

Figure 5.15: Closer magnification of SEM image of mechanically mixed silicon-germanium plus nano-silicon sample. Note the visible pores in the mechanically mixed portion, and the lack of porosity in the nano-silicon regions.

EDS measurements on these samples showed pure silicon for the nano-silicon sample, as well as for the darker regions of the two phase sample imaged here. The lighter region in the two-phase sample show the large particles made up of $Si_{0.8}Ge_{0.2}$ grains. There was no germanium observed in neighboring regions. The only difference was the $Si_{0.8}Ge_{0.2}$ starting material was doped with 0.8% boron, which was not detected. Due to the weak Kα X-Ray emission from boron being readily absorbed by the silicon-germanium matrix, the boron content in our sample is well below the detection limit for this device. The chemical heterogeneity and purity of the nano-silicon regions reflects the composition of

our starting material and indicates that chemical diffusion was not very active during sintering.

SEM EBSD analysis suggested that the resulting silicon material was crystalline with a grain size of approximately 50nm. Under ideal conditions the EBSD technique can automatically detect crystal orientation at a point in the sample and map the entire surface. While a few points provided a strong enough signal to allow identification of a silicon crystal structure, the kikuchi pattern was not strong enough to allow automatic identification. Frequently the investigator would be able to make out 4 bands and one or two nodes of the kikuchi pattern. This allowed some grains to be oriented, which allowed the operator to assign a size to various grains. The grains identified by this method were on the order of 50 nm in diameter, but the quality of the kikuchi information was insufficient to generate an orientation map for the samples investigated.

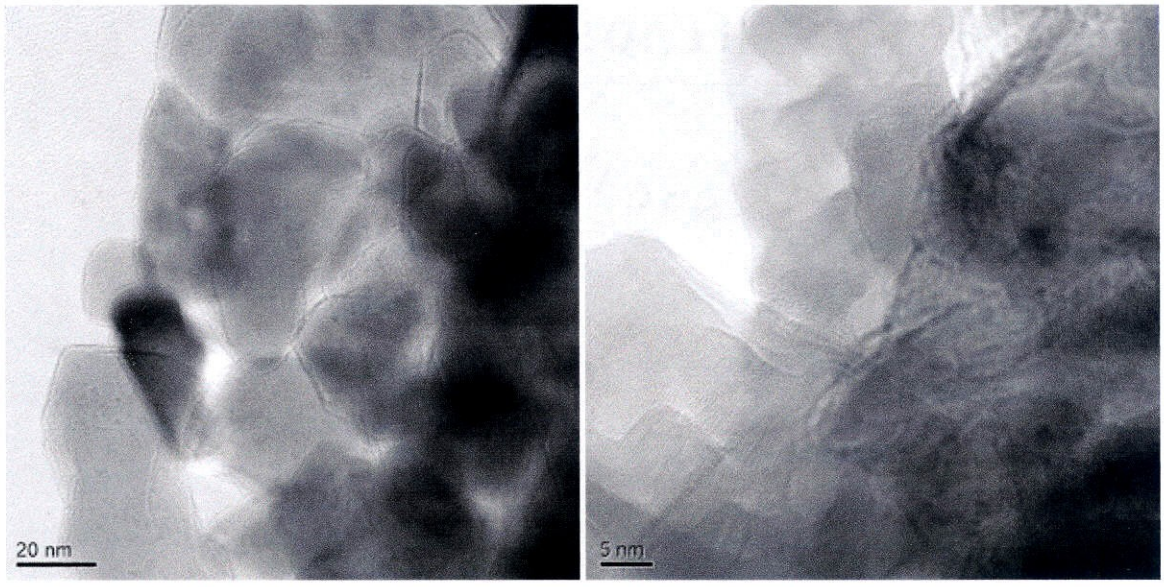

Figure 5.16: TEM images of a nano-silicon sample. Note the individual grains on the order of 10-60 nm.

Transmission Electron Microscopy was employed to confirm the crystalline nature and the grain size of our sintered materials. Samples were ion milled to a few angstroms thickness and supported by graphite foil. As seen in Figure 5.16, the sintered nano-silicon samples are crystalline with a grain size of 10-60 nm. The rows of atoms clearly indicate different crystal orientations between neighboring grains.

Density measurements by geometrical means indicated densities from 90% to 98% depending on the regularity of the sample dimensions. The more accurate Archimedean technique yielded densities closer to 99% of theoretical, as in Table 5.1.

			Dry (mg)	Wet (mg)	ρ
Toluene	0.8627	g/cm^3			
Temp	23.2	C	659	412	2.297
Silicon	2.33	g/cm^3	660	412	2.291
Observed	2.296	g/cm^3	660	412	2.297
Percent			659	412	2.291
Theoretical	98.53%		658	412	2.303
			Average		2.296

Table 5.1: Results of Archimedes density measurement of nano-silicon high-pressure samples. These data are from a single sample of nano-structured silicon approximately diameter 4.3 mm and height 2.6 mm.

5.5 Discussion

5.5.1 New Material Synthesis

High-pressure synthesis was hindered by difficulties in obtaining a monolithic material. Delamination along the furnace axis was persistent through many attempts to eliminate the feature, though progress was made. Several changes to the methodology were adopted to minimize delamination in our high-pressure synthesis results. These modifications were concerned with strain recovery within the furnace stack, control of the decompression rate and decompression temperature to assist in strain recovery within the sample, and exploration of systematic failures in the experiment design. Graphite plates were thickened to absorb some of the volume change in the furnace stack, while the bottom anvil was changed from MgO to CaF_2 to assist in the same purpose. Various decompression programs were tested to judge the impact of temperature and decompression rate on the final properties. Run logs for the press were scoured to discover trends that might reveal a systematic error in our experimental procedure. These efforts led to improvements over time, allowing the sample height to improve from under a millimeter to 6.5 mm for single monolithic pieces of sintered material.

Our model of stress-driven densification gives at least an approximate description of the necessary sintering times and the advantage relative to grain growth and chemical homogenization. Guided by this model, our candidate synthesis conditions yielded immediate results. The exercise also offers a simple explanation for the failure of conventional techniques to densify these materials without homogenization, for any

combination of time and temperature. These results demonstrate the suitability of the models selected, and allow us to choose new candidate process parameters with confidence.

Massive volume change during the densification of the green body takes our technique and methodology to the very limit. The separate but similar operation of the Getting-design cubic multi-anvil device (see Chapter 2), with the same observed uniaxial failure mode, confirms that the problem lies in the furnace stack. The bulk volume reduction of more than 50% is one possible source of mechanical failure on sample decompression. This volume reduction is typically accomplished by a 4% reduction in diameter and a 50% reduction in length of the cylindrical sample. Such anisotropic volume reduction results in significant spring-back and relaxation along one axis regardless of the loading state prior to pressure release. Efforts to re-powder and press these materials a second time were intended to improve the green body density sufficiently to reduce the volume and sample length reductions. We intend also to attempt immediate repressing without re-powdering the result of the first-stage synthesis.

Reducing the total sample volume should also reduce the strain that the rebounding furnace elements place on the sample during release and should minimize the temperatre gradient experienced by the sample, another possible source of delamination stresses. The furnace hot-spot is directly in the center of the sample pressure assembly. As one moves above or below the hot spot the temperature drops off, eventually reaching 15 °C at the water cooled top and bottom plates. This gradient is estimated to be at least 10 °C per

millimeter at 4 mm from the center and 50 °C per millimeter at 15 mm from the center. With a 15 mm long sample one cannot reliably say what the process temperature was during the experiment because the experiment was not conducted at one temperature. Similar modes of failure have been observed in other experiments conducted on the same press and similar methodology. In these cases mineral samples were enclosed in noble metal capsules within the pressure assembly. For experiments with overly long capsules, delamination of the contents and tearing of the capsule has been observed. Such failure is only observed if the capsule is greater than 4 mm in length. This may be due to the thermal gradient along the furnace. We intend to attempt to synthesize large samples over a region with smaller thermal gradient using the 0.75" piston cylinder assembly. This assembly has a maximum applied pressure of 2 GPa, which may result in a significantly lower sintering figure of merit for these experiments.

5.5.2 Application of the Sintering Figure of Merit

In order to generate candidate synthesis conditions one can refer to our sintering Figure of Merit plots to generate the values for any combination of pressure, temperature and time. For instance, in an effort to reduce the height of the sample in our piston cylinder experiments a larger piston diameter was considered. The larger 0.75" assembly cannot reach the pressures of the 0.5" assembly so our pressure variable was fixed at 2 GPa, the practical limit of the 0.75" device. Our candidate synthesis conditions worked well for synthesis of nano-structured silicon. Using conditions similar to the 3 GPa experiments at only 2 GPa would result in a figure of merit of about five, compared to 15 at 3 GPa. In order to improve the figure of merit at 2 GPa one must both decrease the temperature and

increase the time. The figure of merit can be improved to about 7.5 if the experiment is run at 800 °C for two months, or up to 10 if the experiment is run at 700 °C for twenty-five years. Clearly these candidate experiments begin to look impractical for industrial applications at 2 GPa. Our figure of merit calculation is just a tool used to ballpark, successfully, our initial experiments in this system and for this application. The selection of 10 or greater for our minimum requirement for the sintering figure of merit for our candidate synthesis criteria was arbitrary and great value could be obtained from discovering where on the scale from 0.1 to 10 the nanostructure is lost during sintering. An immediate reward from this knowledge would follow if the threshold were below 5. In this hypothetical case, experiments could then proceed just as swiftly at 2 GPa as they presently proceed at 3 GPa.

Alternatively, changing from nano-silicon to nano-germanium would greatly improve the figure of merit at any combination of time, temperature, and pressure. A sintering figure of merit of about 13 is obtained at 2 GPa, 600 °C, and 22 minutes – very comparable to that of the initial silicon experiments. The self-diffusion coefficient of germanium is much higher than that of silicon, thus greatly reducing the time required to sinter the material.

Our sintering figure of merit is a tool that provides a method of determining candidate synthesis conditions, while accounting for the known boundary conditions for materials synthesis. Due to the conservative assumptions of our sintering figure of merit, there may be significant flexibility on the minimum value required to produce chemically

heterogeneous and fully sintered nano-structured materials. One expects the behavior near the conditions where our figure of merit equals one to be the most informative on the quality of the model, though for this proof of concept a crude model has been sufficient.

5.6 Conclusions and Future Work

Our experimental evidence demonstrates the suitability of high-pressure synthesis towards not only controlling grain growth during sintering, but allowing the bulk synthesis of nano-grained solids. To the best of our knowledge this is a new application for hot-pressing. Most of the materials processing world considers our high-pressure technique an ultra-high-pressure technique and quite at the opposite end of the equipment spectrum from the thin film technology typically thought of with bulk nano-structures. Sample volumes are constrained by the practical concerns of the press available. Our present capabilities allow for a disk shaped sample 4 mm in height and 9 mm in diameter, with a mass of approximately 1 g of silicon or silicon-germanium powders. Synthesis runs are short, comparable with standard hot-pressing techniques, but with substantially more preliminary and post synthesis work required due to the destructive nature of the pressurization process. The pressure assembly used in this high-pressure technique is sacrificed during the experiment, while the pressure assembly used in standard hot pressing can be reused for many synthesis runs. Though this recurring operating cost exceeds that of standard techniques, the high-pressure technique provides a unique synthesis capability that cannot otherwise be duplicated.

Pure silicon, pure germanium, and composite (consisting of 50% mechanically mixed silicon-germanium with a 200 nm grain size and 50% nano-silicon with a 60 nm grain size) compounds have been synthesized. These materials were initially nanometer scale powder compacts and after processing were monolithic, dense, solids with nano-grained structures. These materials maintained their short range chemical heterogeneity and

reached a useful density for device applications. Final sample dimensions approached disks of 5.5 mm diameter and 6 mm height with an approximate mass of 0.6 g.

These techniques seem largely independent of peculiarities of constituent elemental chemistry. Pressure synthesis is a popular and common technique in both metals and ceramics processing. New structures for thermoelectric materials research can be explored through the use of high-pressure sintering. Powders containing fast diffusing species can now come to full density without resulting in long range chemical homogeneity common to standard techniques. This high-pressure technique will be limited to materials with similar thermal expansion coefficients and bulk modulus. Since this is a high-pressure technique with capability to reach reasonably high temperatures the resulting material will be subject to large internal strain if mismatched materials are selected. While the rates, pressures and temperatures for different materials might vary significantly, the technique should be applicable up to the limits of our experimental apparatus.

Materials produced via this technique should provide insight into fundamental materials behavior, as one composition can be produced at grain sizes down to the nano-scale. Bulk three-dimensional nano-structure behaviors have not been explored for materials that have previously only been prepared as nano-structured thin films. With easy access to these materials, trends in materials properties that depend on grain size, such as thermal conductivity, can be measured to greater extremes.

As a result of this work, spinodal-like microstructures can be synthesized in materials systems that do not spinodally decompose. Spinodal decomposition describes a phase separation where the difference in composition between the products is small but periodic throughout the structure [17]. This high-pressure technique can start with appropriately sized particles of the two compositions and sinter the powder compact without losing that chemical and structural diversity. Two-phase, small grain size, evenly distributed, materials can be synthesized even when chemical diffusion between the two phases is high and phase separation energetically unfavorable. Such structures could be the key to the long awaited phonon-glass electron-crystal thermoelectric material. Using standard synthesis techniques, attempts at this sort of construction, in systems where spinodal decomposition cannot be used directly, tend to result in homogenous solid solutions. In some pathological cases, or when the sintering temperature is much lower than the melting temperature, the second phase can pin the grain boundaries and pore structure of the first phase preventing densification entirely.

The immediate future holds improvements in sample volume, approaching the 4 mm square by 6 mm tall physical dimension required for device synthesis. Furthermore exploration of the sintering figure of merit parameters will be undertaken to determine how high the sintering figure of merit must be to produce the results we demand. Exploration near a sintering figure of merit of unity, where the mechanisms are predicted to work at similar rates, should shed more light onto behavior of materials under creep or high-pressure synthesis conditions. The longer term suggests expanding the work to include other materials systems, MoS_2 and skutterudites, and building actual silicon-

germanium devices using this process. There is much enthusiasm about synthesizing a wide variety of thermoelectric materials using this technique. Many theoretical two-phase systems suffer from inter-diffusion during traditional densification routes. Providing a quick and reliable means to prepare such systems in reality has opened many opportunities for future advanced thermoelectric materials research.

5.7 References

18 Venkatasubramanian, R., E. Siivola, et. al. (2001). "Thin-film thermoelectric devices with room-temperature figures of merit." Nature 413 (6856): 597-602.

77 Brinker, C.J. (2004). "Evaporation-Induced Sel-Assembly: Functional Nanostructures Made Easy." *MRS Bulletin* 29(9).

35 Caillat, T., J.P. Fleurial, et al. (1999) "A New High Efficiency Segmented Thermoelectric Unicouple." *34th Intersociety Energy Conversion Engineering Conference* IECE (IECE99CD):2567.

78 Ursell, T.S. and G.J. Snyder (2002). "Compatibility of Segmented Thermoelectric Generators." *ICT Conference Proceedings.*

79 Kim, K.H., M. Uehara, et al. (2000) "Thermal and Electrical Transport Properties and Two-Phase Mixtures in La5/8-xPrxCa3/8MnO3" *Physical Review Letters* 84(13):2961-2964.

80 Murray, P., D.T. Livey, et al. (1958) Hot Pressing of Ceramics, Ceramic Fabrication Processes. W. D. Kingery Ed., Boston, Technology Press of Massachusetts Institute of Technology and John Wiley & Sons: 147-171.

81 Wilkinson, D.S., and M.F. Ashby (1976). Sintering and Catalysis. New York. Plenum.

82 Andrault, D., R.J. Angel, et al, (2003), "Equation of state of stishovite to lower mantle pressures." *American Mineralogist*, 88(2-3): 301-307.

83 Reed, J.S. (1995) Solid State Sintering, Principles of Ceramics Processing 2nd ed. John Wiley & Sons New York 1995: 594-618.

84 Wachtman, J.B., (1996) Creep in ceramics. Mechanical Properties of Ceramics John Wiley & Sons, New York: 311-316.

85 Nabarro, F.R. (1947). Deformation of Crystals by Motion of Single Ions. *Report of a Conference on the Strength of Solids.* Bristol, University of Bristol: 75-90.

86 Herring, C. (1950). Diffusional Viscosity of Polycrystalline Solids. *J. Appl. Phys.*, 21(5): 437-445.

87 Coble, R.L. (1961). Sintering of Crystalline Solids. Intermediate and Final State Diffusion Models. *J. Appl. Phys.*, 32(5)787-792.

88 Wilkinson, D.S., (1975). Pressure Sintering by Power Law Creep. *Acta Metallurgica.* 23(11):1277-1285.

89 Ashby, M.F., R.A. Verral (1973). "Diffusion-Accomodated flow and superplasticity." *Acta Metallurgica* 21(2): 149-163.

90 Urick, P., and M.R. Notis (1973). "Final Stage Densification During Pressure Sintering of CoO." *J. Am. Ceram Soc.* 56(11): 570-574.

91 Notis, M.R. (1977). "Advances in Ceramic Hot Forming and Pressing: Theory and Practice." *Ceramurgia Int.* 3.

92 Ashby, M.F. (1972). "A First Report on Deformation Mechanism Maps." *Acta Metalurgical.* 20(7): 887-896.

93 Poirier, J.P. (1991). "Introduction to the Physics of the Earth's Interior." Cambridge, Cambridge University Press.

94 Bracht, H., E.E. Haller, et al. (1998). "Silicon self-diffusion in isotopic heterostructures." *Physical Review Letters.* 81(2): 393.

95 Mitchell, M.J., P. Ashburn, et al. (2002). "Germanium diffusion in polycrystalline emitters of SiGe hererojunction bipolar transistors fabricated by germanium implantation." *Journal of Applied Physics*. 92(11): 6924-6926.

96 Gozza, G.E., (1991). Pressure Densification. Ceramics and Glasses, ASM Int. 4: 296-303.

97 Bohlen, S.R. (1984). "Equilibria for precise pressure calibration and a frictionless furnace assembly for the piston-cylinder apparatus." *Neues Jahrb. Minearl., Monatsh* (9): 404-412.

98 Dunn, T. (1993). The Piston-Cylinder Apparatus. 3: 38-89.

99 Luth, R.W. (1993). Measurement and control of intensive parameters in experiments at high pressure in solid-media apparatus. 2: 14-37.

100 Boyd, F.R., and J. L. England. (1960). "Apparatus for phase-equillibrium measurements at pressures up to 50 kilobars and temperatures up to 1750C." *J. Geophys. Red.* 65(2): 741-748.

49 Mosenfelder, J.L. and S.R. Bohlen (1997). "Kinetics of the coesite to quartz transformation." *Earth and Planetary Science Letters* 153(1-2): 133-147.

101 Tingle, T.N. (1988). "Retrieval of uncracked single crystals from high pressure in piston-cylinder apparatus." *Am. Minaral.* 73(9-10): 1195-1197.

102 Farver, J.R., and R.A. Yund (1995). "Grain boundary diffusion of oxygen, potassium and calcium in natural and hot-pressed feldspar aggregates." *Contrib. Mineral. Petrol.* 118(4): 340-355.

103 El-Genk, M.S., H.H. Saber, et al. (2002). "A Performance comparison of SiGe and skutterudite based segmented thermoelectric devices." *AIP conference proceedings* 608(1): 1007-1015.

17 Kingery, W.D., H.K. Bowen, et al. (1976). Introduction to Ceramics. Cambridge, Mass., John Wiley & Sons.

A.1 Appendix 1
Chapter 3: $Ce_xCo_4Sb_{12}$

Sample Name	Composition	Temp [C]	Pressure [GPa]	Dates	Seebeck $[\mu V/K]_{300}$	Theo. Density
GDS1-0	$CoSb_3$	300-600	0.7 - 3.4	1/23/01 +	Mixed	7.62
GDS1-2	$GeCo_4Sb_{12}$	300-600	0.7 - 3.4	2/1/01 - 2/20/01	N Type	
GDS1-3	$SnCo_4Sb_{12}$	300-600	0.7 - 3.4	2/2/01 - 9/10/01	P Type	7.98
GDS1-4	$Sn_{0.5}Co_4Sb_{12}$	300-600	0.7	3/7/01 - 3/11/01	P Type	7.98
GDS1-5	$Yb_{1.0}Co_4Sb_{12}$	300-600	0.7	8/17/01 - 8/20/01	Mixed	
GDS1-6	$Ce_{1.0}Co_4Sb_{12}$	300-600	3.4	9/12/2001 +		
GDS1-7	$Ce_{0.10+0.05}Co_4Sb_{12}$	550-650	0.5-8	10/2/01 - 10/17/01		
GDS1-8	$Ce_{0.15}Co_4Sb_{12}$	25-650	0.5-14	10/3/01 +		
GDS1-9	$Ce_{0.25}Co_4Sb_{12}$			12/20/01 +		
GDS1-10	$Ce_{0.2}Co_4Sb_{12}$			3/11/02 - 3/18/02		
GDS1-11	$Ce_{0.18}Co_4Sb_{12}$			6/29/2002		
GDS1-12	$Ce_{0.5}Co_4Sb_{12}$			6/12/02 +		
GDS1-13	$Ce_{0.3}Co_4Sb_{12}$			4/1/2003 +		

Sample Name	Composition	Iteration	Temp [C]	Pressure [GPa]	Date	MP	Seebeck $[\mu V/K]_{300}$	Density $[g/cm^3]$	Theo. Density	% Theo. Density
GDS1-0	$CoSb_3$	1	600	0.7					7.62	0.000
		2	500	0.7	1/23/2001	x			7.62	0.000
		3	400	0.7	1/31/2001	x	-112	6.94	7.62	0.911
		4	300	0.7	2/5/2001	x	-95	6.13	7.62	0.804
		5	600	3.1					7.62	0.000
		6	500	3.1	1/25/2001	x	109		7.62	0.000
		7	400	3.1					7.62	0.000
		8	300	3.1	1/28/2001	x	48		7.62	0.000
		9	500	0.7	1/30/2001	x	-23.5	6.77	7.62	0.888
		10	600	0.7	4/3/2001		-14	7.38	7.62	0.969
		11	600	0.7	5/8/2001	x	130	7.52	7.62	0.987
		12	N/A	N/A	8/8/2001	x				
	ww187	13	100	6	4/7/2002	x				
	ww195	14	100	6	5/3/2002	x	-321			

Sample Name	Composition	Iteration	Temp [C]	Pressure [GPa]	Date	MP	Seebeck $[\mu V/K]_{300}$	Density $[g/cm^3]$	Theo. Density	% Theo. Density
GDS1-2	$GeCo_4Sb_{12}$	1	500	0.7	2/1/2001	x	-86	6.7		
		2	500	3.1						
		3	400	0.7	2/15/2001	x	-65	6.09		
		4	300	0.7	2/20/2001		-87.5	5.81		

Sample Name	Composition	Iteration	Temp [C]	Pressure [GPa]	Date	MP	Seebeck $[\mu V/K]_{300}$	Density $[g/cm^3]$	Theo. Density	% Theo. Density
GDS1-3	$SnCo_4Sb_{12}$	1	500	0.7	2/2/2001	x	32	7.45	7.98	
		2	500	3.1						

3	400	0.7	2/16/2001	x	30.5	7.32	8.04	
4	300	0.7	2/21/2001	x	-37.4	6.28		
5	400	0.7	3/15/2001	o	22	7.21		
6	500	0.7	3/15/2001	o	28	7.5		
7	600	0.7	3/15/2001	o	17	7.12		
8	550	0.7	7/18/2001	x	42.8			
9	500	0.7	7/19/2001	o				
10	600	0.7	7/23/2001					
11	600	0.7	5/10/2001	x	20	7.368		
12	500	0.7	5/10/2001	x	36	7.34		
13	450	0.7	7/27/2001	o				
14	600	0.7	7/30/2001	x				
15	600	3.4	9/8/2001	x	-63	7.26		
16	600	3.4	9/7/2001	x	-54			
17	600	12	9/23/2001	x				
18	550	8	12/6/2001	o	-51			

Sample Name	Composition	Iteration	Temp [C]	Pressure [GPa]	Date	MP	Seebeck $[\mu V/K]_{300}$	Density $[g/cm^3]$	Theo. Density	% Theo. Density
GDS1-4	$Sn_{0.5}Co_4Sb_{12}$	1	400	0.7	3/7/2001	x	27	7.09	7.98	0.888
		2	500	0.7	3/8/2001	x	31	7.53	7.98	0.944
		3	600	0.7	3/11/2001	x	-25	7.35	7.98	0.921
		4	450	0.7	8/10/2001	x	38	7.85	7.98	0.984
	$Sn_{0.3}Co_4Sb_{12}$	5	550	3.5	11/12/2001	o	-91	7.3	7.84	0.931

Sample Name	Composition	Iteration	Temp [C]	Pressure [GPa]	Date	MP	Seebeck $[\mu V/K]_{300}$	Density $[g/cm^3]$	Theo. Density	% Theo. Density
GDS1-5	$YbCo_4Sb_{12}$	1	600	0.7	8/17/2001	x	-61	7.72		
		2	500	0.7	8/20/2001	x	92	7.4		
DM310	Yb0.25Co4Sb12	1	450	6	8/30/2002		-182			
GDS1-6	$CeCo_4Sb_{12}$	1	600	12	9/12/2001	x				
		2	100	6	4/17/2002	x				
		ref	600	0.1	4/17/2002	x	-17			
	ww191	3	100	6	4/18/2002	x				
	ww226	4	450	6	7/5/2002		-57			

Sample Name	Composition	Iteration	Temp [C]	Pressure [GPa]	Date	MP	Seebeck $[\mu V/K]_{300}$	Density $[g/cm^3]$	Theo. Density	% Theo. Density
GDS1-7	$Ce_{0.10+5}Co_4Sb_{12}$	1	550	8	10/2/2001	x	-31	7.18		
		Ref	650	0.5	10/17/2001	x	-76	7.23		
	$Ce_{0.10}Co_4Sb_{12}$	Raw	N/A	N/A	N/A	x				

Sample Name	Composition	Iteration	Temp [C]	Pressure [GPa]	Date	MP	Seebeck $[\mu V/K]_{300}$	Density $[g/cm^3]$	Theo. Density	% Theo. Density
GDS1-8	$Ce_{0.15}Co_4Sb_{12}$	1	550	8	10/3/2001	x	-95	7.54		
	ww158	2	450	8	10/9/2001	x	-37	7.81		

ww159		3	350*	8	10/10/2001	x	-113	7.35		
ww160		4	350	8	10/15/2001	x	-28	7.67		
ww161		5	550	8	10/16/2001	x	-30			
ww162		6	550	5	10/23/2001	x	21			
		Ref	650	0.5	10/18/2001	x	-124	7.98		
ww163		7	25	8.5	10/28/2001	x	-118			
ww164		8	450	5	10/30/2001	x	-187			
		Raw	N/A	N/A	N/A	x	-	-	-	-
ww166		9	100	14	11/16/2001	x	-124	7.42		
		10	100	14	1/2/2002		-117	6.43		
		11	100	14	1/10/2002		-115	9.1?!		
		12	100	6	1/16/2002		-134	5.5		

Sample Name	Composition	Iteration	Temp [C]	Pressure [GPa]	Date	MP	Seebeck $[\mu V/K]_{300}$	Density $[g/cm^3]$	Theo. Density	% Theo. Density
GDS1-9	$Ce_{0.25}Co_4Sb_{12}$	ref	700	0.1	3/8/2002	x	-131	7.36		
		1	100	6	3/12/2002	x	-127			
		2	100	6	3/22/2002	x	-119	7.28		
		3	100	14	4/10/2002	x				
	ww201	4	525	6	5/14/2002	x	-139			
	ww202	5	600	6	5/15/2002	x	-140			
	ww204	6	425	6	5/20/2002	x	-109			
	ww206	7	600	14	5/24/2002					
	ww216	8	600	6	6/16/2002		-140			
	ww218	9	450	6	6/18/2002	x	-160			

Sample Name	Composition	Iteration	Temp [C]	Pressure [GPa]	Date	MP	Seebeck $[\mu V/K]_{300}$	Density $[g/cm^3]$	Theo. Density	% Theo. Density
GDS1-10	Ce0.2Co4Sb12	ref	650	0.1	3/11/2002	x	88.5	7.36	7.8	0.944
		1	100	6	3/18/2002					

Sample Name	Composition	Iteration	Temp [C]	Pressure [GPa]	Date	MP	Seebeck $[\mu V/K]_{300}$	Density $[g/cm^3]$	Theo. Density	% Theo. Density
GDS1-11	Ce0.18Co4Sb12	1	450	6	6/29/2002		158	7.21	7.727	0.933

Series closed after one failure.
Conclusion:
Cerium powder added to the top will not yield a filled material.

Sample Name	Composition	Iteration	Temp [C]	Pressure [GPa]	Date	MP	Seebeck $[\mu V/K]_{300}$	Density $[g/cm^3]$	Theo. Density	% Theo. Density
GDS1-12	Ce0.5Co4Sb12	Ref	650	0.1	6/12/2002	x	-93	6.6	8.136	0.811
	ww229	1	450	6	7/12/2002	x	-114	7.7	8.136	0.946
	ww230	2	600	6	7/15/2002	x	-84	7.79	8.136	0.957

	ww240	3	450	6	8/6/2002	
	ww241	4	450	6	8/8/2002	-128
	ww242	5	540	6	8/10/2002	-134
	ww243	6	450	6	8/12/2002	-145

Sample Name	Composition	Iteration	Temp [C]	Pressure [GPa]	Date	MP	Seebeck $[\mu V/K]_{300}$
GDS1-13	Ce0.3Co4Sb12	ref	650	0.1	6/6/2003	x	-182

GDS1-0.011				
	Sb	Co	Sn	Total
point 28	74.1	25.9	0	100
point 29	74.1	25.9	0	100
Average	74.1	25.9	0	100
stoichiometry	11.856	4.144	0.000	6.25
normalized	11.444	4.000	0.000	0.965250965
GDS1-3.011				
	Sb	Co	Sn	Total
Point 30	73.5	25.5	1	100
Point 31	72.8	25.3	1.9	100
Point 39	72.8	25.4	1.8	100
Average	73.033	25.400	1.567	100.000
stoichiometry	12.416	4.318	0.266	5.882
normalized	11.501	4.000	0.247	0.926
GDS1-3.012				
	Sb	Co	Sn	Total
Point 33	72.3	25.1	2.7	100.1
Point 34	72.6	25.4	2	100
Point 35	72.1	25.2	2.7	100
Average	72.333	25.233	2.467	100.033
stoichiometry	12.293	4.288	0.419	5.884
normalized	11.466	4.000	0.391	0.933
GDS1-4.001				
	Sb	Co	Sn	Total
Point 36	73.7	25.7	0.6	100
Point 37	72.9	25.6	1.6	100.1
Point 38	73.3	25.4	1.3	100
Average	73.300	25.567	1.167	100.033
stoichiometry	12.090	4.217	0.192	6.063
normalized	11.468	4.000	0.183	0.949
GDS1-0.012				
	Sb	Co	Sn	Total
Point 43	75.1	24.5	0	99.6
Point 44	75.1	24.6	0	99.7
Average	75.100	24.550	0.000	99.650
stoichiometry	12.812	4.188	0.000	5.862
normalized	12.236	4.000	0.000	0.955

GDS1-3.014				
	Sb	Co	Sn	Total
Point 38	73.6	24.5	2	100.1
Average	73.6	24.5	2	100.1
stoichiometry	12.500	4.161	0.340	5.888235294
normalized	12.016	4.000	0.327	0.961344538
GDS1-4.002				
	Sb	Co	Sn	Total
Point 39	74.2	24.8	1	100
Average	74.200	24.800	1.000	100.000
stoichiometry	12.614	4.216	0.170	5.882
normalized	11.968	4.000	0.161	0.949
GDS1-4.003				
	Sb	Co	Sn	Total
Point 40	74.7	24.9	0.4	100
Point 41	74.9	24.8	0.4	100.1
Average	74.800	24.850	0.400	100.050
stoichiometry	12.710	4.222	0.068	5.885
normalized	12.040	4.000	0.064	0.947
GDS1-4.004				
	Sb	Co	Sn	Total
Point 42	73.6	24.4	1.9	99.9
Average	73.600	24.400	1.900	99.900
stoichiometry	12.525	4.152	0.323	5.876
normalized	12.066	4.000	0.311	0.963
GDS1-3.008				
	Sb	Co	Sn	Total
Point 43	73.8	24.3	1.9	100
Point 44	73.6	24.6	1.9	100.1
Average	73.700	24.450	1.900	100.050
stoichiometry	12.523	4.154	0.323	5.885
normalized	12.057	4.000	0.311	0.963
GDS1-8.001				
	Sb	Co	Ce	Total
Point 22	75	24.5	0.5	100
Average	75.000	24.500	0.500	100.000
stoichiometry	12.750	4.165	0.085	5.882
normalized	12.245	4.000	0.082	0.960

GDS1-3.004				
	Sb	Co	Sn	Total
Point 41	74.8	24.8	0.4	100
Point 42	74.1	25.5	0.3	99.9
Average	74.450	25.150	0.350	99.950
stoichiometry	12.663	4.278	0.060	5.879
normalized	11.841	4.000	0.056	0.935
GDS1-3.017				
	Sb	Co	Sn	Total
Point 40	71.8	25.9	2.2	99.9
Point 41	73.6	22.7	3.7	100
Point 42	69.6	0.1	30.3	100
Average	72.700	24.300	2.950	99.950
stoichiometry	12.365	4.133	0.502	5.879
normalized	11.967	4.000	0.486	0.968
GDS1-3.016				
	Sb	Co	Sn	Total
Point 38	69.2	23.1	7.7	100
Point 39	69.2	23.5	7.3	100
Average	69.200	23.300	7.500	100.000
stoichiometry	11.764	3.961	1.275	5.882
normalized	11.880	4.000	1.288	1.010
GDS1-3.015				
	Sb	Co	Sn	Total
Point 38	70.3	22	7.7	100
Average	70.300	22.000	7.700	100.000
stoichiometry	11.951	3.740	1.309	5.882
normalized	12.782	4.000	1.400	1.070
GDS1-6.001				
	Sb	Co	Ce	Total
Point 28	67.7	32.3	0.1	100.1
Average	67.700	32.300	0.100	100.100
stoichiometry	11.498	5.486	0.017	5.888
normalized	8.384	4.000	0.012	0.729
GDS1-7.001				
	Sb	Co	Ce	Total
Point 24	75.2	24.4	0.4	100
Average	75.200	24.400	0.400	100.000
stoichiometry	12.784	4.148	0.068	5.882
normalized	12.328	4.000	0.066	0.964

A.2 Appendix 2
Chapter 4: $Ce(Ru_{0.67}Rh_{0.33})_4Sb_{12}$

Sample Name	Composition	Iteration	Temp [C]	Pressure [GPa]	Date	MP	Comments	Seebeck $[\mu V/K]_{300}$	Density $[g/cm^3]$
DGF28-0	$Ce_{0.7}Ru_3RhSb_{12}$	1	600	0.7	1/19/2001		Die Failure, TZM plunger		
		2	500	0.7					
DGF28-1	$Ce_{0.7}Ru_3RhSb_{12}$	1	600	3.1	10/17/2000	x	Polyphase		
		2	300	8	11/27/2001	o	r=3.227, mob=4.25, cc=4.557E+20	25	
DGF28-2	$Ce_{0.7}Ge_{0.22}Ru_3RhSb_{12}$	1	900	3.1	1/10/2001	x	Polyphase	10	7.95
DGF28-3	$Ce_{0.7}Sn_{0.45}Ru_3RhSb_{12}$	1	600	3.1	11/7/2001	x	Polyphase		
		2	400	0.7	3/15/2001			12	6.87
		3	500	0.7	3/15/2001			15	7.33
DGF36-0	$La_{0.7}Ru_3RhSb_{12}$	1	600	0.7					
		2	500	0.7					
DGF36-1	$La_{0.7}Ru_3RhSb_{12}$	1	600	3.1					
DGF36-2	$La_{0.7}Ge_{0.22}Ru_3RhSb_{12}$	1	900	3.1					
DGF36-3	$La_{0.7}Sn_{0.45}Ru_3RhSb_{12}$	1	600	3.1					
		2	400	0.7					
		3	500	0.7					
DGF28-4	$Ce_1Ru_{2.67}Rh_{1.33}Sb_{12}$	1	100	6	3/31/2002	x		15	7.32
		2	600	6	4/18/2002	x	Ce0.87Ru2.7Rh1.3Sb11.7		
		ref	650	0.1	4/17/2001	x	Ce0.71Ru2Rh2Sb12 Ce1Ru3RhSb12 Ce1.32Ru0.4Rh3.6Sb12	7	
		3	600	6	6/12/2002				
	ww215	4	600?	6	6/14/2002	x		27.6	
	ww250	5	350	6	9/6/2002	x	temp too low for homogination	18	
	ww252	6	600	6/3	9/20/2002	x	Ce1.04(RuRh)4Sb12; press failure reduced pressure to 3GPA during dwell	40	
	ww259	7	600/350	6	10/28/2002	x	Ce0.94(RuRh)4Sb12; r=4.15, mob=60.6, cc=2.5E19; RuRh ratio variable through matrix	80	

Sample Name	Composition	Iteration	Temp [C]	Pressure [GPa]	Date	MP	Comments	Seebeck $[\mu V/K]_{300}$	Density $[g/cm^3]$
GS3-1	Ce0.15Ir4Sb12	Ref	650	0.1	7/22/2002	x	Ce0.02-0.06Ir4Sb12,	86	6.99
	ww232	1	450	6	7/19/2002	x	Ce0.02-0.19Ir4Sb12, r = 25.417, mob = 62.24, cc = 3.951E+18	87	9.2
	ww237	2	600	6	7/29/2002			107	
	ww238	3	600	6	7/31/2002			88	
	ww249	4	600	6	9/3/2002			57	
	ww251	5	750	6	9/11/2002			54	

Sample Name	Composition	Iteration	Temp [C]	Pressure [GPa]	Date	MP	Comments	Seebeck $[\mu V/K]_{300}$
GS3-2	Ce0.3Ir4Sb12	Ref	650	0.1				

	ww262	1	800/650	6	11/7/2002			57
	ww264	2	800/650	6	11/11/2002		blowout poor sample quality	N/A
	ww265	3	800/500	6	11/12/2002		blowout poor sample quality	N/A
	ww269	4	800/600	6	12/2/2002		MgO plug, no sample (-552 Seebeck)	N/A
	ww270	5	800/600	6	12/9/2002			52
	ww275	6	800/600	6	1/10/2003			26
QM	ww280	7	600	6	4/30/2003		blowout poor sample quality	
	ww282	8	rt	6	5/4/2003	x	Ce0.06Ir4Sb12.79	-78
	ww285	9	600	6	5/9/2003	x	Ce0.17Ir4Sb12.61	28
	JPL Ref	10	650	0.1	5/6/2003	x	Ce0.03Ir4Sb12.55	-210
	ww286	11	200	6	5/14/2003	x	Ce0.13Ir4Sb12.79	-7

Sample Name	Composition	Iteration	Temp [C]	Pressure [GPa]	Date	MP	Comments	Seebeck $[\mu V/K]_{300}$	Density $[g/cm^3]$
GS4-1	$Ce(Ru_{2.44}Rh_{1.22}Pd_{0.34})(Sb_{11.66}Te_{0.34})$	Ref	650	0.1					

A.3 Appendix 3
Chapter 5: Nano-Si, Ge, SiGe

Overview of Preliminary SiGe nanostructure work.

The Nabarro-Herring Model of Creep was used to describe the flow during sintering. The materials constant required for this model is the self diffusion constant, a known quantity for silicon and germanium. We're taking one characteristic length in our calculation and comparing the time it takes each flow mechanism to reach that flow. Diffusion flow is a factor of grain size and self diffusion constant, since we're ignoring bulk diffusion and concentrating on grain boundary diffusion, a reasonable assumption with nano-particles and our desire to maintain a nano scale structure (not much bulk to speak of in comparason to grain boundary volume). The pressure induced sintering is not as simple as the diffusive case, and shows a strong pressure dependance at our synthesis pressures. The linear regime holds only when $\sigma V << kT$, since kT varies from 0.32 at 100C to 0.14 at 1400C our pressure cannot exceed10^3 or 10^4 Pascals for the approximation to have any hope of holding, since even the JPL press reaches 10^7 Pascals we must use the non-linear relation. This works to our advantage as the hyperbolic sin term accelerates the sintering rate with respect to the diffusion rate and we greatly improve our figure of merit. Our figure of merit is just the ratio of the diffusion time to the sintering time, where we've decided that a figure of merit of 10 is good for our purposes (the sintering rate is ten times as fast as the diffusion rate, meaning we can expect pressure induced sintering to dominate the compaction behavior). The figure of merit also tells us that at no combination of temperature and time will the standard sintering conditions in the JPL press will the compaction maintain chemical diversity while reaching a dense material. The JPL conditions are well below one, meaning chemical diffusion is much faster than pressure induced sintering and the resulting material will be chemically homogenous with signifigant grain growth as a result of the sintering process. By contrast the pressures attainable in the Caltech presses can reach a figure of merit in excess of 10.

A comfort zone can be mapped into our plots of Figure of Merit vs. Sintering Time. This shows us where our targets are for materials synthesis as predicted by our calculations. Taking reasonable synthesis times of 15 minutes to 3 days we see that for Silicon we have a variety of temperatures and pressures under which we expect to attain a fully dense sample with nano scale structure intact. For germanium we likewise have a large range in T, P, and time for a sucessful synthesis. Our first experiment on nanoscale silicon has confirmed that our theory is at least in the ballpark, resulting in a fully dense sample with a grainsize on the order of 50 nanometers.

References: 1st for Nabarro-Herring Creep, next three for Multianvil and High Pressure experimental methods

"Introduction to the Physics of the Earth's Interrior," Jean Paul Poirier, Cambridge [England] ; New York : Cambridge University Press, 1991

"Lubrication, gasketing, and precision in multianvil devices," David Walker, American Mineralogist, Vol 76, pg1092-1100, 1991

"Garnet-Perovskite transformation in CaGeO3 In-Situ X-ray measurements using synchrotron radiation," J. Susaki, M. Akaogi, S. Akimoto, O. Shimomura, Geophysical Research Letters, Vol 12, No. 10, pg729-732, October 1985.

"Some simplifications to multianvil devices for high pressure experiments," D. Walker, M.A. Carpenter, C.M. Hitch, American Mineralogist, Vol 75, pg1020-1028, 1990

Plot #1 Linear Model

Pressure improves figure of merit
JPL Synthesis is dominated by diffusion Sintering
14GPa reaches into the >10 figure of merit we're looking for
Large volume experiments have not so great figures of merit

Plot #2 Non-linear Model

Figure of Merit strongly pressure dependant (because of t|sinter)
JPL synthesis still hopeless for preserving nanostructure
Large volume synthesis at Caltech viable

Plot #3 Non-Linear Silicon

3GPa line showing highest volume, safest pressure experiment added
Very large comfort zone, we needn't reach even 3GPa nor particularly high temperatures

Plot #4 Non-Linear Germanium

3GPa line showing highest volume, safest pressure experiment added
Very large comfort zone, we needn't reach even 3GPa nor particularly high temperatures

The current target conditions for further experiments at Caltech:

Silicon requires conditions of 1000C, 3GPa, and 14 minutes
Germanium requires conditions of 675C, 3GPa, and 14 minutes

First Experiment Results

From EDS we see a pure silicon sample.
From EBSD we observe kikuchi patterns that vary on a length scale of 50nm.
This indicates a crystalline result with grain size on the order 50nm.
From SEM we observe a void free silicon surface, appearing fully dense.
From an archimedes density measurement we observe a density of 2.324 g/cm^3
99.8% density over 3 trials with a +-5%
Samples were very small and broke along decompression cracks
Proof of concept: Achieved.

First Experiment Failures

Sample size was about 50mg, handling the nanoparticles was awkward and green packing density was poor
SEM polish only down to 0.3 microns, by hand.
Mechanical polishing to a finer surface will be required to automatically resolve the kikuchi map with EBSD.

N_{AVO}	6.02E+23 1/mol	
d	1.00E-08 meters	
V	1.20E-05 m^3/mol	12
σ	Stress (Pa) Variable	
T	Temp (K) Variable	
k	8.6174E-05 eV/K	1.38E-23 J / mol K

2.97E+03

Stress		1.50E+08 Pa			
Temp (C)	Temp (K)	D_{sd} Si	Diffusion Time	Sintering Time	0.15GPa
100	373	3.51E-66	2.85E+49	4.91E+49	5.80E-01
200	473	1.30E-52	7.69E+35	1.68E+36	4.58E-01
300	573	8.84E-44	1.13E+27	2.99E+27	3.78E-01
400	673	1.43E-37	7.01E+20	2.18E+21	3.22E-01
500	773	5.70E-33	1.76E+16	6.27E+16	2.80E-01
600	873	2.01E-29	4.98E+12	2.01E+13	2.48E-01
700	973	1.32E-26	7.56E+09	3.40E+10	2.22E-01
800	1073	2.60E-24	3.85E+07	1.91E+08	2.02E-01
900	1173	2.07E-22	4.83E+05	2.62E+06	1.85E-01
		8.30E-21	1.20E+04	7.08E+04	1.70E-01
		1.94E-19	5.14E+02	3.26E+03	1.58E-01
		2.97E-18	3.37E+01	2.29E+02	1.47E-01
		3.20E-17	3.12E+00	2.27E+01	1.38E-01
		2.60E-16	3.84E-01	2.97E+00	1.29E-01

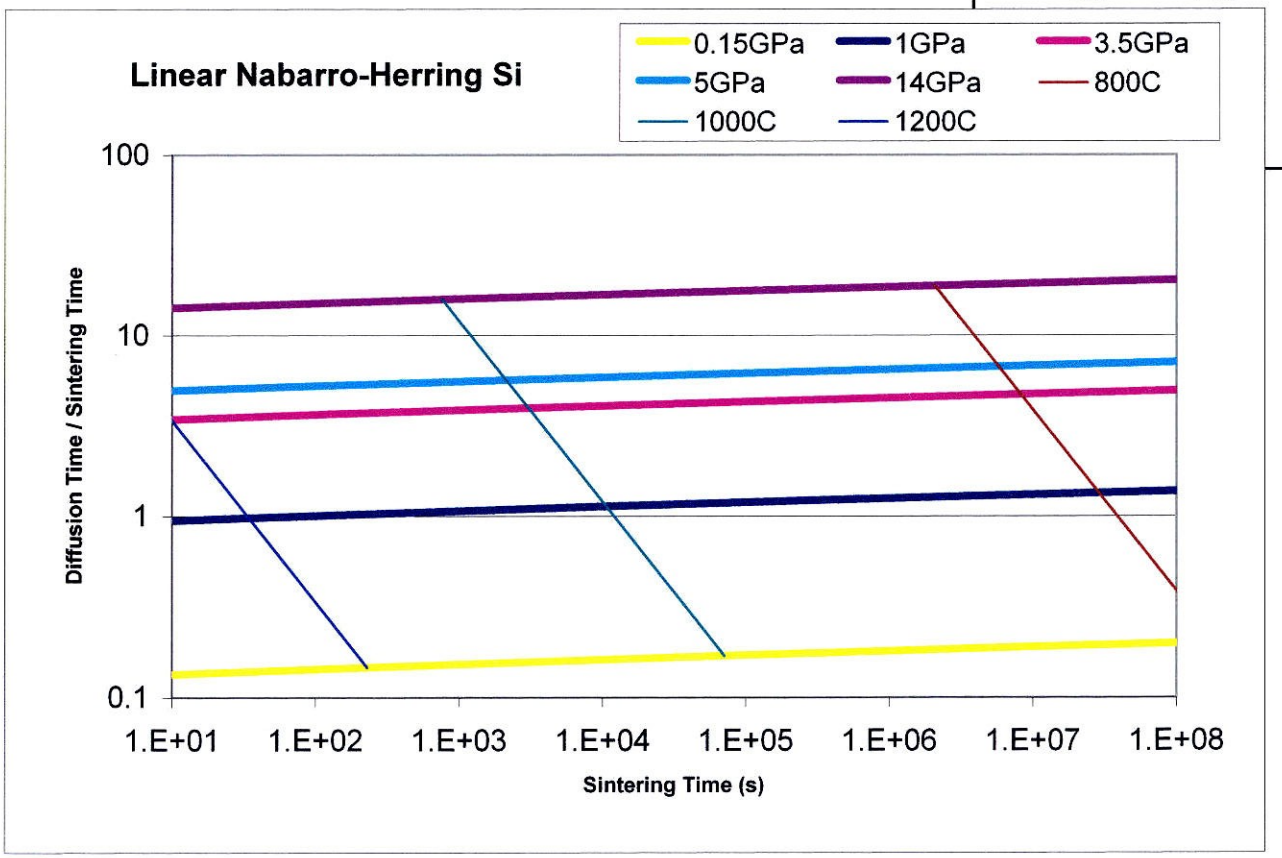

kT	σV
0.032143	1.80E+03
0.04076	
0.049378	
0.057995	
0.066613	
0.07523	
0.083847	
0.092465	
0.101082	
0.1097	
0.118317	
0.126934	
0.135552	
0.144169	

5/18/2004

N_{AVO}	6.02E+23 1/mol	
d	1.00E-08 meters	
V	1.20E-05 m^3/mol	12
σ	Stress (Pa) Variable	
T	Temp (K) Variable	
k	8.6174E-05 eV / K	1.38E-23 J / mol K

D=7.8exp(-2.970/RT) cm^2/sec

Stress		1.50E+08 Pa			
Temp (C)	Temp (K)	D_{Ge} Ge	Diffusion Time	Sintering Time	0.15GPa
100	373	5.80E-44	1.72E+27	2.97E+27	5.80E-01
200	473	1.77E-35	5.66E+18	1.24E+19	4.58E-01
300	573	5.89E-30	1.70E+13	4.50E+13	3.78E-01
400	673	4.48E-26	2.23E+09	6.94E+09	3.22E-01
500	773	3.38E-23	2.96E+06	1.06E+07	2.80E-01
600	873	5.58E-21	1.79E+04	7.23E+04	2.48E-01
700	973	3.23E-19	3.10E+02	1.39E+03	2.22E-01
800	1073	8.76E-18	1.14E+01	5.66E+01	2.02E-01
900	1173	1.35E-16	7.39E-01	4.00E+00	1.85E-01
1000	1273	1.36E-15	7.34E-02	4.32E-01	1.70E-01
1100	1373	9.78E-15	1.02E-02	6.48E-02	1.58E-01
1200	1473	5.38E-14	1.86E-03	1.27E-02	1.47E-01
	573	2.38E-13	4.20E-04	3.05E-03	1.38E-01
	673	8.82E-13	1.13E-04	8.77E-04	1.29E-01

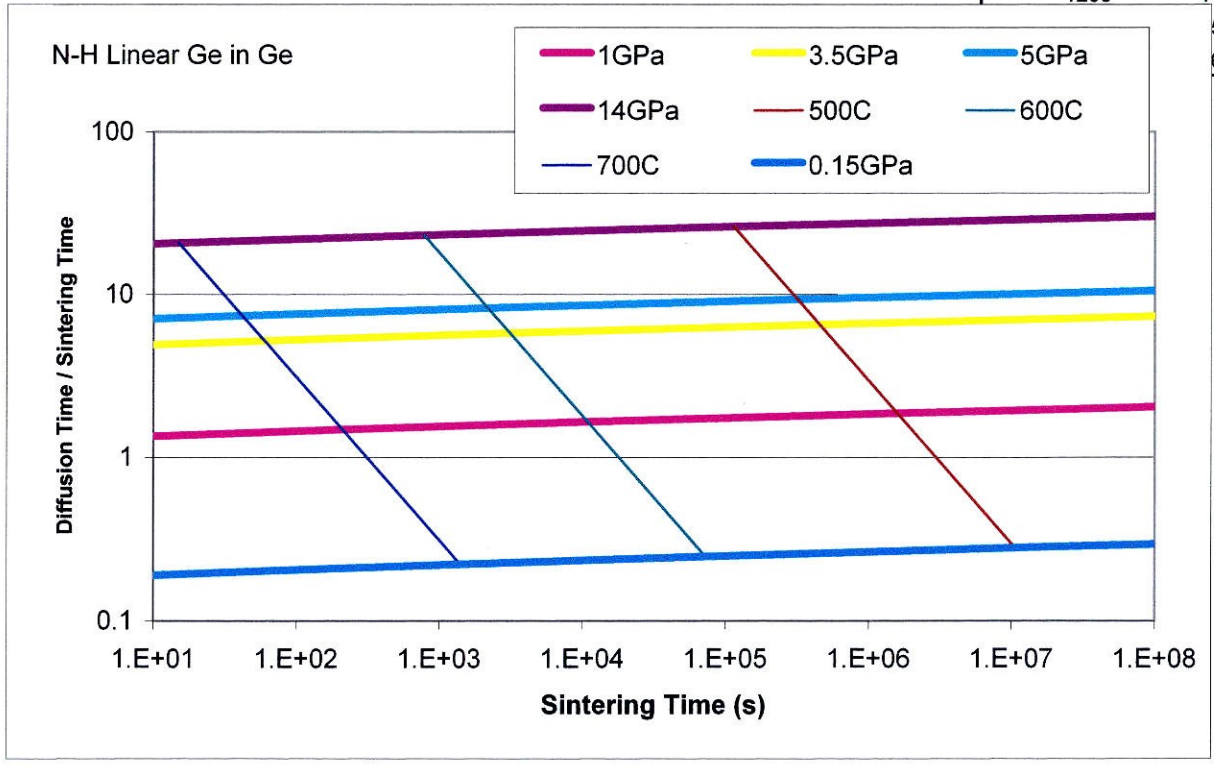

5/18/2004

N_{AVO}	6.02E+23 1/mol	
d	1.00E-08 meters	
V	1.20E-05 m^3/mol	12
σ	Stress (Pa) Variable	
T	Temp (K) Variable	
k	8.6174E-05 eV/K	1.38E-23 J / mol K

D=0.026*exp(-2.59/RT) cm^2/sec

Stress 1.50E+08 Pa

Temp (C)	Temp (K)	D_{Ge} Si	Diffusion Time	Sintering Time	0.15GPa
100	373	2.63E-41	3.80E+24	6.54E+24	5.80E-01
200	473	6.59E-34	1.52E+17	3.31E+17	4.58E-01
300	573	4.32E-29	2.32E+12	6.13E+12	3.78E-01
400	673	1.05E-25	9.55E+08	2.97E+09	3.22E-01
500	773	3.38E-23	2.96E+06	1.06E+07	2.80E-01
600	873	2.91E-21	3.44E+04	1.39E+05	2.48E-01
700	973	1.00E-19	1.00E+03	4.50E+03	2.22E-01
800	1073	1.78E-18	5.62E+01	2.79E+02	2.02E-01
900	1173	1.94E-17	5.16E+00	2.80E+01	1.85E-01
1000	1273	1.45E-16	6.90E-01	4.06E+00	1.70E-01
1100	1373	8.09E-16	1.24E-01	7.84E-01	1.58E-01
1200	1473	3.58E-15	2.80E-02	1.90E-01	1.47E-01
	573	1.31E-14	7.64E-03	5.55E-02	1.38E-01
	673	4.10E-14	2.44E-03	1.88E-02	1.29E-01

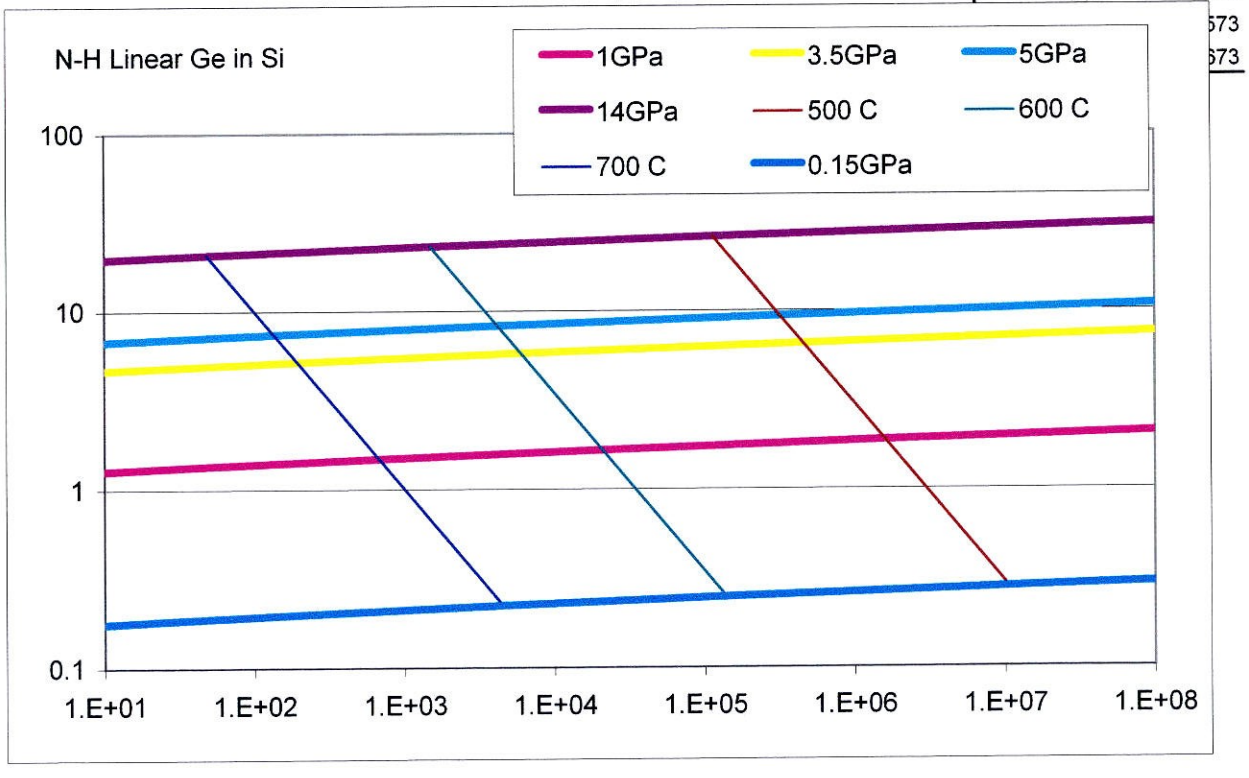

5/20/2004

N_{AVO}	6.02E+23 1/mol	
d	1.00E-08 meters	
V	1.20E-05 m^3/mol	12
σ	Stress (Pa) Variable	
T	Temp (K) Variable	
k	8.6174E-05 eV/K	1.38E-23 J / mol K

Stress 1.50E+08 Pa

Temp (C)	Temp (K)	D_{sd} Si	Diffusion Time	Sintering Time	0.15GPa
100	373	3.51E-66	2.85E+49	4.64E+49	6.14E-01
200	473	1.30E-52	7.69E+35	1.62E+36	4.74E-01
300	573	8.84E-44	1.13E+27	2.92E+27	3.87E-01
400	673	1.43E-37	7.01E+20	2.14E+21	3.27E-01
500	773	5.70E-33	1.76E+16	6.19E+16	2.84E-01
600	873	2.01E-29	4.98E+12	1.99E+13	2.51E-01
700	973	1.32E-26	7.56E+09	3.37E+10	2.24E-01
800	1073	2.60E-24	3.85E+07	1.90E+08	2.03E-01
900	1173	2.07E-22	4.83E+05	2.60E+06	1.86E-01
		8.30E-21	1.20E+04	7.05E+04	1.71E-01
		1.94E-19	5.14E+02	3.25E+03	1.58E-01
		2.97E-18	3.37E+01	2.28E+02	1.48E-01
		3.20E-17	3.12E+00	2.26E+01	1.38E-01
		2.60E-16	3.84E-01	2.96E+00	1.30E-01

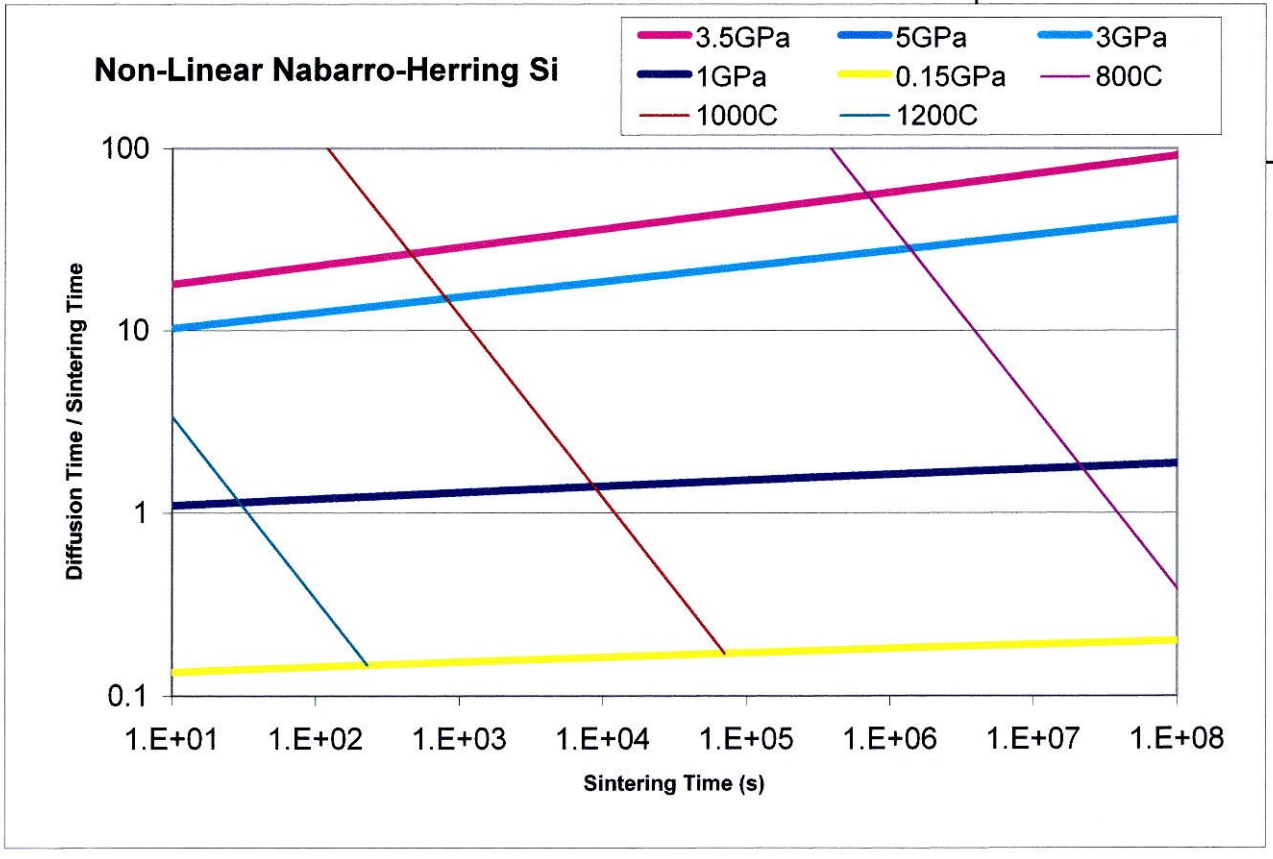

5/23/2004

N_{AVO}	6.02E+23 1/mol	
d	1.00E-08 meters	
V	1.20E-05 m^3/mol	12
σ	Stress (Pa) Variable	
T	Temp (K) Variable	
k	8.6174E-05 eV / K	1.38E-23 J / mol K

D=7.8exp(-2.970/RT) cm^2/sec
= sinh(σV/RT)

Stress			1.50E+08 Pa		
Temp (C)	Temp (K)	D_{Ge} Ge	Diffusion Time	Sintering Time	0.15GPa
100	373	5.80E-44	1.72E+27	2.81E+27	6.14E-01
200	473	1.77E-35	5.66E+18	1.19E+19	4.74E-01
300	573	5.89E-30	1.70E+13	4.39E+13	3.87E-01
400	673	4.48E-26	2.23E+09	6.82E+09	3.27E-01
500	773	3.38E-23	2.96E+06	1.04E+07	2.84E-01
600	873	5.58E-21	1.79E+04	7.15E+04	2.51E-01
700	973	3.23E-19	3.10E+02	1.38E+03	2.24E-01
800	1073	8.76E-18	1.14E+01	5.62E+01	2.03E-01
900	1173	1.35E-16	7.39E-01	3.98E+00	1.86E-01
1000	1273	1.36E-15	7.34E-02	4.30E-01	1.71E-01
1100	1373	9.78E-15	1.02E-02	6.46E-02	1.58E-01
1200	1473	5.38E-14	1.86E-03	1.26E-02	1.48E-01
	73	2.38E-13	4.20E-04	3.04E-03	1.38E-01
	73	8.82E-13	1.13E-04	8.74E-04	1.30E-01

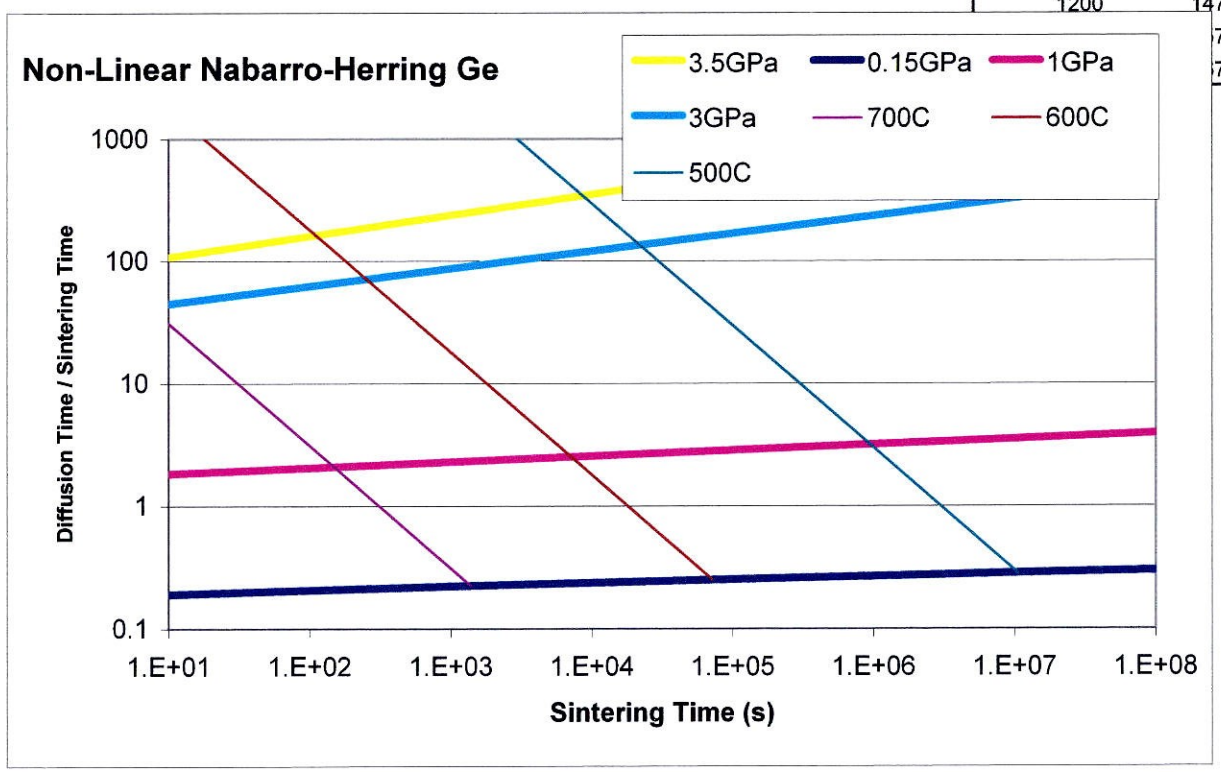

Seconds	Minutes	Hours
10	0.166667	0.00
100	1.666667	0.03
1000	16.66667	0.28
10000	166.6667	2.78
100000	1666.667	27.78
1000000	16666.67	277.78

5/23/2004

Stress		1.00E+09 Pa			
Temp (C)	Temp (K)	D_{sd} Si	Diffusion Time	Sintering Time	1GPa
100	373	3.51E-66	2.85E+49	7.36E+48	3.87E+00
200	473	1.30E-52	7.69E+35	2.52E+35	3.05E+00
300	573	8.84E-44	1.13E+27	4.49E+26	2.52E+00
400	673	1.43E-37	7.01E+20	3.27E+20	2.14E+00
500	773	5.70E-33	1.76E+16	9.40E+15	1.87E+00
600	873	2.01E-29	4.98E+12	3.01E+12	1.65E+00
700	973	1.32E-26	7.56E+09	5.10E+09	1.48E+00
800	1073	2.60E-24	3.85E+07	2.86E+07	1.35E+00
900	1173	2.07E-22	4.83E+05	3.92E+05	1.23E+00
1000	1273	8.30E-21	1.20E+04	1.06E+04	1.13E+00
1100	1373	1.94E-19	5.14E+02	4.89E+02	1.05E+00
1200	1473	2.97E-18	3.37E+01	3.44E+01	9.80E-01
1300	1573	3.20E-17	3.12E+00	3.40E+00	9.18E-01
1400	1673	2.60E-16	3.84E-01	4.45E-01	8.63E-01

Stress		3.50E+09 Pa			
Temp (C)	Temp (K)	D_{sd} Si	Diffusion Time	Sintering Time	3.5GPa
100	373	3.51E-66	2.85E+49	2.10E+48	1.35E+01
200	473	1.30E-52	7.69E+35	7.21E+34	1.07E+01
300	573	8.84E-44	1.13E+27	1.28E+26	8.82E+00
400	673	1.43E-37	7.01E+20	9.34E+19	7.51E+00
500	773	5.70E-33	1.76E+16	2.69E+15	6.53E+00
600	873	2.01E-29	4.98E+12	8.60E+11	5.79E+00
700	973	1.32E-26	7.56E+09	1.46E+09	5.19E+00
800	1073	2.60E-24	3.85E+07	8.19E+06	4.71E+00
900	1173	2.07E-22	4.83E+05	1.12E+05	4.31E+00
1000	1273	8.30E-21	1.20E+04	3.03E+03	3.97E+00
1100	1373	1.94E-19	5.14E+02	1.40E+02	3.68E+00
1200	1473	2.97E-18	3.37E+01	9.82E+00	3.43E+00
1300	1573	3.20E-17	3.12E+00	9.72E-01	3.21E+00
1400	1673	2.60E-16	3.84E-01	1.27E-01	3.02E+00

Temp (C)	Temp (K)		
800	1073		
Stress	D_{sd} Si	Sintering Time	800C
1.50E+08	2.59515E-24	1.91E+08	2.02E-01
1.00E+09	2.59515E-24	2.86E+07	1.35E+00
3.50E+09	2.59515E-24	8.19E+06	4.71E+00
5.00E+09	2.59515E-24	5.73E+06	6.73E+00
1.40E+10	2.59515E-24	2.05E+06	1.88E+01

Temp (C)	Temp (K)		
1000	1273		
Stress	D_{sd} Si	Sintering Time	1000C
1.50E+08	8.3E-21	7.08E+04	1.70E-01
1.00E+09	8.3E-21	1.06E+04	1.13E+00
3.50E+09	8.3E-21	3.03E+03	3.97E+00
5.00E+09	8.3E-21	2.12E+03	5.67E+00
1.40E+10	8.3E-21	7.59E+02	1.59E+01

Temp (C)	Temp (K)		
1200	1473		
Stress	D_{sd} Si	Sintering Time	1200C
1.50E+08	2.97E-18	2.29E+02	1.47E-01
1.00E+09	2.97E-18	3.44E+01	9.80E-01
3.50E+09	2.97E-18	9.82E+00	3.43E+00
5.00E+09	2.97E-18	6.88E+00	4.90E+00
1.40E+10	2.97E-18	2.46E+00	1.37E+01

Stress		1.00E+09 Pa			
Temp (C)	Temp (K)	D_{Ge} Ge	Diffusion Time	Sintering Time	1GPa
100	373	5.80E-44	1.72E+27	4.46E+26	3.87E+00
200	473	1.77E-35	5.66E+18	1.85E+18	3.05E+00
300	573	5.89E-30	1.70E+13	6.74E+12	2.52E+00
400	673	4.48E-26	2.23E+09	1.04E+09	2.14E+00
500	773	3.38E-23	2.96E+06	1.59E+06	1.87E+00
600	873	5.58E-21	1.79E+04	1.08E+04	1.65E+00
700	973	3.23E-19	3.10E+02	2.09E+02	1.48E+00
800	1073	8.76E-18	1.14E+01	8.49E+00	1.35E+00
900	1173	1.35E-16	7.39E-01	6.00E-01	1.23E+00
1000	1273	1.36E-15	7.34E-02	6.48E-02	1.13E+00
1100	1373	9.78E-15	1.02E-02	9.73E-03	1.05E+00
1200	1473	5.38E-14	1.86E-03	1.90E-03	9.80E-01
1300	1573	2.38E-13	4.20E-04	4.58E-04	9.18E-01
1400	1673	8.82E-13	1.13E-04	1.31E-04	8.63E-01

Stress		3.50E+09 Pa			
Temp (C)	Temp (K)	D_{Ge} Ge	Diffusion Time	Sintering Time	3.5GPa
100	373	5.80E-44	1.72E+27	1.27E+26	1.35E+01
200	473	1.77E-35	5.66E+18	5.30E+17	1.07E+01
300	573	5.89E-30	1.70E+13	1.93E+12	8.82E+00
400	673	4.48E-26	2.23E+09	2.97E+08	7.51E+00
500	773	3.38E-23	2.96E+06	4.53E+05	6.53E+00
600	873	5.58E-21	1.79E+04	3.10E+03	5.79E+00
700	973	3.23E-19	3.10E+02	5.97E+01	5.19E+00
800	1073	8.76E-18	1.14E+01	2.43E+00	4.71E+00
900	1173	1.35E-16	7.39E-01	1.71E-01	4.31E+00
1000	1273	1.36E-15	7.34E-02	1.85E-02	3.97E+00
1100	1373	9.78E-15	1.02E-02	2.78E-03	3.68E+00
1200	1473	5.38E-14	1.86E-03	5.42E-04	3.43E+00
1300	1573	2.38E-13	4.20E-04	1.31E-04	3.21E+00
1400	1673	8.82E-13	1.13E-04	3.76E-05	3.02E+00

Temp (C)	Temp (K)		
500	773		
Stress	D_{Ge} Ge	Sintering Time	500C
1.50E+08	8.75795E-18	5.66E+01	2.02E-01
1.00E+09	8.75795E-18	8.49E+00	1.35E+00
3.50E+09	8.75795E-18	2.43E+00	4.71E+00
5.00E+09	8.75795E-18	1.70E+00	6.73E+00
1.40E+10	8.75795E-18	6.06E-01	1.88E+01

Temp (C)	Temp (K)		
600	873		
Stress	D_{Ge} Ge	Sintering Time	600C
1.50E+08	1.36E-15	4.32E-01	1.70E-01
1.00E+09	1.36E-15	6.48E-02	1.13E+00
3.50E+09	1.36E-15	1.85E-02	3.97E+00
5.00E+09	1.36E-15	1.30E-02	5.67E+00
1.40E+10	1.36E-15	4.63E-03	1.59E+01

Temp (C)	Temp (K)		
700	973		
Stress	D_{Ge} Ge	Sintering Time	700C
1.50E+08	5.38E-14	1.27E-02	1.47E-01
1.00E+09	5.38E-14	1.90E-03	9.80E-01
3.50E+09	5.38E-14	5.42E-04	3.43E+00
5.00E+09	5.38E-14	3.80E-04	4.90E+00
1.40E+10	5.38E-14	1.36E-04	1.37E+01

Stress		1.00E+09 Pa			
Temp (C)	Temp (K)	D_{Ge} Si	Diffusion Time	Sintering Time	1GPa
100	373	2.63E-41	3.80E+24	9.81E+23	3.87E+00
200	473	6.59E-34	1.52E+17	4.97E+16	3.05E+00
300	573	4.32E-29	2.32E+12	9.20E+11	2.52E+00
400	673	1.05E-25	9.55E+08	4.45E+08	2.14E+00
500	773	3.38E-23	2.96E+06	1.58E+06	1.87E+00
600	873	2.91E-21	3.44E+04	2.08E+04	1.65E+00
700	973	1.00E-19	1.00E+03	6.74E+02	1.48E+00
800	1073	1.78E-18	5.62E+01	4.18E+01	1.35E+00
900	1173	1.94E-17	5.16E+00	4.20E+00	1.23E+00
1000	1273	1.45E-16	6.90E-01	6.08E-01	1.13E+00
1100	1373	8.09E-16	1.24E-01	1.18E-01	1.05E+00
1200	1473	3.58E-15	2.80E-02	2.85E-02	9.80E-01
1300	1573	1.31E-14	7.64E-03	8.33E-03	9.18E-01
1400	1673	4.10E-14	2.44E-03	2.83E-03	8.63E-01

Stress		3.50E+09 Pa			
Temp (C)	Temp (K)	D_{Ge} Si	Diffusion Time	Sintering Time	3.5GPa
100	373	2.63E-41	3.80E+24	2.80E+23	1.35E+01
200	473	6.59E-34	1.52E+17	1.42E+16	1.07E+01
300	573	4.32E-29	2.32E+12	2.63E+11	8.82E+00
400	673	1.05E-25	9.55E+08	1.27E+08	7.51E+00
500	773	3.38E-23	2.96E+06	4.53E+05	6.53E+00
600	873	2.91E-21	3.44E+04	5.95E+03	5.79E+00
700	973	1.00E-19	1.00E+03	1.93E+02	5.19E+00
800	1073	1.78E-18	5.62E+01	1.19E+01	4.71E+00
900	1173	1.94E-17	5.16E+00	1.20E+00	4.31E+00
1000	1273	1.45E-16	6.90E-01	1.74E-01	3.97E+00
1100	1373	8.09E-16	1.24E-01	3.36E-02	3.68E+00
1200	1473	3.58E-15	2.80E-02	8.15E-03	3.43E+00
1300	1573	1.31E-14	7.64E-03	2.38E-03	3.21E+00
1400	1673	4.10E-14	2.44E-03	8.08E-04	3.02E+00

Temp (C)	Temp (K)		
500	773		
Stress	D_{Ge} Si	Sintering Time	500 C
1.50E+08	1.77865E-18	2.79E+02	2.02E-01
1.00E+09	1.77865E-18	4.18E+01	1.35E+00
3.50E+09	1.77865E-18	1.19E+01	4.71E+00
5.00E+09	1.77865E-18	8.36E+00	6.73E+00
1.40E+10	1.77865E-18	2.99E+00	1.88E+01

Temp (C)	Temp (K)		
600	873		
Stress	D_{Ge} Si	Sintering Time	600 C
1.50E+08	1.45E-16	4.06E+00	1.70E-01
1.00E+09	1.45E-16	6.08E-01	1.13E+00
3.50E+09	1.45E-16	1.74E-01	3.97E+00
5.00E+09	1.45E-16	1.22E-01	5.67E+00
1.40E+10	1.45E-16	4.35E-02	1.59E+01

Temp (C)	Temp (K)		
700	973		
Stress	D_{Ge} Si	Sintering Time	700 C
1.50E+08	3.58E-15	1.90E-01	1.47E-01
1.00E+09	3.58E-15	2.85E-02	9.80E-01
3.50E+09	3.58E-15	8.15E-03	3.43E+00
5.00E+09	3.58E-15	5.71E-03	4.90E+00
1.40E+10	3.58E-15	2.04E-03	1.37E+01

Stress		1.00E+09 Pa			
Temp (C)	Temp (K)	D_{sd} Si	Diffusion Time	Sintering Time	1GPa
100	373	3.51E-66	2.85E+49	1.19E+48	2.39E+01
200	473	1.30E-52	7.69E+35	7.29E+34	1.05E+01
300	573	8.84E-44	1.13E+27	1.83E+26	6.17E+00
400	673	1.43E-37	7.01E+20	1.67E+20	4.21E+00
500	773	5.70E-33	1.76E+16	5.56E+15	3.16E+00
600	873	2.01E-29	4.98E+12	1.98E+12	2.52E+00
700	973	1.32E-26	7.56E+09	3.62E+09	2.09E+00
800	1073	2.60E-24	3.85E+07	2.15E+07	1.79E+00
900	1173	2.07E-22	4.83E+05	3.09E+05	1.57E+00
1000	1273	8.30E-21	1.20E+04	8.65E+03	1.39E+00
1100	1373	1.94E-19	5.14E+02	4.09E+02	1.26E+00
1200	1473	2.97E-18	3.37E+01	2.94E+01	1.14E+00
1300	1573	3.20E-17	3.12E+00	2.97E+00	1.05E+00
1400	1673	2.60E-16	3.84E-01	3.95E-01	9.74E-01

Stress		3.50E+09 Pa			
Temp (C)	Temp (K)	D_{sd} Si	Diffusion Time	Sintering Time	3.5GPa
100	373	3.51E-66	2.85E+49	7.48E+43	3.81E+05
200	473	1.30E-52	7.69E+35	3.54E+31	2.17E+04
300	573	8.84E-44	1.13E+27	3.36E+23	3.37E+03
400	673	1.43E-37	7.01E+20	7.71E+17	9.09E+02
500	773	5.70E-33	1.76E+16	5.10E+13	3.44E+02
600	873	2.01E-29	4.98E+12	3.06E+10	1.63E+02
700	973	1.32E-26	7.56E+09	8.42E+07	8.99E+01
800	1073	2.60E-24	3.85E+07	6.96E+05	5.54E+01
900	1173	2.07E-22	4.83E+05	1.30E+04	3.71E+01
1000	1273	8.30E-21	1.20E+04	4.56E+02	2.64E+01
1100	1373	1.94E-19	5.14E+02	2.60E+01	1.98E+01
1200	1473	2.97E-18	3.37E+01	2.19E+00	1.54E+01
1300	1573	3.20E-17	3.12E+00	2.52E-01	1.24E+01
1400	1673	2.60E-16	3.84E-01	3.76E-02	1.02E+01

Temp (C)	Temp (K)	D_{sd} Si	2.6E-24
800	1073		
Stress	Diffusion Time	Sintering Time	800C
1.50E+08	#DIV/0!	#DIV/0!	#DIV/0!
1.00E+09	#DIV/0!	#DIV/0!	#DIV/0!
3.50E+09	#DIV/0!	#DIV/0!	#DIV/0!
5.00E+09	#DIV/0!	#DIV/0!	#DIV/0!
1.40E+10	#DIV/0!	#DIV/0!	#DIV/0!

Temp (C)	Temp (K)	D_{sd} Si	8.3E-21
1000	1273		
Stress	Diffusion Time	Sintering Time	1000C
1.50E+08	#DIV/0!	#DIV/0!	#DIV/0!
1.00E+09	#DIV/0!	#DIV/0!	#DIV/0!
3.50E+09	#DIV/0!	#DIV/0!	#DIV/0!
5.00E+09	#DIV/0!	#DIV/0!	#DIV/0!
1.40E+10	#DIV/0!	#DIV/0!	#DIV/0!

Temp (C)	Temp (K)	D_{sd} Si	2.97E-18
1200	1473		
Stress	Diffusion Time	Sintering Time	1200C
1.50E+08	#DIV/0!	#DIV/0!	#DIV/0!
1.00E+09	#DIV/0!	#DIV/0!	#DIV/0!
3.50E+09	#DIV/0!	#DIV/0!	#DIV/0!
5.00E+09	#DIV/0!	#DIV/0!	#DIV/0!
1.40E+10	#DIV/0!	#DIV/0!	#DIV/0!

Stress		1.00E+09 Pa			
Temp (C)	Temp (K)	D_{Ge} Ge	Diffusion Time	Sintering Time	1GPa
100	373	5.80E-44	1.72E+27	7.20E+25	2.39E+01
200	473	1.77E-35	5.66E+18	5.37E+17	1.05E+01
300	573	5.89E-30	1.70E+13	2.75E+12	6.17E+00
400	673	4.48E-26	2.23E+09	5.30E+08	4.21E+00
500	773	3.38E-23	2.96E+06	9.38E+05	3.16E+00
600	873	5.58E-21	1.79E+04	7.12E+03	2.52E+00
700	973	3.23E-19	3.10E+02	1.48E+02	2.09E+00
800	1073	8.76E-18	1.14E+01	6.38E+00	1.79E+00
900	1173	1.35E-16	7.39E-01	4.72E-01	1.57E+00
1000	1273	1.36E-15	7.34E-02	5.27E-02	1.39E+00
1100	1373	9.78E-15	1.02E-02	8.14E-03	1.26E+00
1200	1473	5.38E-14	1.86E-03	1.63E-03	1.14E+00
1300	1573	2.38E-13	4.20E-04	4.00E-04	1.05E+00
1400	1673	8.82E-13	1.13E-04	1.16E-04	9.74E-01

Stress		3.50E+09 Pa			
Temp (C)	Temp (K)	D_{Ge} Ge	Diffusion Time	Sintering Time	3.5GPa
100	373	5.80E-44	1.72E+27	4.53E+21	3.81E+05
200	473	1.77E-35	5.66E+18	2.60E+14	2.17E+04
300	573	5.89E-30	1.70E+13	5.04E+09	3.37E+03
400	673	4.48E-26	2.23E+09	2.45E+06	9.09E+02
500	773	3.38E-23	2.96E+06	8.60E+03	3.44E+02
600	873	5.58E-21	1.79E+04	1.10E+02	1.63E+02
700	973	3.23E-19	3.10E+02	3.45E+00	8.99E+01
800	1073	8.76E-18	1.14E+01	2.06E-01	5.54E+01
900	1173	1.35E-16	7.39E-01	1.99E-02	3.71E+01
1000	1273	1.36E-15	7.34E-02	2.78E-03	2.64E+01
1100	1373	9.78E-15	1.02E-02	5.16E-04	1.98E+01
1200	1473	5.38E-14	1.86E-03	1.21E-04	1.54E+01
1300	1573	2.38E-13	4.20E-04	3.39E-05	1.24E+01
1400	1673	8.82E-13	1.13E-04	1.11E-05	1.02E+01

Temp (C)	Temp (K)	D_{Ge} Ge	8.76E-18
700	973		
Stress	Diffusion Time	Sintering Time	700C
1.50E+08	#DIV/0!	#DIV/0!	#DIV/0!
1.00E+09	#DIV/0!	#DIV/0!	#DIV/0!
3.50E+09	#DIV/0!	#DIV/0!	#DIV/0!
5.00E+09	#DIV/0!	#DIV/0!	#DIV/0!
1.40E+10	#DIV/0!	#DIV/0!	#DIV/0!

Temp (C)	Temp (K)	D_{Ge} Ge	1.36E-15
600	873		
Stress	Diffusion Time	Sintering Time	600C
1.50E+08	#DIV/0!	#DIV/0!	#DIV/0!
1.00E+09	#DIV/0!	#DIV/0!	#DIV/0!
3.50E+09	#DIV/0!	#DIV/0!	#DIV/0!
5.00E+09	#DIV/0!	#DIV/0!	#DIV/0!
1.40E+10	#DIV/0!	#DIV/0!	#DIV/0!

Temp (C)	Temp (K)	D_{Ge} Ge	5.38E-14
500	773		
Stress	Diffusion Time	Sintering Time	500C
1.50E+08	#DIV/0!	#DIV/0!	#DIV/0!
1.00E+09	#DIV/0!	#DIV/0!	#DIV/0!
3.50E+09	#DIV/0!	#DIV/0!	#DIV/0!
5.00E+09	#DIV/0!	#DIV/0!	#DIV/0!
1.40E+10	#DIV/0!	#DIV/0!	#DIV/0!

Stress		5.00E+09 Pa			
Temp (C)	Temp (K)	D_{sd} Si	Diffusion Time	Sintering Time	5GPa
100	373	3.51E-66	2.85E+49	1.47E+48	1.93E+01
200	473	1.30E-52	7.69E+35	5.04E+34	1.53E+01
300	573	8.84E-44	1.13E+27	8.98E+25	1.26E+01
400	673	1.43E-37	7.01E+20	6.54E+19	1.07E+01
500	773	5.70E-33	1.76E+16	1.88E+15	9.34E+00
600	873	2.01E-29	4.98E+12	6.02E+11	8.27E+00
700	973	1.32E-26	7.56E+09	1.02E+09	7.42E+00
800	1073	2.60E-24	3.85E+07	5.73E+06	6.73E+00
900	1173	2.07E-22	4.83E+05	7.85E+04	6.15E+00
1000	1273	8.30E-21	1.20E+04	2.12E+03	5.67E+00
1100	1373	1.94E-19	5.14E+02	9.78E+01	5.26E+00
1200	1473	2.97E-18	3.37E+01	6.88E+00	4.90E+00
1300	1573	3.20E-17	3.12E+00	6.80E-01	4.59E+00
1400	1673	2.60E-16	3.84E-01	8.91E-02	4.31E+00

Stress		1.40E+10 Pa			
Temp (C)	Temp (K)	D_{sd} Si	Diffusion Time	Sintering Time	14GPa
100	373	3.51E-66	2.85E+49	5.26E+47	5.42E+01
200	473	1.30E-52	7.69E+35	1.80E+34	4.27E+01
300	573	8.84E-44	1.13E+27	3.21E+25	3.53E+01
400	673	1.43E-37	7.01E+20	2.34E+19	3.00E+01
500	773	5.70E-33	1.76E+16	6.72E+14	2.61E+01
600	873	2.01E-29	4.98E+12	2.15E+11	2.31E+01
700	973	1.32E-26	7.56E+09	3.64E+08	2.08E+01
800	1073	2.60E-24	3.85E+07	2.05E+06	1.88E+01
900	1173	2.07E-22	4.83E+05	2.80E+04	1.72E+01
1000	1273	8.30E-21	1.20E+04	7.59E+02	1.59E+01
1100	1373	1.94E-19	5.14E+02	3.49E+01	1.47E+01
1200	1473	2.97E-18	3.37E+01	2.46E+00	1.37E+01
1300	1573	3.20E-17	3.12E+00	2.43E-01	1.28E+01
1400	1673	2.60E-16	3.84E-01	3.18E-02	1.21E+01

Stress		5.00E+09 Pa				Stress		1.40E+10 Pa			
Temp (C)	Temp (K)	D_{Ge} Ge	Diffusion Time	Sintering Time	5GPa	Temp (C)	Temp (K)	D_{Ge} Ge	Diffusion Time	Sintering Time	14GPa
100	373	5.80E-44	1.72E+27	8.91E+25	1.93E+01	100	373	5.80E-44	1.72E+27	3.18E+25	5.42E+01
200	473	1.77E-35	5.66E+18	3.71E+17	1.53E+01	200	473	1.77E-35	5.66E+18	1.32E+17	4.27E+01
300	573	5.89E-30	1.70E+13	1.35E+12	1.26E+01	300	573	5.89E-30	1.70E+13	4.82E+11	3.53E+01
400	673	4.48E-26	2.23E+09	2.08E+08	1.07E+01	400	673	4.48E-26	2.23E+09	7.43E+07	3.00E+01
500	773	3.38E-23	2.96E+06	3.17E+05	9.34E+00	500	773	3.38E-23	2.96E+06	1.13E+05	2.61E+01
600	873	5.58E-21	1.79E+04	2.17E+03	8.27E+00	600	873	5.58E-21	1.79E+04	7.74E+02	2.31E+01
700	973	3.23E-19	3.10E+02	4.18E+01	7.42E+00	700	973	3.23E-19	3.10E+02	1.49E+01	2.08E+01
800	1073	8.76E-18	1.14E+01	1.70E+00	6.73E+00	800	1073	8.76E-18	1.14E+01	6.06E-01	1.88E+01
900	1173	1.35E-16	7.39E-01	1.20E-01	6.15E+00	900	1173	1.35E-16	7.39E-01	4.29E-02	1.72E+01
1000	1273	1.36E-15	7.34E-02	1.30E-02	5.67E+00	1000	1273	1.36E-15	7.34E-02	4.63E-03	1.59E+01
1100	1373	9.78E-15	1.02E-02	1.95E-03	5.26E+00	1100	1373	9.78E-15	1.02E-02	6.95E-04	1.47E+01
1200	1473	5.38E-14	1.86E-03	3.80E-04	4.90E+00	1200	1473	5.38E-14	1.86E-03	1.36E-04	1.37E+01
1300	1573	2.38E-13	4.20E-04	9.16E-05	4.59E+00	1300	1573	2.38E-13	4.20E-04	3.27E-05	1.28E+01
1400	1673	8.82E-13	1.13E-04	2.63E-05	4.31E+00	1400	1673	8.82E-13	1.13E-04	9.39E-06	1.21E+01

Stress		5.00E+09 Pa				Stress		1.40E+10 Pa			
Temp (C)	Temp (K)	D_{Ge} Si	Diffusion Time	Sintering Time	5GPa	Temp (C)	Temp (K)	D_{Ge} Si	Diffusion Time	Sintering Time	14GPa
100	373	2.63E-41	3.80E+24	1.96E+23	1.93E+01	100	373	2.63E-41	3.80E+24	7.01E+22	5.42E+01
200	473	6.59E-34	1.52E+17	9.94E+15	1.53E+01	200	473	6.59E-34	1.52E+17	3.55E+15	4.27E+01
300	573	4.32E-29	2.32E+12	1.84E+11	1.26E+01	300	573	4.32E-29	2.32E+12	6.57E+10	3.53E+01
400	673	1.05E-25	9.55E+08	8.91E+07	1.07E+01	400	673	1.05E-25	9.55E+08	3.18E+07	3.00E+01
500	773	3.38E-23	2.96E+06	3.17E+05	9.34E+00	500	773	3.38E-23	2.96E+06	1.13E+05	2.61E+01
600	873	2.91E-21	3.44E+04	4.16E+03	8.27E+00	600	873	2.91E-21	3.44E+04	1.49E+03	2.31E+01
700	973	1.00E-19	1.00E+03	1.35E+02	7.42E+00	700	973	1.00E-19	1.00E+03	4.82E+01	2.08E+01
800	1073	1.78E-18	5.62E+01	8.36E+00	6.73E+00	800	1073	1.78E-18	5.62E+01	2.99E+00	1.88E+01
900	1173	1.94E-17	5.16E+00	8.39E-01	6.15E+00	900	1173	1.94E-17	5.16E+00	3.00E-01	1.72E+01
1000	1273	1.45E-16	6.90E-01	1.22E-01	5.67E+00	1000	1273	1.45E-16	6.90E-01	4.35E-02	1.59E+01
1100	1373	8.09E-16	1.24E-01	2.35E-02	5.26E+00	1100	1373	8.09E-16	1.24E-01	8.40E-03	1.47E+01
1200	1473	3.58E-15	2.80E-02	5.71E-03	4.90E+00	1200	1473	3.58E-15	2.80E-02	2.04E-03	1.37E+01
1300	1573	1.31E-14	7.64E-03	1.67E-03	4.59E+00	1300	1573	1.31E-14	7.64E-03	5.95E-04	1.28E+01
1400	1673	4.10E-14	2.44E-03	5.65E-04	4.31E+00	1400	1673	4.10E-14	2.44E-03	2.02E-04	1.21E+01

Stress		3.00E+09 Pa			
Temp (C)	Temp (K)	D_{Ge} Ge	Diffusion Time	Sintering Time	3GPa
100	373	5.80E-44	1.72E+27	1.37E+19	1.26E+08
200	473	1.77E-35	5.66E+18	2.68E+12	2.11E+06
300	573	5.89E-30	1.70E+13	1.15E+08	1.47E+05
400	673	4.48E-26	2.23E+09	9.84E+04	2.27E+04
500	773	3.38E-23	2.96E+06	5.23E+02	5.67E+03
600	873	5.58E-21	1.79E+04	9.21E+00	1.95E+03
700	973	3.23E-19	3.10E+02	3.73E-01	8.32E+02
800	1073	8.76E-18	1.14E+01	2.74E-02	4.17E+02
900	1173	1.35E-16	7.39E-01	3.14E-03	2.35E+02
1000	1273	1.36E-15	7.34E-02	5.07E-04	1.45E+02
1100	1373	9.78E-15	1.02E-02	1.07E-04	9.58E+01
1200	1473	5.38E-14	1.86E-03	2.77E-05	6.71E+01
1300	1573	2.38E-13	4.20E-04	8.55E-06	4.91E+01
1400	1673	8.82E-13	1.13E-04	3.04E-06	3.73E+01

Stress		1.40E+10 Pa			
Temp (C)	Temp (K)	D_{Ge} Ge	Diffusion Time	Sintering Time	14GPa
100	373	5.80E-44	1.72E+27	1.03E+04	1.68E+23
200	473	1.77E-35	5.66E+18	3.17E+00	1.78E+18
300	573	5.89E-30	1.70E+13	1.65E-02	1.03E+15
400	673	4.48E-26	2.23E+09	4.08E-04	5.47E+12
500	773	3.38E-23	2.96E+06	2.63E-05	1.13E+11
600	873	5.58E-21	1.79E+04	3.18E-06	5.63E+09
700	973	3.23E-19	3.10E+02	5.94E-07	5.22E+08
800	1073	8.76E-18	1.14E+01	1.51E-07	7.54E+07
900	1173	1.35E-16	7.39E-01	4.88E-08	1.51E+07
1000	1273	1.36E-15	7.34E-02	1.88E-08	3.91E+06
1100	1373	9.78E-15	1.02E-02	8.30E-09	1.23E+06
1200	1473	5.38E-14	1.86E-03	4.10E-09	4.53E+05
1300	1573	2.38E-13	4.20E-04	2.22E-09	1.90E+05
1400	1673	8.82E-13	1.13E-04	1.29E-09	8.79E+04

A.4 Appendix 4
Press Operations Guide

The Cubic Multi-anvil device in the Asimow Lab has a few websites associated with its operation and maintenance. The Press Operations Guide presented here is intended to be used with the 1000 Ton press home page and checklist maintained by Dr. Asimow as well as the Press Information page maintained by Dr. Mosenfelder. These resources may be found online:

http://www.asimow.com/labstuff/multianvilmanual.htm
http://www.gps.caltech.edu/~jed/Multianvilpage.html

The Press Operations Guide is reproduced here for archival purposes.
(currently online at: http://www.its.caltech.edu/~frgkng/Press/press.html)

Cubic Multianvil Device:

Revision March 9th, 2004

Paul's Manual of Everything Multianvil
Jed's Multianvil Page

Overview:

The goal of this guide is to provide a quick guide for users becoming familiar with the use and operation of the Multianvil Press in the Asimow Lab. A step by step walkthrough from the notion of running an experiment to cleaning up after the inevitable blowout.

Sample Preparation:

The entire cube assembly is composed of a number of elements. Some will be the same for each run, while others will depend on the nature of your sample i.e. the encapsulation required.

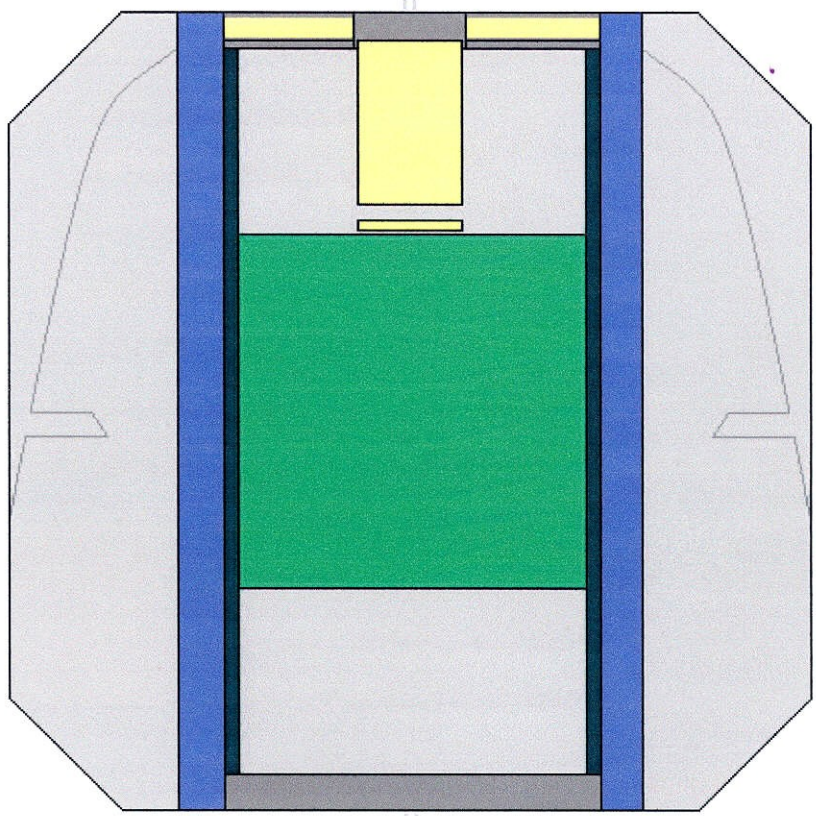

The major components of a cube assembly are the pyrophyllite cube, BaCO3 sleeve, furnace element, MgO filler, Moly ring/plate, thermocouple, and sample. If preparation has been done before hand all these components can be put together fairly quickly and you can have your experiment up and running in a few hours or less.

The pyrophyllite cubes are prepared as below, as is the BaCO3 sleeve. The BaCO3 sleeve should slide neatly into the pyrophyllite cube. Into this the furnace should be slotted. Typical furnace materials are LaCrO3 and graphite. Once the furnace is in hand make sure you measure it to determine how big the other components in the assembly will be. At this time it is also a good idea to have your sample prepared so you know how much space it will take up in your assembly. The furnace will be shorter than the BaCO3 sleeve, but will sit directly on the Moly plate at the bottom of the assembly. Once you have worked out the dimensions of the internal components you can cut the MgO pieces from stock supplies and start putting everything together. The dimensions of a typical experiment with graphite heater with graphite

capsule:

- 18.53mm Graphite Furnace
- 4.95mm MgO plug
- 4.73mm MgO sleeve
- 4.27mm 4-hole alumina
- 3.75mm 1-hole alumina
- 3.61mm 1-hole alumina
- 0.81mm Graphite plate
- 0.43mm Graphite Plate
- 7.61mm Sample Volume
- 1.45mm Moly ring
- 1.45mm Moly plate

With all the components measured, cut, and laid out you can begin assembly. Insert the BaCO3 sleeve into Pyrophyllite cube. Put the moly plate at the bottom and slide the furnace in on top of it. Add the MgO plug then the sample. Put the MgO sleeve on top of that and the moly ring. Insert the thermocouple and fill the gaps with resbond. Bake it overnight and you are ready to do some experimentation.

Moly Rings

There are two moly components in the assembly. They are used to transfer current from the press to the furnace and they protect the furnace from extrusion. The bottom Moly plate requires no modification. The top ring requires a slot to be cut in it so the thermocouple can pass through. It is important to make this slot very deep, the single hole alumina must sit completely in the volume of the ring or else it will break on loading and your thermocouple will be severed. The placement is slightly offcenter, as in the diagram. This is because the thermocouple wires will come out of the four-hole alumina off center. Stretching or straining the wires across the top of the four-hole alumina can lead to a short with the moly ring or to one of the wires being severed on loading.

The moly ring can be cut with the dremel tool and diamond tipped grinders. Starting with the small wheel for the big initial cuts then moving to the smaller diamond drill for cleaning up the slot is recommended.

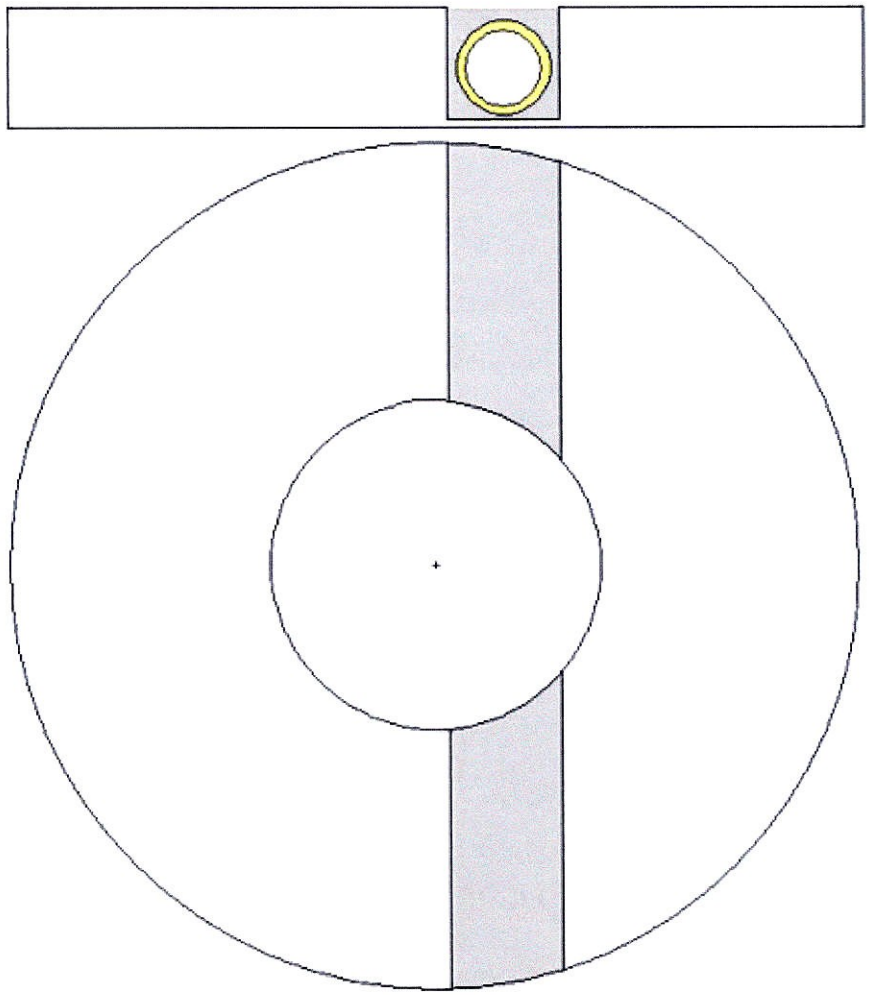

Thermocouple

It is important to be dileberate and careful in the construction of the thermocouple. This component has the most pieces, the highest failure rate, and without it your experiment is toast.

Components in a thermocouple for the cubic device:

- Single hole Alumina: Insulation for the thermocouple wire as it passes across the top of the furnace via the moly ring.
- Four-hole Alumina: Support/insulation, wires cross at base to form thermocouple contact.
- 0.25mm Alumina plate
- Blue Thermocouple wire: Use a piece of insulation to mark the 'color' of the wire.
- Copper coil
- Blue Thermocoulpe extension wire
- Red Thermocouple wire: Use a piece of insulation to mark the 'color' of the wire.

- Red Thermocouple extension wire

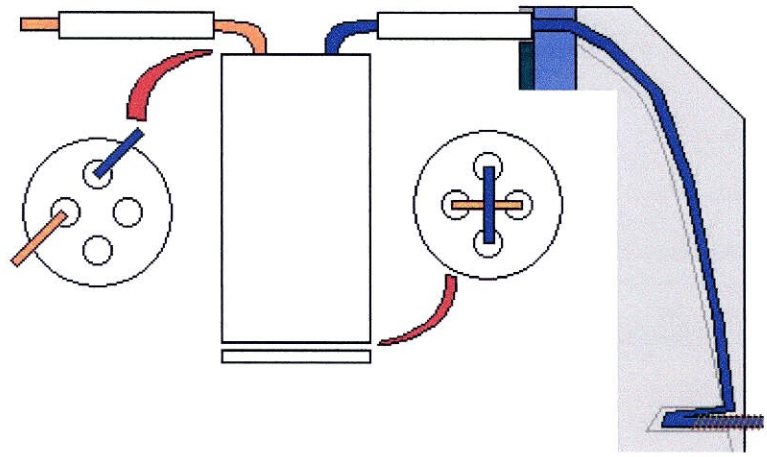

The four-hole alumina should be slightly shorter than the MgO plug surrounding it, or else the thermocouple will push itself out one end or the other. In the cube assembly the thermocouple components are the hardest components. They will pierce the sample capsule or can end up touching the anvil face as the rest of the assembly extrudes around them. The ends of the four-hole alumina should also be ground with the dremel diamond drill tool such that they are concave. This creates a small space for the crossed thermocouple wires to form their contact point. Poor contact will cause thermocouple problems. The thin alumina plate at the base of the thermocouple stack serves to protect the thermocouple from puncturing the sample capsule.

Assembly goes as follows. Into the four-hole alumina insert the red and blue thermocouple wires. Carefully bend the ends of each into a hook such that the hooked portion can fit into one of the unused holes in the four-hole alumina. The thermocouple wire is brittle, so avoid over bending. Use the small pliers to start and some tweezers to get the final shape. Make sure the two wires cross at the bottom, this means starting by passing the two wires through adjacent holes in the alumina and using opposite holes for the hooks as shown in the diagram. Once the thermocouple is formed you are ready to insert the unit into the cube assembly. Make sure the alumina disk is at the bottom of the single hole MgO plug. You may have to file out the interrior of the moly ring to allow the four-hole alumina to slide through easily. Once done, simply insert the 4-hole alumina and make sure the thermocouple wires line up with the slot in the moly ring and they both line up with the slot cut in the pyrophyllite cube. fold down the one-hole alumina and thermocouple wires then file down a small pyrophyllite plug and mix some resbond to seal the top end of the 4-hole alumina-thermocouple unit. Once that sets up a bit you can start pressing the thermocouple wires into the slots in the pyrophyllite. We do this to make sure our thermocouple wires do not get

stretched across the moly ring, as tends to happen when you press the wires into the pyrophyllite before you've resbonded the center of the unit. Once the center is secure you may begin pressing the thermocouple leads into the pyrophyllite, typically done with the edge of a razor blade. Once in position you may find the copper coil to assist in holding everything in place, since the copper coil fits neatly into the hole drilled into the side of the cube halfway down. Into the other end of the coil insert the extension wire, making sure there is overlap between the thermocouple wire and the extension wire. Then crimp the copper coil to make good contact between the wires and prevent pull out. Now begin to press resbond into the slot to fill the space and make sure the thermocouple leads remain isolated during the experiment. The entire assembly should be baked overnight in the bake out oven to make sure the resbond sets prior to beginning the experiment.

Tricks I've seen

Graphite will decompose in atmosphere with increasing temperature. For high temperature or long time experiments one will probably have to rely on LaCrO3 heaters. But I suspect is possible to run an experiment in a reducing atmosphere by including a sacrificial graphite component in the run. Since the graphite oxidizes and turns into a gas this might not be a useful bit of information for our press and the extreme pressures it reaches, as sudden or unpredictable volume change tends to lead to blowouts and failed experiments.

Oxygen rich environments, however, are sustained under pressure by the inclusion of PO5. Under pressure PO5 decomposes into PO4 + O, this creates an increased oxygen partial pressure in the region of compression. If you included PO5 near your sample from the start you could synthesize under oxygen rich conditions. This is probably of limited use for typical petrological applications, but certainly sees more use in Materials Science and is a very slick means of controlled atmosphere synthesis with low tech equipment.

Press Preparation:

Refer to Paul's Checklist. It is really quite good.

Things to add:

- Reset the pressure limit on the black box in the grey pressure control panel. Labview should be paused to allow pressure limit setting.
- Confirm the cooling water is connected and running.
- Using the air compressor to add the initial load (switch setting "B" to increase the load and "A" to release the load), closing the release valve, and switching to labview control.
- Temperature control and heat switch set to off.

Loading and Operation:

Again to Paul's Checklist.

Things to add:

- The target load should not exceed 500 tons, as higher loads will threaten the anvil drivers (anvil drivers break regularly at 800 tons).
- Heat switch should be turned to off after completion of the program.
- The pressure and temperature control are not linked, so once the pressure is stable you will have to start the temperature profile. Once the temperature profile is complete you will have to change the pressure control in labview to decompress the run.
- Always leave a small negative value in the minimum setting for press control. Without a value of even -0.1 V (enough to generate a press rpm of -25 to -40) the pressure in your run can build up and throw off the experiment. This is especially true as you start the cooling water and the heating.
- Cooling water should be turned off after the heat is turned off. Otherwise water will condense all over the plates which will corrode them and possibly make the press electrically unsafe.
- Use the plexiglas shield to prevent pasersby from unintentionally encountering the electrified top or bottom plates of the press.
- >>link to pressure calibrations<<

  Cubic device 21mm cube

  - 3.5 GPa on 412 tons
  - 4GPa on 500 tons
  - 5GPa on 800 tons

Unloading:

- Backing off the pressure at 5 tons per minute is a safe rate for the cubic device and generally fast enough for most users.
- remove and clean all anvils and anvil drivers.
- Inspect pins and anvil drivers for damage, especially in the area of the guide pin groove.
- Replace any lost G10 on the anvils or drivers.
- Vacuum the interior of the module.
- Clean the top and bottom 7mil teflon sheets.
- Ensure that no blowout debris remains wedged in the teflon, as further use will cause electrical shorts or damage to the anvils or drivers.
- Remove the used mylar sheets and thread the *Staneff Devices[1]* when you remove your sample to make assembly of the next run easy.

[1] The Staneff Device is a toothpick with a wire wound around it that is used to thread the thermocouple wires into and out of the module. The end of the wire opposite the toothpick forms a loop, through which the thermocouple is threaded. When the module is loaded these protrude into the area where the pressure assembly resides, allowing the thermocouple wires to thread through to the terminal leads in a quick and hassle-free manner. Staneff Devices have a limited lifespan, as the work hardening sustained in the wire during service eventually leads to brittle failure.

Pressure Assembly Component Preparation:

Pyrophyllite Cubes

The pyrophyllite cubes come with furnace holes but need to have slots cut for the thermocouple leads prior to being cured. These cuts are made freehand with a dry diamond blade, as the pyrophyllite can pick up water if you cut wet. It is very important to have a firm grip on the pyrophyllite cube when cutting free hand, losing control or drifting can pinch the blade or break it. If the cubes are cut wet they will need to sit in a bake out furnace for a few hours to drive out some of the water. Actual cutting follows the diagram: Start cutting into one diagonal from the halfway point. Cut the slot and roll the blade around the corner to the top 1/8" of the drilled furnace hole. The thermocouple leads will be packed into this slot when the assembly is prepared, so it is important to make sure there is ample room and no sharp corner. Once the cutting is finished you will need to drill on the halfway point to allow space for the thermocouple to extension wire joint. This feature cleans up the exit from the pyrophyllite cube and helps to standardize the cube to press interface.

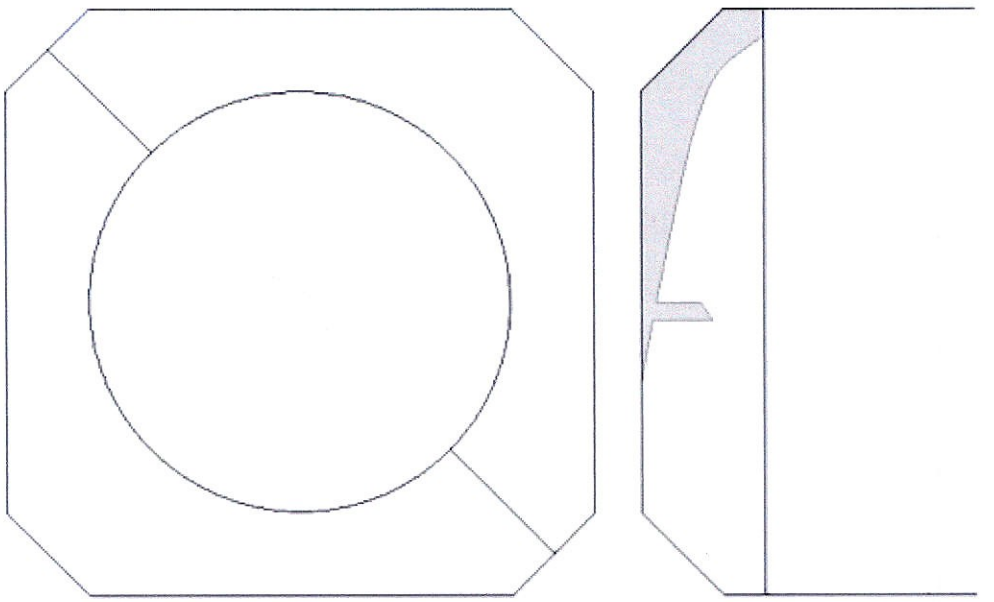

The cut cubes are placed in a furnace for 1 hour at 500C then the temperature is increased to 900C for 4 hours. After this curing step the furnace hole is drilled to 1/2" with a carbide drill. The pyrophyllite undergoes a 3% expansion during the cure, hence the need to rebore the furnace hole.

BaCO3 Sleeves

First assemble the supplies:

- Rubber Gloves ($BaCO_3$ is a poison)
- Nickel plated Die + plunger apparatus

- Aluminum rings for use with the Enerpac press
- Eggcrate foam (should be on Enerpac)
- Metal holder for Die
- BaCO3 powder
- Carbon Black
- Aluminum weighing pans
- Mortar + Pestle
- Alumina firing plate
- Molycote
- Scoops, swabs, paper towels, ethanol

It is a good idea to perform these tasks in bunches, first weigh out all the BaCO3 for all the sleeves you intend to make, then move on to the next step. This helps keep the work area free of clutter. Initially weigh out 5.25 grams of BaCO3 into several weighing pans. To this add just a *smidge* of Carbon Black. Mix the BaCO3 and Carbon together in the mortar and pestle until the texture and color are even. While working on the others and pressing the sleeves, store these in the box furnace near the Enerpac press at 150C. Swab the die and die mandrils, etc. with molycote. Remove one weighing pan and load the die (warning will be hot). Fit the die into the metal die holder, horizontally, and once seated fully stand it upright and load it on the press. Press to 2,000psi on the guage and hold for 60 seconds. Back off plunger, load Aluminum rings onto Enerpac and extract the BaCO3 sleeve carefully. Make sure the foam is set between the rings and positioned to catch the BaCO3 sleeve and mandrils as they come out of the die. The BaCO3 sleeve will be very fragile, so take care. Set the BaCO3 sleeve on the alumina firing plate and continue until all sleeves have been pressed. Turn the box furnace up to 600C and fire the BaCO3 sleeves for 30 minutes. When finished allow the BaCO3 sleeves to cool and turn the furnace back down to 150C. Store the BaCO3 sleeves in a vacuum chamber / dessicator until needed. Clean all apparatus with ethanol and paper towels.

Bibliography

Chapter 1

1 Seebeck, T.J. (1821). "Ueber den magnetismus der galvenische kette." *Abhandlungen der Deutschen Akademie der Wissenshafften zu Berlin* 289.

2 Seebeck, T.J. (1823). "Magnetic polatization of metals and minerals." *Abhandlungen der Deutschen Akademie der Wissenshafften zu Berlin* 265.

3 Seebeck, T.J. (1823). "Magnetische polarisation der metalle und erze durck temperatur-differenz." *Abhandlungen der Akademie der Wissenshafften zu Berlin* 265.

4 Seebeck, T.J. (1826). *Ann. Phys.,* (Leipzig) 2(6): 1.

5 Seebeck, T.J. (1826) "Methode, Platinatiegel auf ihr chemische reinheit durck thermomagnetismus zu prufen." *Schweigger's J. Phys.* (46): 101.

6 Henri Le Châtelier, (1885).

7 The International Practical Temperature Scale of 1968, Amended Edition of 1975 (1976). *Metrologia* 12: 7-17.

8 Peltier, J.C. (1834). "Nouvelles experiences sur la caloriecete des courans electriques." *Ann. Chem.,* 56: 371-387.

9 Ioffe, A.F. (1957). "Semiconductor Thermoelements and Thermoelectric Cooling." *Infosearch*, London.

10 Altenkirch, E. (1909). *Physikalische Zeitschrift*, 10: 560-580.

11 Altenkirch, E. (1911). *Physikalische Zeitschrift*, 12: 920-924.

12 Ioffe, A.F. (1949).

13 Ioffe, A.F. (1956). "2 New Applications of the Peltier Effect." *Soviet Physics. Technical Physics* 1(2): 462-465.

14 Varmaraf ehf. IceTec Keldnaholti, Iceland, http://www.varmaraf.is/index.htm.

15 FerroTec, Nashua, NH, USA http://www.ferrotec.com/usa/index.html.

16 Cassini-Huygens (1997-Present). Mission to Saturn & Titan, NASA, http://saturn.jpl.nasa.gov/home/index.cfm.

17 Kingery, W.D., H.K. Bowen, et al. (1976). Introduction to Ceramics. Cambridge, Mass., John Wiley & Sons.

18 Venkatasubramanian, R., E. Siivola, et. al. (2001). "Thin-film thermoelectric devices with room-temperature figures of merit." *Nature* 413 (6856): 597-602.

19 Caillat, T., A. Borshchevsky, et al. (1999) "High-Performance Thermoelectric Materials Based on b-Zn3Sb3." *NASA Tech Briefs* (NPO19851).

20 Slack, G.A. (1995). CRC Handbook of Thermoelectrics, edited by D. M. Rowe (Chemical Rubber, Boca Raton FL, 1995). 34: 407.

21 Sales, B.C., D. Mandrus, et al. (1997). "Filled skutterudite antimonides: Electron crystals and phonon glasses." *Phys Rev B* 56(23) 15081-15089.

22 Nolas, G.S., D. T. Morelli, et al. (1999). "Skutterudites: A phonon-Glass-Electron Crystal Approach to Advanced Thermoelectric Energy Conversion Applications." *Annual Review of Materials Science* [0084-6600]. 29: 89-116.

23 Fleurial, J.P., T. Caillat, et al. (1994). Proc 13th Int. Conf. on 'Thermoelectrics.' Kansas City, *AIP Press*. 316: 209-211.

24 Mineralogy Database, http://webmineral.com/data/Skutterudite.shtml

25 Lincoln Labs Review on Skutterudite Thermoelectrics. (1995).

26 Jeitschko, W. and D. Braun (1977). "LaFe4P12 with filled CoAs3-type structure and isotrypic lanthanoid transition metal phosphides." *Acta Crystallographica.* B33: 3401-3406.

27 Meisner, G.P., M.S. Torikachvili, et al. (1985). "UFe4P12 and CeFe4P12 – Nonmetallic Isotopes of Superconducting LaFe4P12." *Journal of Applied Physics* 57(8): 3073-3075.

28 Jung, D.W., M.H. Whangbo, et al. (1990). "Importance of the X4-Ring Orbitals for the Semiconducting, Metallic, or Superconducting Properties of Skutterudites Mx3 and Rm4x12." *Inorganic Chem.* 29(12): 2252-2255.

29 Grandjean, F., A. Gerard, et al. (1984). "Some Physical-Properties of LaFe4P12 Type Compounds." *The Journal of Physics and Chemistry of Solids.* 45(8-9): 877-886.

30 Stetson, N.T., S.M. Kauzlarich, et al. (1991). "The Synthesis of Structure of 2 Filled Skutterudite Compounds – BaFe4Sb12 and BaRu4Sb12." *Journal of Solid State Chemistry.* 91(1): 140-147.

31 Braun, D.J. and W. Jeitschko (1980). "Thorium-Containing Pnictides with the LaFe4P12 Structure." *Journal of the Less-Common Metals.* 76(1-2): 33-40.

32 Danebrock, M.E., C.B.H. Evers, et al. (1996). "Magnetic Properties of alkaline earth and lanthanoid iron antimonides AFe4Sb12 (A=Ca,Sr,Ba,La-Nd,Sm,Eu) with the LaFe4P12 structure." *The Journal of Physics and Chemistry of Solids.* 57(4): 381-387.

33 Chen, B.X., J.H. Xu, et al. (1997). "Low-temperature transport properties of the filled skutterudite CeFe4-xCoxSb12." *Phys. Rev. B* 55(3): 1476-1480.

34 Fleurial, J.P., T. Caillat, et al. (1997). Proc. 16th Int. Conf. on 'Thermoelectrics,' *16th International Conference on Thermoelectrics, IEEE* (Cat. No. 97TH8291).

35 Caillat, T., J.P. Fleurial, et al. (1999) "A New High Efficiency Segmented Thermoelectric Unicouple." *34th Intersociety Energy Conversion Engineering Conference* IECE (IECE99CD):2567.

36 Snyder, G.J. (2004). "Application of the Compatibility Factor to the Design of Segmented and Cascaded Thermoelectric Generators" *Applied Physics Letters* 84(13): 2436-2438.

37 Chen, G., M. S .Dresselhaus, et al. (2003). "Recent developments in thermoelectric materials." *International Materials Reviews*. 48(1): 45-66.

38 Rundquist, S. and N.-O. Ersson (1968). Arkiv for Kemi. 30: 103-114.

39 Kaye, G.W.C., and T.H. Laby (1966). "Table of Physical and Chemical Constants." Longmans Green, London.

40 Sze, S.M. (1981). Physics of semiconductor devices. New York, John Wiley & Sons, Inc. 2nd ed.

41 Snider, T.S., J.V. Badding, et al. (2000). "High-pressure stability, pressure-volume equation of state, and crystal structure under pressure of the thermoelectric material IrSb3." *Chemistry of Materials*. 12(3): 697-700.

42 Anno, H., K. Matsubara, et al. (1999). "Effects of doping on the transport properties of CoSb3." *Journal of Applied Physics* 86(7): 3780-3786.

43 Morelli, D.T., G.P. Meisner, et al. (1997). "Cerium filling and doping of cobalt triantimonide." *Physical Review B, Condensed Matter* 56(12):7376-7383.

44 Sales, B.C., D. Mandrus, et al. (1996), "Filled skutterudite antimonides: A new class of thermoelectric materials." *Science* 272(5266): 1325-1328.

45 Chapon, L., D. Ravot, et al. (1999). "Nickel-substituted skutterudites: synthesis, structural and electrical properties." *Journal of Alloys and Compounds*. 282(1-2): 58-63.

46 Staneff, G. (2001). High pressure synthesis of cerium filled cobalt triantimonide. International Conference on Thermoelectrics.

47 Walker, D., M.A. Carpenter, et al. (1990). "Some simplifications to multianvil devices for high pressure experiments." *The American Mineralogist*. 75(9-10): 1020-1028.

48 Walker, D. (1991). "Lubrication, gasketing, and precision in multianvil experiments." *The American Mineralogist*. 76(7-8): 1092-1100.

49 Mosenfelder, J.L. and S.R> Bohlen (1997). "Kinetics of the coesite to quartz transformation." *Earth and Planetary Science Letters*. 153(1-2): 133-147.

50 Susaki, J., M. Akaogi, et al. (1985). "Garnet-perovskite transformation in CaGeO3 in-situ x-ray measurements using synchrotron radiation." Geophysical Research Letters. 12(10) 729-732.

51 Takizawa, H., K. Miura, et al. (1999). "Atom insertion into the CoSb3 skutterudite host lattice under high pressure." *Journal of Alloys and Compounds*. 282(1-2): 79-83.

52 Staneff, G., P.D. Asimow, et al. (2003). "Synthesis and thermoelectric properties of Ce(Ru0.67Rh0.33)4Sb12." MRS Fall Meeting. Boston, Mass. MRS Symposium Proceedings.

53 Hunter, B. (1998). "Rietica – A visual Rietveld program." *International Union of Crystallography Commission on Powder Diffraction Newsletter* 20(Summer): http://www.rietica.org.

54 Phillips Analytical. "X'Pert Plus." http://www.panalytical.com/.

55 Young, R.A. (2000). The Rietveld Method. New York, Oxford University Press.

56 Armstrong, J. (1981). "CITZAF." National Institute of Standards and Technology. http://www2.arnes.si/~sgszmera1/others/others/mlist.html

57 Van der Pauw, L.J. (1958). "A method of measuring specific resistivity and hall effect of discs of arbitrary shape." *Phillips Research Reports*. 13(1): 1.

58 Van der Pauw, L.J. (1958). "A method of measuring the resistivity of and hall coefficient on lamellae of arbitrary shape." Phillips *Technical Review*. 20:220.

59 Uher, C. (2001). "Skutterudites: Prospective Novel Thermoelectrics." *Recent Trends in Thermoelectric Materials Research I: Semiconductors and Semimetals*. 69: 139-253.

60 Vandersande, J.W., A. Zoltan, et al. (1989). "Accurate determination of specific-heat and high-temperatures using the flash diffusivity method." *International Journal of Thermalphysics*. 10(1): 251-257.

61 Lesher, C.E., J. Pickering-Witter, et al. (1999). "Operation and calibration of the 'Getting' cubic multi-anvil apparatus." *EOS Transactions of the American Geophysical Union*. 80(46): F1116.

62 Getting, I.C. (1998). "New determination of the bismuth I-II equilibrium pressure: a proposed modification to the practical pressure scale." *Metrologia*. 35(2): 119-132

63 Zhang J., B. Li, et al. (1996). "In situ x-ray observations of the coesite stishovite transition: Reversed phase boundary and kinetics." *Physics and Chemistry of Minerals.* 23(1): 1-10.

64 Morishima, H., T. Kato, et al. (1994). "The phase-boundary between Alpha-Mg2SiO4 and Beta-Mg2SiO4 determined by in-situ x-ray observation." *Science.* 265(5176): 1202-1203.

65 Dilley, N.R., E.D. Bauer, et al. (2000). "Thermoelectric properties of chemically aubstituted skutterudites YbyCo4SnxSb12-x." *Journal of Applied Physics.* 88(4): 1948-1951.

66 Nagamoto, Y., K. Tanaka, et al. (1997). "Thermoelectric properties of the skutterudite related phase CoSn1.5Te1.5." *International Conference on Thermoelectrics.* ICT Press.

67 Zhuravlov, N.N. and G.S. Zhdonov (1956). Soviet *Physical Crystallography.* 1: 404.

68 Uher, C., J. Yang, et al. (1999). *Material Research Society Symposium Proceedings.* 545: 247.

69 Sales, B.C. (1998). *MRS Bulletin.* 23: 15.

70 Nolas, G.S., H.B. Lyon, et al. (1997). "Expanding the investigation of the thermoelectric properties of rare-earth-filled skutterudites." 16th International Conference on Thermoelectrics. *IEEE*(0-7803-4057-7/97).

71 Takizawa, H., K. Okazaki, et al. (2001). High pressure synthesis of new filled skutterudites.

72 Morelli, D.T., T. Caillat, et al. (1995). "Low-temperature transport properties of p-type CoSb3." *Physical Review B, Condensed Matter*. 51(5): 9622-9628.

73 Caillat, T. (1996). "Preparation and thermoelectric properties of IrxCo1-xSb2 alloys." *The Journal of Physics and Chemistry of Solids*. 57:9 1351-1358.

74 Nolas, G.S., H. Takizawa, et al. (2000). "Thermoelectric properties of Sn-filled skutterudites." *Applied Physics Letters*. 77(1): 52-54.

75 Nolas, G.S., G.A. Slack, et al. (1996). "The effect of rare-earth filling on the lattice thermal conductivity of skutterudites." *Journal of Applied Physics*.79(8): 4002-4008.

76 Fornari, M. and D.J. Singh (1999). "Prediction of room-temperature high-thermoelectric performance in n-type La(Ru1-xRhx)4Sb12." *Applied Physics Letters.* 74(24): 3666-3668.

77 Brinker, C.J. (2004). "Evaporation-Induced Sel-Assembly: Functional Nanostructures Made Easy." *MRS Bulletin* 29(9).

78 Ursell, T.S. and G.J. Snyder (2002). "Compatibility of Segmented Thermoelectric Generators." *ICT Conference Proceedings.*

79 Kim, K.H., M. Uehara, et al. (2000) "Thermal and Electrical Transport Properties and Two-Phase Mixtures in La5/8-xPrxCa3/8MnO3" *Physical Review Letters* 84(13):2961-2964.

80 Murray, P., D.T. Livey, et al. (1958) Hot Pressing of Ceramics, Ceramic Fabrication Processes. W. D. Kingery Ed., Boston, Technology Press of Massachusetts Institute of Technology and John Wiley & Sons: 147-171.

81 Wilkinson, D.S., and M.F. Ashby (1976). Sintering and Catalysis. New York. Plenum.

82 Andrault, D., R.J. Angel, et al, (2003), "Equation of state of stishovite to lower mantle pressures." *American Mineralogist*, 88(2-3): 301-307.

83 Reed, J.S. (1995) Solid State Sintering, Principles of Ceramics Processing 2nd ed. John Wiley & Sons New York 1995: 594-618.

84 Wachtman, J.B., (1996) Creep in ceramics. Mechanical Properties of Ceramics John Wiley & Sons, New York: 311-316.

85 Nabarro, F.R. (1947). Deformation of Crystals by Motion of Single Ions. *Report of a Conference on the Strength of Solids.* Bristol, University of Bristol: 75-90.

86 Herring, C. (1950). Diffusional Viscosity of Polycrystalline Solids. *J. Appl. Phys.*, 21(5): 437-445.

87 Coble, R.L. (1961). Sintering of Crystalline Solids. Intermediate and Final State Diffusion Models. *J. Appl. Phys.*, 32(5)787-792.

88 Wilkinson, D.S., (1975). Pressure Sintering by Power Law Creep. *Acta Metallurgica.* 23(11):1277-1285.

89 Ashby, M.F., R.A. Verral (1973). "Diffusion-Accomodated flow and superplasticity." *Acta Metallurgica* 21(2): 149-163.

90 Urick, P., and M.R. Notis (1973). "Final Stage Densification During Pressure Sintering of CoO." *J. Am. Ceram Soc.* 56(11): 570-574.

91 Notis, M.R. (1977). "Advances in Ceramic Hot Forming and Pressing: Theory and Practice." *Ceramurgia Int.* 3.

92 Ashby, M.F. (1972). "A First Report on Deformation Mechanism Maps." *Acta Metalurgical.* 20(7): 887-896.

93 Poirier, J.P. (1991). "Introduction to the Physics of the Earth's Interior." Cambridge, Cambridge University Press.

94 Bracht, H., E.E. Haller, et al. (1998). "Silicon self-diffusion in isotopic heterostructures." *Physical Review Letters.* 81(2): 393.

95 Mitchell, M.J., P. Ashburn, et al. (2002). "Germanium diffusion in polycrystalline emitters of SiGe hererojunction bipolar transistors fabricated by germanium implantation." *Journal of Applied Physics.* 92(11): 6924-6926.

96 Gozza, G.E., (1991). Pressure Densification. Ceramics and Glasses, ASM Int. 4: 296-303.

97 Bohlen, S.R. (1984). "Equilibria for precise pressure calibration and a frictionless furnace assembly for the piston-cylinder apparatus." *Neues Jahrb. Minearl., Monatsh* (9): 404-412.

98 Dunn, T. (1993). The Piston-Cylinder Apparatus. 3: 38-89.

99 Luth, R.W. (1993). Measurement and control of intensive parameters in experiments at high pressure in solid-media apparatus. 2: 14-37.

100 Boyd, F.R., and J. L. England. (1960). "Apparatus for phase-equillibrium measurements at pressures up to 50 kilobars and temperatures up to 1750C." *J. Geophys. Red.* 65(2): 741-748.

101 Tingle, T.N. (1988). "Retrieval of uncracked single crystals from high pressure in piston-cylinder apparatus." *Am. Minaral.* 73(9-10): 1195-1197.

102 Farver, J.R., and R.A. Yund (1995). "Grain boundary diffusion of oxygen, potassium and calcium in natural and hot-pressed feldspar aggregates." *Contrib. Mineral. Petrol.* 118(4): 340-355.

103 El-Genk, M.S., H.H. Saber, et al. (2002). "A Performance comparison of SiGe and skutterudite based segmented thermoelectric devices." *AIP conference proceedings* 608(1): 1007-1015.

104 Akimoto, S., H Fujisawa, et al. (1965). "Olivine-Spinel transition in Fe3SiO4 and Ni2SiO4." *Journal of Geophysical Research.* 70(8): 1969.